To İpek and Sedef

BIOMINERALIZATION WITH ENGINEERED CELLULAR SYSTEMS

A DISSERTATION SUBMITTED TO

THE GRADUATE SCHOOL OF ENGINEERING AND SCIENCE

OF BILKENT UNIVERSITY

IN PARTIAL FULFILLMENT OF THE REQUIREMENTS FOR

THE DEGREE OF

DOCTOR OF PHILOSOPHY

IN

MATERIALS SCIENCE AND NANOTECHNOLOGY

By

ELİF ERGÜL

AUGUST 2019

BIOMINERILIZATION WITH ENGINEERED CELLULAR SYSTEMS

By Elif Ergül

August 2019

We certify that we have read this dissertation and that in our opinion it in fully adequate, in scope and in quality, as a thesis for the degree of Doctor of Philosophy.

Urartu Özgür Şafak Şeker (Advisor)

Murat Alper Cevher

Pınar Huri

Kezban Ulubayram

Bilge Baytekin

Approved for the Graduate School of Engineering and Science:

Ezhan Karaşan

Director of the Graduate School

“Reproduced in part with permission from [Biomineralization of Calcium Phosphate Crystals Controlled by Protein–Protein Interactions. Elif Duman, Ebru Şahin Kehribar, Recep Erdem Ahan, Esra Yuca, and Urartu Özgür Şafak Şeker. ACS Biomaterials Science & Engineering Article ASAP DOI: 10.1021/acsbiomaterials.9b00649] Copyright [2019] American Chemical Society."

ABSTRACT

BIOMINERALIZATION WITH ENGINEERED CELLULAR SYSTEMS

Elif ERGÜL

PhD in Materials Science and Nanotechnology

Advisor: Urartu Özgür Şafak Şeker

August, 2019

Hydroxyapatite (HAP) is the final product of bone biomineralization process and HAP formation is controlled by proteins, enzymes and small molecules secreted to extracellular matrix (ECM). Among these molecules, alkaline phosphatase (ALP) leads formation of HAP crystals and noncollagenous proteins control crystal nucleation and growth, and inhibit crystal formation. Osteocalcin (OCN) and osteopontin (OPN), are the most abundant noncollagenous proteins in ECM, which controls mineralization events. In this study, effect of OCN and OPN on HAP crystal formation was studied in order to achieve controlled crystal growth. In vitro biomineralization assays were conducted to understand the effect of OCN and OPN on the crystal structure of as formed minerals. While OCN decreases crystal growth rate and inhibit mineralization, which leads to more uniform crystal formation, OPN provides faster mineral formation with reduced Ca/P ratio. Moreover, a mammalian engineered cell line was constructed to achieve expression of bone extracellular

matrix (ECM) proteins. For this purpose, genetic cassettes were produced to express OCN and OPN proteins, which are the most common non-collagen proteins that control bone mineral formation. By this way, production of bone type minerals with controlled size, shape and Ca/P ratio can be possible. Our system provides a truly biomimetic approach to HAP formation compared to chemical synthesis methods in literature. We believe our current findings will lead to innovative approaches for bone biomineralization in regenerative medicine and bone tissue engineering.

Keywords: Osteocalcin, Osteopontin, ALP Enzymatic Activity, Biomineralization, Genetically Modified Cells

ÖZET

GENETİĞİ DEĞİŞTİRİLMİŞ HÜCRELER İLE BİYOMİNERALİZASYONUN SAĞLANMASI

Elif ERGÜL

Malzeme Bilimi ve Nanoteknoloji, Doktora

Tez Danışmanı: Urartu Özgür Şafak Şeker

Ağustos, 2019

Hidroksiapatit (HAP), kemik biyomineralizasyon işleminin son ürünüdür ve HAP oluşumu, hücre dışı matrikse (ECM) salgılanan proteinler, enzimler ve küçük moleküller tarafından kontrol edilir. Bu moleküller arasında, alkalin fosfataz (ALP), HAP kristallerinin oluşmasını sağlar ve kolajen olmayan proteinler, kristal çekirdeklenmesini, büyümesini kontrol eder ve kristal oluşumunu inhibe eder. Osteokalsin (OCN) ve osteopontin (OPN), mineralizasyon olaylarını kontrol eden ve ECM' de en çok bulunan kolajen olmayan proteinlerdir. Bu çalışmada, kontrollü kristal büyümesini sağlamak için OCN ve OPN'nin HAP kristal oluşumu üzerindeki etkisi incelenmiştir. OCN ve OPN'nin oluşan minerallerin kristal yapısı üzerindeki etkilerini anlamak için *in vitro* biyomineralizasyon deneyleri yapılmıştır. OCN kristal büyümesini azaltır, daha düzgün kristal oluşumuna yol açar ve mineralizasyonu inhibe ederken, OPN Ca / P oranını düşürür ve daha hızlı mineral oluşumu sağlar.

Ayrıca, kemik hücre dışı matrisinde bulunan proteinlerin ifade edilmesini sağlamak amacıyla genetiği değiştirilmiş bir hücre hattı oluşturulmuştur. Bu amaçla, kemik

mineral oluşumunu kontrol eden, en çok bulunan kolajen olmayan proteinler olan OCN ve OPN proteinlerini ifade edebilecek genetik kasetler oluşturulmuştur. Bu şekilde, boyut, şekil ve Ca / P oranı kontrol edebilmek ve kemik tipi mineraller üretmek mümkün olabilecektir. Sistemimiz, literatürdeki kimyasal sentez yöntemleriyle karşılaştırıldığında HAP oluşumuna biyomimetik bir yaklaşım sunmaktadır. Mevcut bulgularımızın, rejeneratif tıp ve kemik dokusu mühendisliğinde, kemik biyomineralizasyonunda yenilikçi yaklaşımlara yol açacağına inanıyoruz.

Anahtar kelimeler: Osteocalcin, Osteopontin, ALP Enzim Aktivitesi, Biyomineralizasyon, Genetiği Değiştirilmiş Hücreler

ACKNOWLEDGEMENTS

It seems that it has taken 8 years to complete PhD program. For me, it was more than that. It has started when I started primary school when I am 7 years old by learning reading, writing and math. Since then, I am a bookworm and a fond of learning. Last 8 years of my life was full of experience and experiment, failure and success, cry and laugh, and; sorrow and proud. Now, it has ended for a new beginning.

First, I would like to thank Dr. Urartu Şeker for guiding me in my thesis work. He is an incredibly virtuous person and a dedicated, passionate scientist. I am so happy to work with him in my PhD journey. I would also thank to Dr. Esra Yuca for guiding me in my projects. She is an excellent troubleshooter, no experiments can be left half finished with her consistency. I also want to thank to Recep Erdem Ahan and Ebru Şahin Kehribar for helping me in my thesis work. I want to thank to all SBL group members; Ebru Şahin Kehribar, Recep Erdem Ahan, Behide Saltepe, Musa Efe Işılak, Aslıhan Gökaltun, Merve Erden, Julian Ostoku, Gökçe Çelik, Zafer Koşar, Çisil Köksaldı, Selin Su Yirmibeşoğlu, Nedim Hacıosmanoğlu, Özge Begli, Cemile Elif Özçelik, Büşra Merve Kırpat, Sıla Köse, Merve Yavuz, Tolga Tarkan Ölmez, Ebuzer Kalyoncu, Tuğçe Önür and Onur Apaydın. Without them, such a nice and fruitful working environment could not be possible.

I would like to acknowledge all the support coming from my best friends. Hikmet Taner Teker was my best supporter since my undergraduate years both mentally and intellectually. Ebru Şahin Kehribar is both a close friend for me and a college to discuss scientific research, her presence in SBL lab gave me strength all the time.

Recep Erdem Ahan is somehow weird person, but he is so clever, talented and supportive. Dr. Rashad Mammadov was one of the best scientist in the world, I am happy to work with him and learn from him in my first year of PhD. His wisdom, advices and support had great contribution on my acquired skills. Dr. Nuray Gündüz is another passionate scientist graduated from UNAM, she was always supportive in my hard times, her advices from a different perspective helped me guide my life in my own way. I also thank her for pushing me positively to make me work harder.

Above every person that I want to thank to, I would like to thank my mother, Emine Duman and my father, Hüseyin Duman. They always supported my education and my journey to become a scientist. Without their effort on educating their daughters in spite of all odds, I could not be a women in science. I cannot skip to say that my sisters, Hümeyra Duman and Fatma Türker, was as supportive as my parents. Hümeyra was both my baby sitter from time to time and my lawyer; and Fatma was my life coach. I am so happy to have two sisters now, even though the years of childhood leading a cat and dog life.

The most challenging part of the PhD was becoming a scientist and a mother at the same time. However, whatever I learned from motherhood helped me to be a good researcher, and vice versa. I would like to thank to my daughters, İpek Ergül and Sedef Ergül, for making me who I am today. I would like to thank to all my babysitters, taking care of my children while I am working. Günay Parlak, she is like an older sister for me, Ayşe Tiryaki, Muhammet Ergül, Yıldız Köksal, Emine Duman, Hüseyin Duman, Hümeyra Duman, Rabia Kuşçu. Hatice Üzümcü, Gözde Yiğit Güneş, Fadime Acar, Öznur Çeliköz were the teachers of my daughters in kindergarten. I want to thank to these compassionate teachers for compensating the

odds of being a student mom. All helped me to raise my children and complete my thesis work. I also thank to Dr. Urartu Şeker for supporting me in the hard times of parenthood and integrating me to his group in spite of all the odds of being a mother. I hope scientist will take advantage of child care support provided by universities or governments in the future. Nobody starts his/her life at age 18, so having children should be something normal in academia.

It is impossible to thank to all the people who help me in my thesis, there are lots of hidden figures. All the members of UNAM, Bilkent University, the people who take part in the construction of the university and the institution, the people who fix technical problems that we faced, the people who keep the environment clean... I wish I would thank to all of them.

I want to thank to the contributors of my PhD thesis projects. During my thesis, I worked with Dr. Esra Yuca, in cloning, protein purification and biomineralization experiments. Ebru Şahin Kehribar helped me in optimization of protein purification, Recep Erdem Ahan in cloning, Behide Şaltepe for designing cloning experiments, Onur Apaydın for conducting MTT assay. I want to thank to all group members and engineers who educate me and make me gain all the skills. I want to thank to Dr. Serkan Kasırga for fruitful advises in EDS data analysis.

Lastly, I would like to acknowledge the PhD scholarship from TÜBİTAK (The Scientific and Research Council of Turkey) BIDEB 2211-A.

1 TABLE OF CONTENTS

2 CHAPTER I: INTRODUCTION 1

2.1 The mechanism of biomineralization in mammalian hard tissues 1

2.2 Currents strategies to mimic hard tissue extra cellular matrix 2

2.3 Expression of recombinant proteins in *E. coli* 4

2.4 The significance of the method used in this study to control crystal behavior 5

2.5 The significance of the method used in this study to engineer mammalian cells by bone mineralizing factors 6

3 CHAPTER II: BIOMINERALIZATION OF CALCIUM PHOSPHATE CRYSTALS CONTROLLED BY PROTEIN–PROTEIN INTERACTIONS 7

3.1 Objective 7

3.2 Materials And Methods 8

3.2.1 Cell strains, growth, cell maintenance and transformation 8

3.2.2 Construction of plasmid maps and cloning 9

3.2.3 Sequence alignments 12

3.2.4 Expression of recombinant proteins in E. coli 12

3.2.5 Purification of recombinant proteins 13

3.2.6 Verification of expression and purification 17

3.2.7 Protein quantitation 19

3.2.8 Analysis of enzyme kinetics 20

3.2.9 Secondary structure analysis by circular dichroism (CD) measurement 21

3.2.10 Biomineralization of calcium and phosphate in the presence of recombinant proteins 22

3.3 Results and Discussion 25

3.3.1 Cloning, expression and purification 25

3.3.2 Effect of recombinant proteins on enzyme kinetics 39

3.3.3 Secondary structure analysis 41

3.3.4 Effect of recombinant proteins on ALP-mediated *in vitro* biomineralization 45

4 CHAPTER III: ENGINEERING CELLS FOR BIOMINERALIZATION 66

4.1 Objective 66

4.2 Materials and Methods 67

4.2.1 Cell Lines 67

4.2.2 Differentiation of Pre-Osteoblast Cells 68

4.2.3 Plasmid construction 68

4.2.4 Transfection 69

4.2.5 mRNA and protein isolation 69

4.2.6 Quantitative Real Time PCR (qRT-PCR) 71

4.2.7 Immunocytochemistry (ICC) 71

4.3 RESULTS AND DISCUSSION 72

4.3.1 Cloning, expression and purification 72

4.3.2 Transient transfection of mammalian cells for OCN and OPN expression 79

5 CHAPTER IV 86

5.1 CONCLUSION 86

5.2 BIBLIOGRAPHY 89

5.3 APPENDIX A 95

5.3.1 DNA sequences of genes and gene fragments 95

5.4 APPENDIX B 104

5.4.1 List of primers 104

5.5 APPENDIX C 107

5.5.1 Plasmid maps 107

5.6 APPENDIX D 112

5.6.1 Sanger sequencing results 112

5.7 APPENDIX E 116

5.7.1 Amino acid sequences of proteins 116

5.8 APPENDIX F 120

5.9 APPENDIX G 121

5.9.1 Secondary structure analysis. 121

5.10 APPENDIX H 1

5.10.1 Comparison of commercial HAP with CaP crystals in our system 1

LIST OF TABLES

Table A1. Nucleotide sequences of phoA, GST-OCN, OCN and OPN genes. 95
Table A2. Nucleotide sequences of cDNAs. 101

Table B1. Nucleotide sequences of primers used in cloning ALP, OCN and OPN genes. 104
Table B2. Nucleotide sequences of primers used in qRT-PCR reactions. 106

Table E1. Amino acid sequences of ALP, GST-OCN, OCN and OPN proteins. 116
Table E2. Amino acid sequences of mouse pre-osteoblast derived OCN and OPN proteins. 119

Table G1. Secondary structure prediction by Bestsel online tool. Secondary structure analysis of OCN and OPN proteins and their changes upon addition of $CaCl_2$ (Ca^{2+}), β-GP (organic phosphate, P) and Na_2HPO_4 (inorganic phosphate, P_i). The analysis was done based on the protocol described elsewhere. (Micsonai, Wien et al. 2015). 121

LIST OF FIGURES

Figure 1. Graphical illustration depicting the effect of size/shape/CaP ratio controlled HAP scaffold on differentiation of osteoblast cells and induction of mineralization. In the presence of Ca^{2+} ions and organic phosphate source, pre-osteoblasts can differentiate into osteocyte cells and deposit inorganic matrix. HAP scaffold hastens mineral deposition and propagates osteoblast differentiation. 5
Figure 2. Graphical illustration depicting the effect of bone related proteins on reprogramming of somatic cells and induction of mineralization. In the presence of bone mineralizing proteins, Ca^{2+} ions and organic phosphate source, somatic cells can secrete inorganic matrix..... 6
Figure 3. ALP is a conserved enzyme and functions similarly in several organisms. Multiple sequence alignment of ALP proteins from 4 selected organisms is performed by Clustal Omega and is partially shown. 26
Figure 4. Amplification of phoA gene from bacterial genomic DNA. DH5α genomic DNA was used as a template to amplify *phoA* gene. PCR reaction was performed according to the protocol of Q5 Polymerase (NEB). 2-log DNA ladder (NEB) was used for detection. 26
Figure 5. Schematic diagram of ALP expression cassette. Native periplasmic space localization sequence was replaced with pelB periplasmic space localization peptide. His-tag was added after pelB to the N-terminal of the protein for detection of expression and purification. GS linker provide flexibility to His-tag. T7 promoter and terminator were used for expression by T7 polymerase. 27
Figure 6. OCN gene was amplified by PCR. Synthetic OCN gene fragment was used as template in PCR. PCR reaction was performed according to the protocol of Q5 Polymerase (NEB). 50 bp ladder (NEB) was used for detection. 28
Figure 7. Schematic diagram of OCN expression cassette. GST tag added to the N-terminal of the protein for enhancing solubility, expression and purification. TEV recognition site was inserted between GST and OCN for removing GST after expression. His-tag was added to the C-terminal of the protein for detection of expression and purification. T7 promoter and terminator were used for expression by T7 polymerase. 29

Figure 8. OPN gene was amplified by PCR. Synthetic OPN gene fragment was used as template in PCR. PCR reaction was performed according to the protocol of Q5 Polymerase (NEB). 2-log DNA ladder (NEB) was used for detection. 30
Figure 9. Schematic diagram of OPN expression cassette. His-tag was added to the C-terminal of the protein for detection of expression and purification. T7 promoter and terminator were used for expression by T7 polymerase..... 30
Figure 10. Agarose gel electrophoresis image of pEt22b-ALP plasmid verification by restriction enzyme digestion. Uncut plasmid was used as digestion control (Lane 2). 3 colonies was selected to verify insertion of ALP into pEt22b by HindIII digestion (Lanes 3-5). Last plasmid in image has a higher band (6500 bp vs. 5000 bp), which verifies insertion. The ladder was 2-log DNA ladder (NEB) in Lane 1. 31
Figure 11. Agarose gel electrophoresis image of pGEX-6P1-OCN plasmid verification by restriction enzyme digestion. Uncut plasmid was used as digestion control (Lane 2). 2 colonies was selected to verify insertion of OCN into pGEX-6P1 by BamHI and EcoRI digestion (Lanes 3-4). Last plasmid in image has a band (300-400 bp), which verifies insertion. The ladder was 2-log DNA ladder (NEB) in Lane 1..... 32
Figure 12. Agarose gel electrophoresis image of pEt22b-OPN plasmid verification by restriction enzyme digestion. Uncut plasmid was used as digestion control (Lane 2). One of the colonies was selected to verify insertion of OPN into pEt22b by NotI and XhoI digestion (Lane 3). Last plasmid in image has a band (900 bp), which verifies insertion. The ladder was 2-log DNA ladder (NEB) in Lane 1. 33
Figure 13. Phosphatase assay detects overexpression of ALP in transformed cells. Overexpression of ALP in periplasmic extract of pET22b-ALP bacteria (A) compared to that of control bacteria (B) after 4 hour IPTG (1 mM) induction at 200 RPM, 37 ºC. 34
Figure 14. Purification of ALP by IMAC detected by SDS-PAGE analysis. Lane 1 Page Ruler (NEB) ladder, Lane 2 cell lysate, Lane 3 purified ALP. Purification was done by either Cobalt resin or Ni-NTA resin..... 35
Figure 15. Purification of ALP by IMAC detected by Western blot analysis. Lane 1 Page Ruler (NEB) ladder, Lane 2 purified ALP. Detection was done by anti-his-tag primary antibody, HRP-conjugated secondary antibody and ECL substrate..... 35
Figure 16. Purification of OCN detected by SDS-PAGE. Image 1: Lane 1 Page Ruler (NEB) ladder, Lane 2 cell lysate, Lane 3 purified GST-OCN (36 kD). Purification

was done by either Cobalt resin or Ni-NTA resin. Image 2: Lane 1 Spectra Low Range (NEB) ladder, Lane 2 GST (26 kD) and OCN (10 kD) were cut by TEV protease. Image 3: Lane 1 Page Ruler (NEB) ladder, Lane 2 OCN (10 kD), Lane 3 GST (26 kD). Purification was done by GST bind resin. 36
Figure 17. Purification of OCN by IMAC detected by Western blot analysis. Image 1: Lane 1 Page Ruler (NEB) ladder, Lane 2 purified GST-OCN (36 kD). Image 2: Lane 1 Spectra Low Range (NEB) ladder, Lane 2 GST-OCN (36 kD), GST (26 kD) and OCN (10 kD). GST-OCN were cut by TEV protease. Detection was done by anti-his-tag primary antibody, HRP-conjugated secondary antibody and ECL substrate..... 37
Figure 18. Purification of OPN by IMAC detected by SDS-PAGE analysis. Lane 1 Page Ruler (NEB) ladder, Lane 2 cell lysate, Lane 3 purified OPN. Purification was done by either Cobalt resin or Ni-NTA resin..... 38
Figure 19. Purification of OPN by IMAC detected by Western blot analysis. Lane 1 Page Ruler (NEB) ladder, Lane 2 purified OPN. Detection was done by anti-his-tag primary antibody, HRP-conjugated secondary antibody and ECL substrate..... 38
Figure 20. Michaelis-Menten kinetic analysis of ALP activity in the presence of OCN and OPN. A. ALP activity in the presence of OCN or OPN. B. V_{max} and K_m of ALP in the presence of OCN or OPN. K_m (μM), the reaction rate constant, increased in the presence of OCN and OPN. C. ALP activity in the presence of varying concentrations of OCN and OPN. D. v_{max} and k_m of ALP in the presence of OCN and OPN. K_m, the reaction rate constant, increased in the presence of varying concentrations of OCN and OPN. V_{max} (μM pNP/min) is constant for all cases. Experiment was performed in triplicate. Nonlinear regression curve fitting was performed to fit experimental data on Michaelis-Menten curve (A-C). TWO-WAY ANOVA was performed to compare each group with ALP only group (B-D). V_{max} was not statistically significant while k_m significantly increased for all groups..... 40
Figure 21. CD spectrum measurement for secondary structure analysis of OCN and OPN in the presence of biomineralization molecules. A.OCN helical and anti parallel structures was increased following the addition of Ca^{2+}. B-C. α-helical structure of OCN is disrupted in the presence of inorganic phosphate, not organic phosphate. D. Secondary structure of OPN following the addition of Ca^{2+} is largely conserved. E-F. OPN becomes more compact in the presence of inorganic phosphate, not the organic phosphate. 44

Figure 22. *In vitro* biomineralization in the presence of ALP and OCN-P_i. A. Initial mineral formation was detected by spectrophotometer when OCN and ALP were added into the reaction before BB (Ca^{2+} and β-GP). Initial mineral formation rate was calculated based on first 30 minutes of mineral formation. The legends in the first graphic are also valid for the columns in $k_{observable}$ graphic. Statistical analysis was performed in Graphpad Prism software by One-Way ANOVA. BB: 24 mM $CaCl_2$, 14.4 mM β-GP, 25 mM Tris-HCl (pH=7.4) ALP (5 U), 1 mM $MgCl_2$ used for each reaction. All samples are in 25 mM Tris-HCl, pH=7.4. 47
Figure 23 *In vitro* biomineralization in the presence of ALP and OCN-Ca^{2+}. A. Initial mineral formation was detected by spectrophotometer when OCN and BB Ca2+ and β-GP) were added into the reaction before ALP. Initial mineral formation rate was calculated based on first 30 minutes of mineral formation. The legends in the first graphic are also valid for the columns in $k_{observable}$ graphic. Statistical analysis was performed in Graphpad Prism software by One-Way ANOVA. BB: 24 mM $CaCl_2$, 14.4 mM β-GP, 25 mM Tris-HCl (pH=7.4) ALP (5 U), 1 mM $MgCl_2$ used for each reaction. All samples are in 25 mM Tris-HCl, pH=7.4..... 47
Figure 24. Electron microscopy imaging of *in vitro* biomineralization in the presence of ALP and OCN. A. SEM imaging of mineral formation in the presence of ALP after 24 h of incubation at 37 ˚C. B. SEM imaging of mineral formation in the presence of ALP and OCN after 24 h of incubation at 37 ˚C. A-B. Scale bars represent 1 µm. C. Crystal size is measured by the ImageJ program measure tool from SEM images from N=20 ± SEM and N=18 ± SEM crystals. Unpaired t-test was performed to analyze statistical significance. BB: 24 mM $CaCl_2$, 14.4 mM β-GP, 25 mM Tris-HCl (pH=7.4) ALP (5 U), 1 mM $MgCl_2$ used for each reaction. All samples are in 25 mM Tris-HCl, pH=7.4. 49
Figure 25. Ca:P ratio of the minerals formed in the presence of ALP and OCN after 24 h of incubation at 37 ˚C detected by XPS and EDS, respectively. 3 points with 400 µm spot size were selected for XPS scanning. Unpaired t-test was performed to analyze statistical significance. 5-6 points were selected EDS analysis. One-Way ANOVA was performed to analyze statistical significance..... 52
Figure 26. Schematic representation of the reaction with ALP in the absence of OCN, and ALP was added into reaction before or after BB (Ca^{2+} and β-GP). 53
Figure 27. *In vitro* biomineralization in the presence of ALP and OPN-Ca^{2+}. Initial mineral formation was detected by spectrophotometer when BB and OPN added into

the reaction before ALP. Initial mineral formation rate was calculated based on first 30 min of mineral formation. (Error bars represents N=3 ± SEM.) The legends in spectrophotometry measurement graphic are also valid for the columns in $k_{observable}$ graphics. Statistical analysis was performed in Graphpad Prism software by One-Way ANOVA. BB: 24 mM $CaCl_2$, 14.4 mM β-GP, 25 mM Tris-HCl (pH=7.4) ALP (5 U), 1 mM $MgCl_2$ used for each reaction. All samples are in 25 mM Tris-HCl, pH=7.4..... 55
Figure 28. In vitro biomineralization in the presence of ALP and OPN-P_i. Initial mineral formation detected by spectrophotometer when ALP and OPN added into the reaction before BB. Initial mineral formation rate was calculated based on first 30 min of mineral formation. (Error bars represents N=3 ± SEM.) The legends in spectrophotometry measurement graphic are also valid for the columns in $k_{observable}$ graphics. Statistical analysis was performed in Graphpad Prism software by One-Way ANOVA. BB: 24 mM $CaCl_2$, 14.4 mM β-GP, 25 mM Tris-HCl (pH=7.4) ALP (5 U), 1 mM $MgCl_2$ used for each reaction. All samples are in 25 mM Tris-HCl, pH=7.4..... 55
Figure 29. A.SEM imaging of mineral formation in the presence of ALP after 24 h of incubation at 37 ˚C. B. SEM imaging of mineral formation in the presence of ALP and 3 µM OPN after 24 h of incubation at 37 ˚C. A-B. Scalebars represent 1µm. C. Crystal size is measured by the ImageJ program measure tool from SEM images from N=14 ± SEM and N=21 ± SEM crystals. Unpaired t-test was performed to analyze statistical significance. 57
Figure 30. Surface Ca:P ratio of the minerals formed in the presence of ALP and OPN after 24 h of incubation at 37 ˚C detected by XPS. 3 points with 400 µm spot size are selected for scanning. ONE-WAY ANOVA was performed to analyze statistical significance of each sample compared to ALP. 58
Figure 31. Illustration of initial and late phases of CaP crystal formation in the presence of ALP only, and both ALP and OPN..... 60
Figure 32. *In vitro* biomineralization in the presence of ALP and varying concentrations of OCN and OPN. Initial mineral formation detected by spectrophotometer. Initial mineral formation rate calculated based on first 40 min of mineral formation (ONE-WAY ANOVA). BB: 24 mM $CaCl_2$, 14.4 mM β-GP, 25 mM Tris-HCl (pH=7.4) ALP (5 U), 1 mM $MgCl_2$ used for each reaction. All samples are in 25 mM Tris-HCl, pH=7.4. 62

Figure 33. SEM imaging of mineral formation after 24 h of incubation at 37 ˚C in the presence of ALP only, ALP and 3 µM OPN, ALP and 1 µM OCN, and ALP, combination of, 3 µM OPN and 1µM OPN, respectively. Scalebars represents 1 µm. 63
Figure 34. Ca:P ratio of the minerals formed in the presence of ALP and OCN after 24 h of incubation at 37 ˚C detected by EDS. 5-6 points were selected EDS analysis. One-Way ANOVA was performed to analyze statistical significance. 64
Figure 35. Illustration of initial and late phases of CaP crystal formation in the presence of ALP only, and ALP, OCN and OPN. 65
Figure 37. Differentiation of MC3T3 cells for osteoblastic gene expression. Alizarin Red Staining indicates CaP crystal formation of MC3T3 cells differentiated in osteogenic medium for 14 days. Scalebar represents 100 µm. 73
Figure 38. Schematic diagram of mOCN expression cassette. Kozak translation initiation sequence was added for enhanced expression. His-tag was added after a GS linker to the C-terminal of the protein for detection of expression. GS linker provides flexibility to His-tag. CMV promoter and BGH terminator were used for constitutive mammalian gene expression. 74
Figure 39. mOCN gene was amplified by PCR. mOCN cDNA was used as template in 2-step PCR. PCR reaction was performed according to the protocol of Q5 Polymerase (NEB). 2-log DNA ladder (NEB) was used for detection. Tm1= 53-62 ºC (55 ºC best), Tm2= 82 ºC. All temperatures worked. Lane 1: 2 log DNA Ladder (NEB) Lane 2-6: Gradient PCR reactions..... 74
Figure 40. Linearization of plasmid vector pCDNA3-eGFP with HindIII and XbaI digestion. Lane 1 2-log DNA Ladder (NEB), Lane 2-3 double digested plasmid, Lane 4 uncut plasmid control..... 75
Figure 41. Verification of mOCN-pCDNA3 Gibson Assembly. Restriction enzyme digestion was performed with EcoRI and KpnI. Lane 1: Ladder, Lane 2: uncut plasmid for 1st colony, Lane 3: Double digested plasmid. Lane 4: uncut plasmid for 2nd colony, Lane 5: Double digested plasmid. Lane 6: uncut plasmid for 3rd colony, Lane 7: Double digested plasmid. Lane 8: uncut plasmid for 4th colony, Lane 9: Double digested plasmid. Lane 10: uncut plasmid for 5th colony, Lane 11: Double digested plasmid..... 76
Figure 42. Schematic diagram of mOPNa expression cassette. Kozak translation initiation sequence was added for enhanced expression. His-tag was added after a GS

linker to the C-terminal of the protein for detection of expression. GS linker provides flexibility to His-tag. CMV promoter and BGH terminator were used for constitutive mammalian gene expression. 77
Figure 43. mOPNa gene was amplified by PCR. mOPNa cDNA was used as template in 2-step PCR. PCR reaction was performed according to the protocol of Q5 Polymerase (NEB). 2-log DNA ladder (NEB) was used for detection. Lane 1: 2-log DNA Ladder (NEB), Lane 2-6: mOPNa. cDNA library template was amplified at 62-72 ˚C interval. 900 bp expected band was visible on gel. 77
Figure 44. Colony PCR of mOPNa-pCDNA3 plasmid construct with PFU Polymerase. Lane 1: Ladder, Lane 2-5: mOPNa colonies 1-4 amplified at 67 ˚C, Lane 6: mOPNa plasmid (positive control). 78
Figure 45. Transfection of HEK293 cells with pCDNA-eGFP and PEI. 1:3 DNA:PEI ratio was used. PEI was prepared in 0.1 N HCl and in 100% EtOH, respectively. 10^5 cells were seeded each well in 24 well plate and they were allowed to grow for 24 h. 500 ng DNA was used for each group. DNA and PEI were premixed in serum-free DMEM 20 min before transfection. Images were taken 24 hours after transfection by an inverted fluorescent microscope. 80
Figure 46. Detection of mOCN and mOPNa mRNA levels in HEK293 cells by qRT-PCR. cDNA library was created from equal amount of mRNA from each biological triplicate before qRT-PCR. Equal amount of cDNA was used in technical triplicate. hGAPDH gene was used to normalize gene expression levels. Untransfected HEK293 cells were used as negative control to calculate relative expression levels. 81
Figure 47. Protein expression analysis of mOCN in HEK293 cells by SDS-PAGE. Image 1. Cell lysate. Lane 1: Page Ruler Ladder (NEB), Lane 2: Untransfected cells. Lane 3: mOCN transfected cells after 48 h culture with plasmid. Image 2. Cell culture supernatant. Lane 1: Page Ruler Ladder (NEB), Lane 2: Control cells without transfection cultured in the presence of osteogenic medium for 48 h, Lane 3: mOCN transfected cells after 48 h culture with plasmid. 82
Figure 48. Protein expression analysis of mOPNa in HEK293 cells by SDS-PAGE. Image 1. Cell lysate. Lane 1: Page Ruler Ladder (NEB), Lane 2: Untransfected cells. Lane 3: mOPNa transfected cells after 48 h culture with plasmid. Image 2. Cell culture supernatant. Lane 1: Page Ruler Ladder (NEB), Lane 2: Control cells without transfection cultured in the presence of osteogenic medium for 48 h, Lane 3: mOPNa transfected cells after 48 h culture with plasmid. 82

Figure 49. Protein expression analysis of mOPNa in HEK293 cells by Western Blotting. Cell lysate. Lane 1: Page Ruler Ladder (NEB), . Lane 2: Control cells without transfection cultured in the presence of osteogenic medium. Lane 3: mOCN transfected cells, Lane 3: mOPNa transfected cells. Western Blot analysis was performed 48 h after transfection. 83
Figure 50. Protein expression analysis of mOCN and mOPNa in HEK293 cells by ICC. A,D. Untransfected HEK293 cells. B,E. mOCN transfected HEK 293 cells. C,F. mOPNa transfected HEK 293 cells. His Tag Monoclonal Antibody (HIS.H8) was used in 1:300 dilution in 5% milk powder in 1X PBS as primary antibody. Pierce Goat anti-Mouse IgG (H+L) Cross Adsorbed Secondary Antibody, DyLight 550 was used in 1:600 dilution in 5% milk powder in 1X PBS as secondary antibody. Images were taken fluorescent microscope. A-C. Overlay of brightfield and fluorescent images. D-F. Fluorescent staining images. Scalebars represents 50 µm. 85

Figure C1. Schematic representation of pEt22b-pelB-6H-ALP plasmid. 107
Figure C2. Schematic representation of pGEX-6P1-GST-OCN-6H plasmid..... 108
Figure C3. Schematic representation of pEt22b-OPN-6H plasmid. 109
Figure C4. Schematic representation of pCDNA3-OCN-4H plasmid. 110
Figure C5. Schematic representation of pCDNA3-OPN-4H plasmid. 111

Figure D 1. Sequencing alignment of pEt22b-ALP construct with phoA gene sequence. Analysis performed in Geneious R9.0.5 Software.
(Score = 5475.0, Identities = 1189/1458 (81%),
Positives = 1189/1458 (81%), Gaps = 261/1458 (17%)) 112
Figure D 2. Sequencing alignment of pGEX-6P1-GST-OCN-6H construct with synthetic OCN gene fragment sequence. Analysis performed in Geneious R9.0.5 Software. Score = 1170.0, Identities = 234/1151 (20%),
Positives = 234/1151 (20%), Gaps = 917/1151 (79%) 113
Figure D3. Sequencing alignment of pEt22b-OPN-6H construct with synthetic OPN gene fragment sequence. Analysis performed in Geneious R9.0.5 Software.
Score = 4275.0, Identities = 855/1230 (69%),
Positives = 855/1230 (69%), Gaps = 375/1230 (30%) 114

Figure D4. Sequencing alignment of pCDNA3-mOCN-4H construct with mOCN cDNA sequence. Score = 4835.75, Identities = 1013/5710 (17%), Positives = 1076/5710 (18%), Gaps = 4632/5710 (81%) 114
Figure D5. Sequencing alignment of pCDNA3-mOPNa-4H construct with mOPNa cDNA sequence. Score = 1500.0, Identities = 293/307 (95%), Positives = 293/307 (95%), Gaps = 13/307 (4%) 115
Figure D6. Sequencing alignment of pCDNA3-mOPNa-4H (K30) and pCDNA3-mOPNa-4H (K30, D87Y) constructs with mOPNa cDNA sequence. First colony does not contain missense mutation while second colony has missense mutation. . 115

Figure F1. Standard curve for pNP concentration. ($y = 47.19x - 1.655$, $R^2 = 0.998$) 120
Figure F 2. Determination of ALP unit enzyme concentration. ($y = 0.546x - 0.008$, $R^2 = 0.997$) 1 U enzyme corresponds to the 1.98 fold ALP, which generates 1 µM pNP in 1 min. 120

Figure G1. Secondary structure analysis of OCN and OPN proteins and their changes upon addition of $CaCl_2$ (Ca^{2+}), β-GP (organic phosphate, P) and Na_2HPO_4 (inorganic phosphate, P_i). The analysis was done based on the protocol described elsewhere with Bestsel online tool.(Micsonai, Wien et al. 2015)..... 123

Figure H 1. Comparison of Ca:P ratio of the CaP crystals in our system with the commercial HAP. Ca:P ratio was calculated by XPS and EDS, respectively. Measurements were done after 24 h of incubation at 37 ˚C. A. 3 points with 400 µm spot size were selected for XPS scanning. B. 5-6 points were selected EDS analysis. Unpaired t-test was performed to analyze statistical significance. 1

2 CHAPTER I: INTRODUCTION

2.1 The mechanism of biomineralization in mammalian hard tissues

Bone tissue is composed of a dense extracellular matrix which is synthesized by two main cell types: osteoblasts and osteocytes, and degraded by another cell type, osteoclasts, each are differentiated from bone marrow stromal cells. (Liu, Luo et al. 2016) Osteoblasts are responsible for the formation of the organic part of the matrix, including Collagen (type I) 90%, noncollagenous proteins, proteoglycans, glycosaminoglycans and lipids. Osteocytes are terminally differentiated forms of osteoblasts and they synthesize and are trapped inside inorganic matrix, primarily hydroxyapatite ($Ca_5(PO_4)_3(OH)_2$) crystals. (Crichton 2012)

HAP formation in bone is composed of two phases. In the first phase, matrix vesicles (MVs), which are membranous compartments, are released from osteoblasts. ALP is found both in ECM and in the membrane of MVs, and converts organic phosphate into inorganic phosphate (P_i). Ca^{2+} and P_i ions are internalized from ECM and amorphous CaP crystals are formed inside MVs. Amorphous CaP crystals were converted to octa-CaP (OCP) crystals, and OCP crystals were converted to HAP crystals. In second phase, HAP crystals penetrate MV membrane and secreted to the ECM. Continued nucleation of hydroxyapatite crystals in ECM is controlled by the levels of extra-vesicular Ca^{2+}, P_i, and H^+, as well as Ca^{2+}-binding proteins including Collagen I, OCN, and OPN. (Golub 2009)

Collagen I is the most abundant protein in ECM of bone and serves as a template for the growth of crystals in parallel orientation. It is composed of triple helical fibers, and mineralization starts in gap regions of these fibers. (Crichton 2012) However, the presence of collagen I is not enough for mineralization, noncollagenous proteins (NCPs) play important roles in controlling mineralization process. NCPs control size, shape and Ca/P ratio of the crystals, inhibit mineralization to prevent excessive calcification and to provide c-axis elongated growth of crystals, and provide uniformity to the crystals. (Gehron Robey 2008) Mainly, there are two class of NCPs in bone ECM, gamma-carboxylated proteins, and small integrin-binding ligand, N-linked glycoproteins (SIBLINGs). OCN and OPN belongs to these families, respectively, and are the most abundant NCPs. OCN and OPN are both inhibitor of mineralization but OPN also acts as a nucleator when it is cross linked to the gap regions of the collagen fibers (Hauschka and Wians Jr 1989; Denhardt and Guo 1993; Ducy, Desbois et al. 1996; Kaartinen, Pirhonen et al. 1999).

2.2 Currents strategies to mimic hard tissue extra cellular matrix

Although hard tissues in the body are difficult to injure, the intrinsic healing capacity of these tissues is highly limited. (Edwards, Simmons et al. 1988) In addition, several diseases can affect homeostasis of bone and teeth, such as bone cancer, osteoporosis, and dental pulp infections. (Riggs and Melton 1986; Jemal, Siegel et al. 2008; Trope 2008) Commercial bone substitutes and dental prostheses for fracture healing and disease treatment are available. (Greenwald, Boden et al. 2001; Wittneben, Buser et al. 2014) However, the properties of these materials need to be enhanced in order to provide better osteointegration while controlling the bone regeneration rate and

preventing ectopic bone formation. (Puzas, Miller et al. 1989; Ai-Aql, Alagl et al. 2008)

Among synthetic bone substitutes, hydroxyapatite (HAP) grafts are one of the best in terms of their bioinertness and osteointegration capability. (Heise, Osborn et al. 1990; Landi, Celotti et al. 2003; Li, Yubao et al. 2005; Sadat-Shojai, Khorasani et al. 2013; Teotia, Raina et al. 2017). There are several methods for HAP synthesis; among them, wet chemical synthesis and high temperature synthesis are the most studied routes. (Sadat-Shojai, Khorasani et al. 2013) Despite their straightforward protocol, the methods suffer from many limiting factors. For example, wet chemical synthesis is the most promising method; however, precise control of crystallinity is not possible which yields a low number of ordered crystals and high impurity content. In addition, aging of crystals can take too long, which makes the process time-consuming. (Sadat-Shojai, Khorasani et al. 2013) High temperature synthesis of HAP can be a better alternative to wet synthesis in terms of a more pure phase composition and higher crystallinity, but it requires a high amount of energy to heat the sample up to 2000 ºC. (Sadat-Shojai, Khorasani et al. 2013)

Several organisms including mammalians can synthesize HAP crystals and other mineral forms. (Kirkham, Brookes et al. 2002) Organisms perform mineral synthesis with tight control mechanisms to provide high crystallinity and shape uniformity. Proteins, enzymes, and even small ions take part in this process. (D'Souza, Cavender et al. 1997; Gajjeraman, Narayanan et al. 2007; Abbarin, San Miguel et al. 2014; Ibsen, Gebauer et al. 2016; Siller Alejandro and Whyte Michael 2017; Tsao, Huang et al. 2017; O'Neill, Awale et al. 2018) These components possess important roles in hard tissue development, bone remodeling, and bone regeneration. (Romberg, Werness et al. 1986; Yang, He et al. 2011; Siller Alejandro and Whyte Michael

2017; O'Neill, Awale et al. 2018) Mimicking biological mineral formation has potential as a promising route for HAP synthesis, as the physiological conditions such as pH and temperature can be easily adapted to the *in vitro* environment. Synthesized HAP molecules can be better adapted to the host tissue environment by biomimetic mineral formation. (Kikuchi, Ikoma et al. 2004; Wang, Guan et al. 2007; Cai, Mei et al. 2010; Yang, He et al. 2011)

2.3 Expression of recombinant proteins in *E. coli*

Purification of proteins from bone tissue is a laborious work to study the interaction of these proteins *in vitro*. In addition, purification of the proteins may alter the secondary structure and functionality of the proteins since harsh conditions are applied during the extraction. (Prince, Oosawa et al. 1987) On the other hand, bacterial platforms are easy to handle for production and purification of recombinant proteins. (Guan and Dixon 1991; Baneyx 1999; Sørensen and Mortensen 2005; Choi, Keum et al. 2006; Structural Genomics, Architecture et Fonction des Macromolécules et al. 2008) Several bone-related proteins are successfully produced and purified in these platforms, and they were investigated for their biomineralization activities. (Sampath, Maliakal et al. 1992; Käkönen, Hellman et al. 1996; Smith, Cheung et al. 1996; Xiong, Yu et al. 2002; He, Dahl et al. 2003; Tartaix, Doulaverakis et al. 2004; Lee, Kim et al. 2012; Svensson Bonde and Bulow 2012; Yun, Kim et al. 2012)

2.4 The significance of the method used in this study to control crystal behavior

In this study, *in vitro* biomineralization of calcium phosphate (CaP) crystals was controlled in a truly biomimetic system composed of ALP, OCN and OPN, which are the main components of bone ECM. While ALP is enough for mineral formation, the reaction rate, size, and shape of the crystals were affected by the presence of OCN and OPN. Controlled HAP growth will improve construction of mammalian hard tissue environment-mimicking matrices and tissue scaffolds in order to provide bone healing at the fracture site. These matrices will be suitable candidates to host hMSCs and pre-osteoblast cells. Fine-tuning/manipulation of OCN-OPN concentrations and ratio can create a valuable platform to control biomineralization in bone regeneration and tissue repair. (Figure 1)

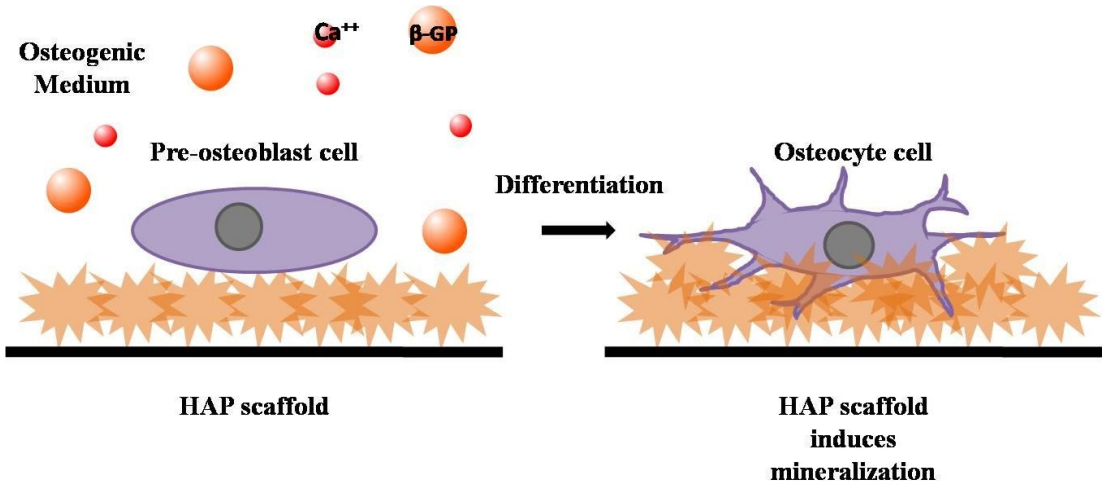

Figure 1. Graphical illustration depicting the effect of size/shape/CaP ratio controlled HAP scaffold on differentiation of osteoblast cells and induction of mineralization. In the presence of Ca^{2+} ions and organic phosphate source, pre-osteoblasts can differentiate into osteocyte cells and

deposit inorganic matrix. HAP scaffold hastens mineral deposition and propagates osteoblast differentiation.

2.5 The significance of the method used in this study to engineer mammalian cells by bone mineralizing factors

Differentiation of osteoblast cells from mesenchymal stem cells *in vitro* is a promising route for *in vitro* bone tissue formation. However, it is hard to isolate MSCs from human and the differentiation capacity of these cells varies from patient to patient. Therefore, a platform for generation of bone-type minerals by non-mineralizing somatic cell types is needed. Engineering of somatic cells is necessary to make them suitable for bone type mineral formation. In order to achieve this, bone ECM specific proteins were produced in mammalian cells. Main mineral-controlling proteins, OCN and OPN, were successfully produced in this work. They have huge potential to provide reprogramming somatic cells in order to achieve mineralization in different non-osteoblast cell lines. The reprogrammed cells can be a better alternative to the mesenchymal cells to provide bone tissue regeneration and healing at the fracture site. (Figure 2)

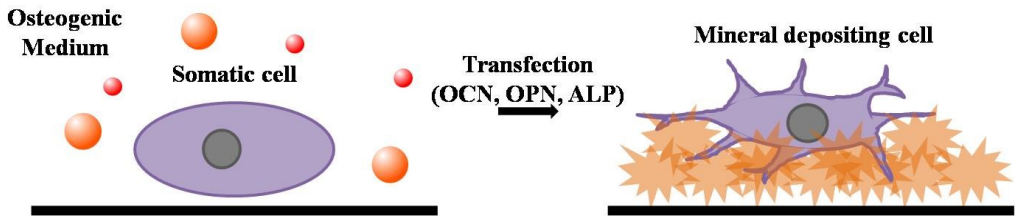

Figure 2. Graphical illustration depicting the effect of bone related proteins on reprogramming of somatic cells and induction of mineralization. In the presence of bone mineralizing proteins, Ca^{2+} ions and organic phosphate source, somatic cells can secrete inorganic matrix.

3 CHAPTER II: BIOMINERALIZATION OF CALCIUM PHOSPHATE CRYSTALS CONTROLLED BY PROTEIN–PROTEIN INTERACTIONS

3.1 Objective

Gene transfer from one organism to another by synthetic biology made production of proteins in different organisms possible. By this way, human proteins were successfully produced and isolated from bacterial and yeast cells with high yield and low cost. (Swartz 2001; Sanchez-Garcia, Martín et al. 2016) Production of insulin in bacterial cells was a breakthrough in recombinant protein technology, which eliminated the risk of immunogenicity of animal derived insulin and reduced the cost of exogenous insulin drugs used in diabetes treatment. (Keen, Pickup et al. 1980) Other drugs were also developed by recombinant technology including recombinant human erythropoietin for treatment of anemia, human growth hormone, for treatment of the growth hormone deficiency, recombinant hirudin for treatment of thrombotic disease. (Lee-Huang 1984; Shin, Kim et al. 1998; Tan, Wu et al. 2002; Choi and Lee 2004) For the treatment of bone-related diseases such as acute tibial fractures and osteoporosis, human bone proteins can be used directly or these proteins can be used for biomimetic mineral scaffold formation. (Liu, Luo et al. 2016)

In this part of my thesis project, expression and characterization of important bone mineralizing proteins, ALP, OCN, and OPN in bacterial platforms was achieved. Understanding and optimization of in vitro biomineralization activities with these

proteins gave us the opportunity to produce biomimetic minerals for bone regeneration applications.

3.2 Materials And Methods

3.2.1 Cell strains, growth, cell maintenance and transformation

E. coli DH5α strain was used in this study for cloning. *E. coli* DH5α strain contains mutations in recA1 and endA1 genes which increase transformation efficiency. Plasmid recombination is reduced and plasmid stability is increased by recA1, plasmid yield is improved by endA1. (Singer, Eiteman et al. 2009; Borja, Meza Mora et al. 2012) Cell stocks was prepared in freezing medium containing 25% glycerol in Lysogeny Both (LB) medium in order to maintain viability in the long term. *E. coli* BL21 (DE3) strain was used for protein expression and purification. This strain encodes T7 polymerase under the control of Lac promoter and is deficient of proteases for improving protein yield. (Jeong, Barbe et al. 2009) Both strains were inoculated in LB medium and incubated on LB agar at 30 or 37 ºC.

Chemical transformation was performed for the uptake of plasmids into bacterial cells. Chemically competent cells were prepared by TSS (Transformation and Storage Solution) buffer (PEG 8000 20% (w/v), DMSO 10% (w/v), $MgCl_2$ 100 mM, in LB). Briefly, bacterial cells were inoculated in LB medium overnight and diluted in LB in 1:100 ratio. The bacterial cells were grown until OD600 becomes 0.2-0.5, incubated on ice for 10 min and centrifuged at 3000 RPM, +4 ºC. LB-supernatant was removed, the bacterial cells were resuspended in 1:10 volume of TSS buffer

compared to morning growth and aliquoted into pre-chilled microcentrifuge tubes. Positive control was done by transformation of an existing plasmid, negative control was done by spreading cells into several LB agar plates containing different antibiotics (ampicillin, chloramphenicol, kanamycin). The aliquots were stored at -80 ºC for several months.

The competent cells were used for transformation of plasmids. First, the competent cell stock was thawed on ice for 10 minutes, intact plasmid, ligation or Gibson assembly reaction mix was added on competent cells, incubated on ice for 10 minutes. The cells were heated at 42ºC for 45 seconds for plasmid uptake via heat-shock, incubated on ice for 5 more minutes and diluted in 1 ml LB medium. Diluted cells were inoculated at 37 ºC for 30-60 minutes in shaking incubator. Cells were centrifuged at 13000 RCF for 1 minute, excess supernatant was removed, the cells resuspended in remaining medium and spread onto antibiotic containing LB-agar plate. The plate was incubated at 37 ºC overnight for single-colony growth.

3.2.2 Construction of plasmid maps and cloning

ALP is a phosphatase, which has a universal function, generating inorganic phosphate by breaking phosphate bonds in organic phosphorylated molecules. The corresponding gene, *phoA*, is a universal gene with conserved domains and function. (Galperin and Jedrzejas 2001) *E. coli* ALP works in the same manner with human ALP. (Halford, Schlesinger et al. 1972) Therefore, bacterial ALP is used in this study. *E. coli* ALP was amplified by the primers listed in Table B1. *E. coli* K12MG1655 genomic DNA was used as template. pET22b(+) vector was used for

cloning with modifications. Polyhistidine tag coding sequence was added the 5' of the multiple cloning site (MCS). 6 Histidine residues was expressed at the N-terminal of the protein after pelB periplasmic space localization signal peptide. Plasmid map was shown in Figure C1.

BamHI-HF (NEB R3101S) and XhoI (NEB R0146S) was used to cut the plasmid by restriction digestion. 5472 bp linear vector was generated after restriction enzyme digestion. Same restriction enzymes were used to cut amplified *phoA* gene PCR product. 1356 bp insert was generated upon restriction enzyme digestion. T4 ligase (NEB M0202S) was used to ligate the vector and insert. 1:3 insert to vector molar ratio was used and the mix incubated at room temperature for 10 minutes. The ligation mix was transformed into chemically competent *E. coli* DH5α bacteria. After overnight incubation, single colonies were selected and positive clones containing *phoA* gene were verified by Sanger sequencing. (Figure D1)

Codon optimization of human OCN and OPN coding sequences were performed for overexpression of the proteins in *E. coli* K-12 strain. Online IDT codon optimization tool was used to generate sequences. (http://eu.idtdna.com/CodonOpt) Briefly, native signal sequences of both genes were excluded and the coding sequences of pro-proteins were analyzed based on *E. coli* codon usage. Rare codons in *E. coli* was changed to more frequently used codons in order to increase expression levels. The resulting sequences, synthetic OCN and OPN genes, were synthesized by Genscript Company. Nucleic acid sequences of synthetic OCN and OPN genes, and amino acid sequences of recombinant OCN and OPN were shown in Table A1, E1.

Gibson assembly method was used to clone synthetic OCN gene into pGEX-6P1 vector. GST fusion protein was placed before MCS of the vector in order to enhance

expression of non-native proteins. Moreover, TEV protease cleavage site was inserted to the 5' of OCN nucleotide sequence via PCR extension. TEV protease provides cleavage of GST fusion protein after expression and/or purification. Also, 6X-His coding sequence was inserted at the 3' of OCN nucleotide sequence so as to detect expression and for purification. Primers which were used to amplify synthetic OCN gene were listed in Table B1. For cloning, restriction enzyme digestion was performed to cut pGEX-6P1 vector with BamHI-HF (NEB R3136S) and EcoRI-HF (NEB R3101S) , 4999 bp linear vector was formed and verified by agarose gel electrophoresis. Gibson assembly was performed by using equamolar ratio of insert and vector according to the protocol used elsewhere. (Gibson, Young et al. 2009) Briefly, vector and insert were mixed in equimolar ratio in the reaction mix containing exonuclease, polymerase and ligase. Exonuclease trims one of the strands in each DNA template, the resulting single stranded regions match and stick together since there is at least 20 bp overlapping homologous regions which were introduced to insert by extension PCR. Ligase closes the last gap between bases. Then, the assembly product was transformed into chemically competent *E. coli* DH5α bacteria. After overnight incubation, single colonies were selected and positive clones containing synthetic OCN gene (273 bp) was verified by Sanger sequencing. (Figure D2)

Standard ligation method was used to clone synthetic OPN gene into pET22b(+) vector, which contains 6x-His tag coding sequence before stop codon. The primers listed in Table B1 was used to amplify synthetic OPN gene via PCR. Restriction enzyme digestion was performed to cut pET22b(+) vector, and synthetic OPN gene product with NotI-HF (NEB R3189S) and XhoI (NEB R0146S). 5492 bp linear vector and 855 bp insert were formed, respectively and agarose gel electrophoresis

was performed to verify digestion. Ligation was performed at room temperature for 10 minutes and the ligation mix was transformed into chemically competent *E. coli* DH5α bacteria. After overnight incubation, single colonies selected and positive clones containing synthetic OPN gene (855 bp) was verified by Sanger sequencing. (Figure D3)

3.2.3 Sequence alignments

The plasmid maps were designed by Benchling online tool for the insertion of the codon optimized gene fragments. After cloning, selected positive colonies was sequenced by Genewiz Company. The sequencing results were analyzed by Geneious R9.0.5 software by pairwise alignment. The sequences of gene fragments in Benchling were used for comparison of identity. Automatically determine direction, Global alignment with free end gaps, 65% similarity options were chosen for alignment.

3.2.4 Expression of recombinant proteins in E. coli

E. coli BL21 (DE3) strain was used to express ALP, OCN and OPN proteins. The plasmids containing the synthetic genes of the proteins was isolated from DH5α bacteria and transformed into *E. coli* BL21 (DE3) strain via chemical transformation method described in 3.2.1. Expression of genes encoding ALP and OPN are controlled by T7 promoter and expression of gene encoding OCN is controlled by Tac promoter. Both promoters were switched on in the presence of a commonly used

inducer, Isopropyl β-D-1-thiogalactopyranoside (IPTG). Bacteria containing expression plasmids were inoculated overnight. Then, they were diluted at 1:50 ratio and inoculated for approximately 2 hours. 1 mM IPTG (Amresco 0487-10G), inducer of gene expression, was added when bacteria reaches OD=0.5-0.6, where they enter pre-log phase. In log phase, population density of the bacterial culture rapidly increases. Therefore, pre-log phase is the most suitable time for switching on inducible promoters. After several optimizations, induction of ALP was performed for 4 hours at 37 ºC, while induction of OCN and OPN were performed for 6-8 hours at 30 ºC. Following the induction of the proteins, bacterial culture centrifuged at 8000 RCF and the medium was discarded. Bacterial pellets were freezed at -80 ºC to keep the proteins intact until purification.

3.2.5 Purification of recombinant proteins

3.2.5.1 Cell Lysis

Bacterial pellet was obtained from 25 mL cell culture, the pellet was resuspended in 1 mL lysis buffer (50 mM $Na_2HPO_4.2H_2O$ (Merck 106342), 300 mM NaCl (Merck 1.06404-1KG), 10 mM Imidazole (VWR 0527-50G)), 1 mg/mL lysozyme (Sigma L6876-10G) and 1 mM phenylmethane sulfonyl fluoride (PMSF) (Amresco m145-5G). Cell lysis was provided by lysozyme and sonication. Sonication was made for 5 min on ice. Then, the cell lysate was centrifuged at maximum speed for 30-60

minutes to separate intact components from soluble proteins. The supernatant was filtered with 0.45 µm syringe filter (Isolab) before loading to mobile/immobile resin.

3.2.5.2 Purification of recombinant proteins by cobalt resin for small scale purification

Cobalt resin was used to trap his-tagged proteins and separate them from the rest of the proteins. Imidazole groups of histidines can bind to cobalt ions on resins. Thus, they can be purified from cell lysate. 200 µL cobalt resin (Thermo Scientific 89964-10 ML) was washed with 1 mL wash buffer (50 mM Na_2HPO_4, 300 mM NaCl, 10 mM Imidazole) to remove EtOH. Soluble proteins obtained from the previous step were mixed with cobalt resin and incubated at room temperature in an end-over-end rotator for 1 h. The resin was centrifuged at 700 RCF for 2 minutes to allow the resin to precipitate and washed with wash buffer 2-3 times with 1 ml of wash buffer in order to remove all non-specific proteins. Then, 100 µL elution buffer (50 mM Na_2HPO_4, 300 mM NaCl, 150 mM Imidazole) was mixed with the resin in an end-over-end rotator for 5 min and the resin was centrifuged at 700 RCF for 2 min. The supernatant contains eluted His-tag proteins since high imidazole concentration in elution buffer provides unbinding of His-tagged proteins from resin by replacing them. The elution was repeated for 5 times to elute all of the proteins bound to resin.

3.2.5.3 Purification of recombinant proteins by nickel column for large scale purification

Nickel column (HisTrap HP 1 ml, GE Healthcare) was used to purify large quantities of proteins. Nickel column was washed with 10 volumes of ddH_2O to remove EtOH. Then, the soluble part of the cell lysate were loaded to column in preparative high pressure liquid chromatography (Prep-HPLC, Agilent) device. Binding buffer (50 mM Na_2HPO_4, 300 mM NaCl, 20 mM Imidazole) was used for both binding and washing, and elution buffer (50 mM Na2HPO4, 300 mM NaCl, 500 mM Imidazole) was used for eluting proteins. The following reaction conditions were operated for purification: 35 min binding buffer for washing, 10 min elution buffer with 1 mL/min flow rate, 2 ml of elution aliquots was collected in fraction collector, 5 bar maximum pressure limit.

3.2.5.4 Removal of GST tag from OCN

GST was removed from OCN by TEV protease cleavage. Purified GST-OCN was concentrated to 1 ml with a 10 kDa cutoff filter unit (Thermo) and loaded into desalting column (Desalt 5 ml, GE Healthcare). Desalting column was washed with 10 ml ddH_2O and was equilibrated with 5 ml 25 mM Tris Buffer prior to loading of the proteins. Then, the proteins were eluted in 2 ml 25 mM Tris Buffer. Concentration of GST-OCN was determined by BCA assay and GST-OCN (2 ml) was mixed with TEV protease (1:100 ratio of TEV:GST-OCN). For efficient

cleavage by TEV protease, 100 µl of 20X TEV Reaction Buffer (1 M Tris-HCl (Sigma T5941-500G) (pH 8.0), 10 mM EDTA (Sigma E5134-500G)), and 20 µl of 0.1 M DTT (Invitrogen P2NY00147) were added into the reaction. Almost 90% of the protein was cleaved at room temperature when incubated for 16 h, which was detected by SDS-PAGE analysis.

After verification of efficient cleavage, the reaction mixture was concentrated to 1 ml with a 3 kDa cutoff filter unit (Millipore) and loaded to a desalting column. Desalting column was washed with 10 ml ddH_2O and was equilibrated with 5 ml 20 mM binding buffer prior to loading proteins. Then, the proteins were eluted in 2 ml 20 mM binding buffer. Then, binding to cobalt resin explained in section 3.2.5.2 was repeated. Thus, GST-OCN-His (Uncut protein), GST-TEV-His, OCN-His was bound and eluted with cobalt resin while GST remained in unbound fragment. The elution was concentrated to 1 ml with a 3 kDa cutoff filter unit, and loaded to a desalting column. The desalting column was washed with 10 ml ddH_2O, and was equilibrated with 5 ml 1X PBS (prepared from 10X PBS stock containing 1.37 M NaCl, 26.8 mM KCl (Merck 1.04936-1KG), 0.1 M Na_2HPO_4, 17.6 mM K_2HPO_4 (Merck 1.05104-1KG), pH=7.4 by dilution with ddH_2O) prior to loading the proteins. Then, the proteins were eluted in 2 ml 1X PBS.

GST Bind Resin (Novagen 70-541-3-10ML) was used to separate GST-TEV-His, and GST-OCN-His from OCN-His. 1 mL of the GST resin was washed twice with 2.5 mL 1X PBS to remove EtOH. The proteins obtained from the previous step were added onto the GST Bind Resin. Binding of the GST-tagged proteins to GST-Bind Resin was performed at room temperature for 1 h in an end-over-end rotator. Then, the resin was centrifuged at 500 RCF for 5 min. The unbound fragment and first 2

washes contain almost pure OCN-His and were collected. GST-tagged proteins were eluted at least twice in 250 µL GST Elution Buffer (50 mM Tris-HCl, 10 mM L-Glutathione, reduced (Cayman Chemical 10077461-10G), pH=8.0).

The unbound proteins were concentrated to 1 ml with a 3 kDa cutoff filter unit, and loaded to a desalting column. Desalting column was washed with 10 ml ddH_2O and was equilibrated with 5 ml 25 mM Tris or OCN storage buffer (0.121% Tris, 50% Glycerol, 0.435% Sodium chloride). Then, the proteins were eluted in 2 ml 25 mM Tris or OCN Storage Buffer for either immediate use or -20/-80 ºC storage, respectively.

3.2.6 Verification of expression and purification

3.2.6.1 SDS-PAGE and Coomassie Blue Staining

2.2 ml ddH_2O, 2.6 ml 1.5 M Tris-HCl (Sigma) (pH 8.8), 100 µl 10% (w/v) SDS, 5 ml Acrylamide/Bisacrylamide (VWR) (30%/0.8% w/v), 100 µl 10% (w/v) APS (Biorad Ammonium persulfate), 10 µl tetramethylethylenediamine (TEMED) (Biorad) were used to prepare 15% SDS resolving gel. 3.2 ml ddH_2O, 2.6 ml 1.5 M Tris-HCl (pH 8.8), 100 µl 10% (w/v) SDS, 4 ml Acrylamide/Bisacrylamide (30%/0.8% w/v), 100 µl 10% (w/v) APS, 10 µl TEMED were used to prepare 12% SDS resolving gel. 2.975 ml ddH_2O, 1.25 ml 0.5 M Tris-HCl (pH 6.8), 50 µl 10% (w/v) SDS, 0.67 ml Acrylamide/Bisacrylamide (30%/0.8% w/v), 50 µl 10% (w/v) APS, 5 µl TEMED were used for preparing the stacking gel. Resolving gel was allowed to dry for 30

min at room temperature after addition of 250 µl isopropanol. Stacking gel was added after complete removal of isopropanol, the combs were placed immediately, and the gel was allowed to dry for 30 min at room temperature before use.

4 µl 6X Laemmli sample buffer (1.2 g SDS (sodium dodecyl sulfate), 6 mg bromophenol blue, 4.7 ml glycerol, 1.2 ml Tris (0.5M, pH 6.8), 2.1 ml ddH_2O), and 20 µl protein were mixed prior to loading SDS gel. Cell lysates were denatured at 95 ºC for 5 min. 12% SDS gel was used to detect proteins higher than 15 kD (ALP and GST-OCN and OPN) and 15% SDS gel was used to separate proteins as low as 10 kD (OCN).

SDS-PAGE was performed at 120-190 V for 45-90 minutes for an efficient protein separation. For detecting whole proteins, the gels were stained with Coomassie Brilliant Blue (CBB) Solution (45 MetOH%, 10% glacial acetic acid, 3 g/L CBB R250 (Sigma 27815-25G)), and destained in destaining buffer (10% acetic acid, 30% methanol). For detecting his-tagged proteins, the proteins on gel were transferred to a PVDF (Thermo Scientific 88520) membrane.

3.2.6.2 Western blotting

The proteins were transferred to a PVDF membrane in a Transblot Turbo Transfer System (Biorad). Transfer conditions were as following for ALP, GST-OCN and OPN: 25 kV, 1.3 A for 7 min. Transfer conditions for OCN were as following: 25 kV, 1.3 A for 5 min. The membrane was incubated in blocking solution (3% milk powder in 1X TBS-T) for 1 h in a rotator at room temperature. Immediately after

blocking, the membrane was transferred to the primary antibody solution (1: 10000 dilution of mouse anti-6X-His Tag mAb (HIS.H8) (PTGLAB 66005-1-1G-0.15 ML) in 5% milk powder in 1X TBS-T). Primary antibody was allowed to bind His-tagged proteins on membrane for 1 h at room temperature or for overnight at +4 ˚C in a rotator. Prior to and after incubation in secondary antibody solution (1: 10000 dilution of Goat anti-mouse IgG H&L (HRP) (Abcam ab6789-1 MG) in 5% milk powder in 1X TBS-T), the membrane was washed 3 times in 1X TBS-T for 5, 15, 5 min in a rotator at room temperature. Secondary antibody binding was performed at room temperature for 1 h in a rotator. ECL Substrate (Biorad 170-5060-200 ML) was used to detect the secondary antibody. Briefly, the membrane was incubated in 1 ml of substrate solution in dark without agitation and imaged immediately in ChemiDoc MP Imaging System (Biorad).

3.2.7 Protein quantitation

Serial dilutions of BSA (2 mg/mL, Pierce 23209) were prepared and used to form a standard curve. Equal amount of BSA standard curve samples and protein of interest were placed in 96-well plates in triplicate. BCA Protein Assay Kit (Pierce 23225) was used to measure protein concentrations. Reagent A and Reagent B was mixed in 50:1 ratio prior to measurement and 200-260 µl of mix was added on proteins by a multichannel pipette. The plate was incubated at 37 ºC for 30 min, and was read in SpectraMax M5 spectrophotometer (Molecular Devices) at 562 nm absorbance. Protein concentrations were automatically calculated by the standard BCA assay protocol in SoftmaxPro software.

3.2.8 Analysis of enzyme kinetics

3.2.8.1 Determination of unit enzyme concentration

ALP in 25 mM Tris (pH 7.4) was diluted, and 7 serial dilutions were prepared. 0.5 mM pNPP and ALP were incubated at 37 ºC for 5 min. ALP and pNPP (Sigma 20-106 EMD MILLIPORE) were mixed in 1:1 ratio, and each reaction was prepared in triplicate. Absorbance measurement was performed in a spectrophotometer at 405 nm. pNP (Fluka 35836) was used to prepare standard curve. 140 µM pNP was used as the starting substrate for serial dilutions. 7 serial dilutions was prepared. Absorbance measurement was performed at 405 nm at spectrophotometer. ALP converted pNPP into pNP, and pNP concentration was calculated based on the standard curve. (Figure F1) Then, the reaction velocity (pNP/min) was calculated. The concentration of ALP which generates 1 µM pNP in 1 min was determined as 1 U enzyme. (Figure F2)

3.2.8.2 ALP enzymatic activity in the presence of OCN and OPN

4 mM pNPP substrate was prepared in pNPP reaction buffer (0.1 M Lysine (Amresco 0167-1 KG), 1 mM $MgCl_2$ (Sigma M4880-100 G), 1 mM $ZnCl_2$ (NEB 7646-85-7)). 5 serial dilutions of pNPP were performed in the pNPP reaction buffer. 1 U ALP (25 mM Tris, pH=7.4) was used for each reaction in the presence of OCN, OPN, both or none. Each reaction was performed in triplicate at 37 ºC for 10 min.

Absorbance measurement was performed at 405 nm at spectrophotometer. pNP standard curve which was prepared previously was used to calculate pNP concentration and reaction velocity (µM pNP/min). Michaelis-Menten graphics were generated at Graphpad Prism 6 software. Then, reaction rate constant, k_m (µM), and maximum velocity, v_{max} (µM/min), values were calculated. Nonlinear regression curve fitting was performed to fit experimental data with the maximum number of iterations (95% confidence interval, R2>0.9 for each group). Second order polynomial smoothing and 4 number of neighbors averaging were applied on the curves of Michaelis-Menten graphs. Statistical significance of k_m and v_{max} values were calculated by TWO-WAY ANOVA in Graphpad Prism 6 software.

3.2.9 Secondary structure analysis by circular dichroism (CD) measurement

CD Spectra Measurement Device (Jasco J-815) was used to analyze the secondary structures of OCN and OPN. In addition, the effects of calcium and phosphate on the secondary structure of the recombinant proteins were analyzed. A temperature gradient was selected between 22 and 37 ºC with 5ºC intervals, 300 sec delay time, 1 mm band width. OCN and OPN proteins were prepared in 25 mM Tris, pH=7.4. 1 M $CaCl_2$ (Merck 1.02378-500 G), 1 M Na_2HPO_4, or 1 M β-GP (Calbiochem 35675-100 G) was used to analyze the interaction of the proteins with calcium, organic and inorganic phosphate. 5 mM $CaCl_2$, Na_2HPO_4 and β-GP was used in the analysis.

3.2.10 Biomineralization of calcium and phosphate in the presence of recombinant proteins

CaP crystal formation in the presence of ALP, organic phosphate source (β-GP), and calcium was studied. The effect of the most abundant bone mineralizing extracellular matrix proteins, namely OCN and OPN, on CaP crystal formation was analyzed. To do this, a biomineralization buffer (BB) was prepared based on the protocol described elsewhere. (Gungormus, Fong et al. 2008) The BB was prepared as 2X (48 mM CaCl2, 28.8 mM β-Glycerophosphate, 25 mM Tris-HCl pH 7.4) and used 100 µl for each 200 µl reaction. 200 µl reaction was composed of 1X BB, 1 mM $MgCl_2$, 5 U ALP, and varying concentrations of OCN and OPN.

3.2.10.1 Spectrophotometry measurements

The reaction was performed in 96 well plate for spectrophotometry measurements in SpectraMax Microplate Reader. A light scattering measurement at 820 nm absorbance was performed for 1 h with 1 min intervals at 37 ºC so as to detect initial CaP crystal formation. All reactions were performed in triplicate for statistical analysis. After about 20 min, the reaction becomes observable. The slope of the first 30-40 min of CaP formation reaction was calculated (R^2>=0.98), and designated as observable reaction rate constant ($k_{observable}$).

3.2.10.2 Imaging of CaP crystals by electron microscopy

The plate was incubated at 37 ºC for up to 24 h to prepare samples for scanning electron microscopy (SEM) imaging and energy-dispersive X-ray spectroscopy (EDS) analysis. Briefly, silicon wafer was cut into small pieces and washed with isopropanol prior to sample preparation. 5 µL of sample from 200 µl CaP formation reaction was dropped onto a wafer, and incubated for 10 min at room temperature. The wafer was dried with a lint-free napkin carefully and washed twice with 1 µL ddH_2O for 1 min each. The wafer was kept in a vacuum desicator till SEM imaging. Before imaging, the wafer surface was coated with 5 nm Au/Pd. The images were taken by E-SEM microscope (FEI-Quanta 200 FEG). A representative image was shown in the figures for all groups. Crystal sizes were measured from SEM images by ImageJ Software. Statistical analysis of crystal size was done by Graphpad Prism 6 Software by unpaired t-test. The number of size measurements, the mean size, and standard error mean (SEM) values were indicated in both results section and in figure captions. EDS analysis was performed with EDAX Genesis software attached to the SEM microscope. Same operating conditions were used for all measurements (Accelerating voltage: 5 kV, Spot size 3.0).

3.2.10.3 Quantitative analysis of Ca/P ratio and determination of crystallinity by X-ray photoelectron spectroscopy (XPS) analysis

CaP crystal formation reaction was transferred to a low-binding microcentrifuge tube after incubation at 37 ºC for 24 h. The sample was centrifuged at 8000 RCF for 8 min and supernatant was removed. 100 µL of pH 10 water (10% NH_4OH) was added onto the tube to stop reaction, and the tube was centrifuged at 8000 RCF for 8 min. Supernatant was removed, and the sample was washed with 100 µL EtOH. The sample was centrifuged at 8000 RCF for 8 min, supernatant was removed, and the sample powder was air dried for at least 3-5 min. The sample was kept at room temperature until analysis. The elemental composition of sample was analyzed by XPS (Thermo Scientific K-Alpha spectrometer). The binding energy (BE) scale was adjusted based on the measurement of adventitious C (284.6 eV). The survey scan was acquired with scan number 2 and the high resolution detailed scans of Ca(2p), P(2p), O(1s) and C(1s) were acquired with scan number 10-30 based on the intensity of the signal. 400 µm spot size was chosen for each point and all samples were scanned from 3 different points. Adjusted Ca/P ratio was calculated based on the protocol described in a previous research in the literature (Lu, Campbell et al. 2000). Statistical analysis of Ca/P ratio was done by Graphpad Prism 6 Software by unpaired t-test for comparing two samples, and by One-Way ANOVA for comparing more than two samples.

3.3 Results and Discussion

3.3.1 Cloning, expression and purification

3.3.1.1 Cloning of proteins into prokaryotic expression vectors

ALP is an enzyme which converts organic phosphate into inorganic phosphate. CaP mineral formation in bone cannot start before the formation of inorganic phosphate, so, expression of ALP is the most fundamental requirement of the bone mineral formation. The enzyme transfers phosphate group to Ser102 position of itself in transition state, and generates inorganic phosphate by removing phosphate group at this position. (Zhang, Yang et al. 2018) The bacterial ALP has a structural homology with human ALP, and it has the same function. (Figure 3) (Herries 1981). Therefore, the *phoA* gene-coding for the bacterial ALP was amplified from the genomic DNA of the *E. coli* K-12 strain (Figure 4) with the primers listed in Table B1, and cloned into the pET22b(+) plasmid. (Figure C1)

```
[Escherichia      ALRDSLSDKPAKNIILLIGDGMGDSEITAARNYAEGAGGFFKGIDALPLTGQYTHYALNK
[Homo             LELQKLNTNVAKNVIMFLGDGMGVSTVTAARILKGQ-LHHNPGEETRLEMDKFPFVALSK
[Mus              LKLQKLNTNVAKNVIMFLGDGMGVSTVTAARILKGQ-LHHNTGEETRLEMDKFPFVALSK
[Gallus           LRLQHLNQNVAKNLILFLGDGMGVSTVTAARILKGQ-LQHRKGEESLLEMDKFPYVALAK
                     : *. : ***:*:::***** * :****        .  * ::     :: . ** *

[Escherichia      KTGKPDYVTDSAASATAWSTGVKTYNGALGVDIHE----------KDHPTILEMAKAAGL
[Homo             TYNTNAQVPDSAGTATAYLCGVKANEGTVGVSAATERSRCNTTQGNEVTSILRWAKDAGK
[Mus              TYNTNAQVPDSAGTATAYLCGVKANEGTVGVSAATERTRCNTTQGNEVTSILRWAKDAGK
[Gallus           TYNTNAQVPDSAGTATAYLCGVKANEGTVGVSAGVTRDRCNTTKGQEVTSILRWAKDEGK
                  .  .   * ***.:***:  ***: :*::**.            ::  :**. **  *

[Escherichia      ATGNVSTAELQDATPAALVAHVTSRKCYGPSATSEKCPGNALEKGGKGSITEQLLNAR--
[Homo             SVGIVTTTRVNHATPSAAYAHSADRDWYSDNE----MPPEALSQGCKD-IAYQLMHNIRD
[Mus              SVGIVTTTRVNHATPSAAYAHSADRDWYSDNE----MPPEALSQGCKD-IAYQLMHNIKD
[Gallus           AVGIVTTTRVTHATPSAAYAHSANRDWYSDGE----MPLDALEGGCKD-IARQLVDNIPD
                  :.* *:*:.: .***:*  ** :.*. *.        * :**. * *  *: **:.
```

Figure 3. ALP is a conserved enzyme and functions similarly in several organisms. Multiple sequence alignment of ALP proteins from 4 selected organisms is performed by Clustal Omega and is partially shown.

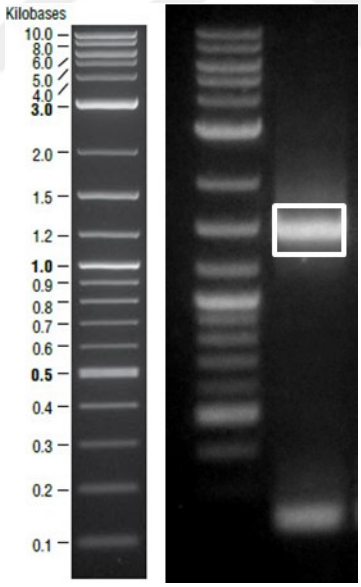

Figure 4. Amplification of phoA gene from bacterial genomic DNA. DH5α genomic DNA was used as a template to amplify *phoA* gene. PCR reaction was performed according to the protocol of Q5 Polymerase (NEB). 2-log DNA ladder (NEB) was used for detection.

Commercial plasmid contains 6X His-tag sequence at the 3' end of the MCS, at the C-terminal of the protein. Protein purification and western blot analysis of bacterial ALP with C terminal his-tag using anti-his tag antibody were not successful. (data not shown) Consequently, the his-tag sequence was moved to the N-terminal of the ALP, downstream of the periplasmic translocation signal pelB. Since pelB can localize ALP to periplasmic space, the native periplasmic space localization signal of ALP was removed. A GS linker was added between ALP and His-tag sequence in order to provide flexibility to His-tag. (Figure 5, C1)

Figure 5. Schematic diagram of ALP expression cassette. Native periplasmic space localization sequence was replaced with pelB periplasmic space localization peptide. His-tag was added after pelB to the N-terminal of the protein for detection of expression and purification. GS linker provide flexibility to His-tag. T7 promoter and terminator were used for expression by T7 polymerase.

Synthesis of human proteins in bacterial platforms is widely used since bacterial cells are easy to grow. However, codon bias, the difference in the tRNA abundance among organisms, may cause the reduction in protein yield or even loss of protein expression. (Plotkin and Kudla 2010) Therefore, codon optimization is necessary in order to produce recombinant proteins in distant organisms. Synthetic human OCN gene fragment was synthesized by Genscript Company (Table A1) in order to prevent codon bias. Synthetic OCN gene was amplified by PCR (Figure 6), and cloned into the pET22b(+) plasmid (data not shown), which contains 6x-His tag at the 3' end of MCS.

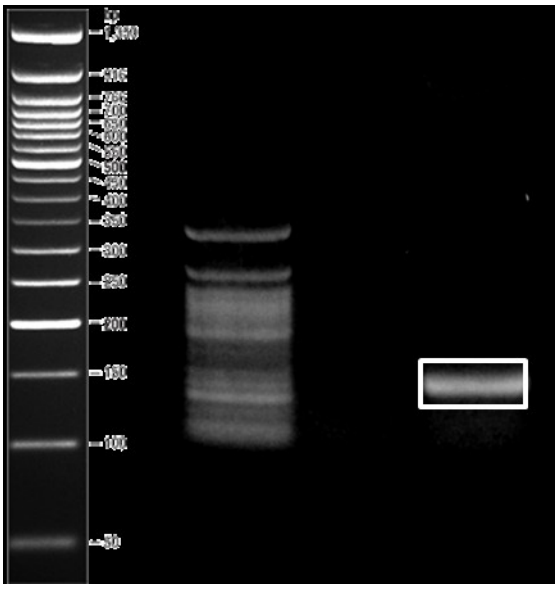

Figure 6. OCN gene was amplified by PCR. Synthetic OCN gene fragment was used as template in PCR. PCR reaction was performed according to the protocol of Q5 Polymerase (NEB). 50 bp ladder (NEB) was used for detection.

OCN is a ~10-kDa small soluble protein, and it could not be detected in Western blot using 6x-his antibody (data not shown). Therefore, it was cloned into another vector, pGEX-6P1 (Figure C2), which contains the glutathione S-transferase (GST) gene prior to MCS. GST is a highly soluble and easily producible protein, and it is generally used to improve the efficiency of recombinant protein production and solubility of the protein. (Käkönen, Hellman et al. 1996) A TEV protease recognition site was added between GST and OCN to cleave the GST-tag after purification. A 6X his-tag was added to the C-terminal of the protein for IMAC purification. (Figure 7)

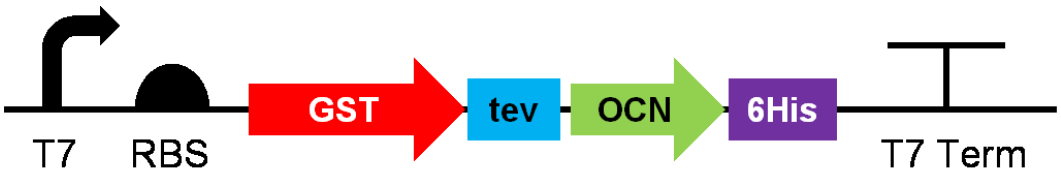

Figure 7. Schematic diagram of OCN expression cassette. GST tag added to the N-terminal of the protein for enhancing solubility, expression and purification. TEV recognition site was inserted between GST and OCN for removing GST after expression. His-tag was added to the C-terminal of the protein for detection of expression and purification. T7 promoter and terminator were used for expression by T7 polymerase.

Compared to OCN, OPN is a large ~33 kDa soluble protein, and it can be produced in bacteria recombinantly without any solubility-enhancing tag. Synthetic OPN gene fragment was synthesized, amplified by PCR (Figure 8), and cloned into the pET22b(+) plasmid. (Figure C3) A 6X his-tag was placed at the 3' end of the MCS of commercial plasmid, and it was therefore added to the C-terminal of protein. (Figure 9)

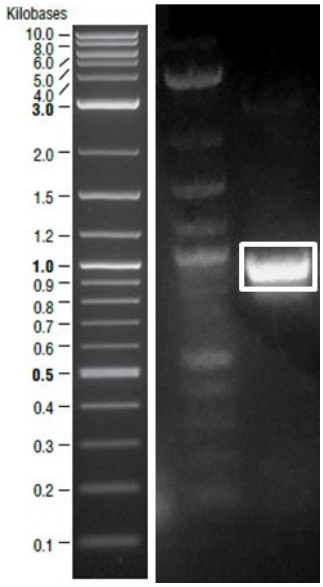

Figure 8. OPN gene was amplified by PCR. Synthetic OPN gene fragment was used as template in PCR. PCR reaction was performed according to the protocol of Q5 Polymerase (NEB). 2-log DNA ladder (NEB) was used for detection.

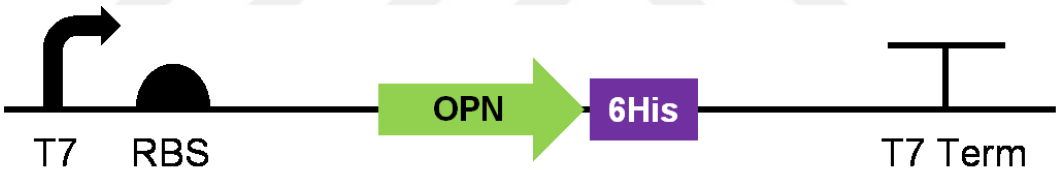

Figure 9. Schematic diagram of OPN expression cassette. His-tag was added to the C-terminal of the protein for detection of expression and purification. T7 promoter and terminator were used for expression by T7 polymerase.

3.3.1.2 Verification of cloning

Restriction enzyme digestion, colony PCR and Sanger sequencing were performed for verification of all cloning experiments. For restriction enzyme digestion of pEt22b-ALP, HindIII-HF enzyme was used to cut candidate pEt22b-ALP constructs. 6500 bp expected band was observed for the last candidate. (Figure 10) This plasmid

was sent sequencing (Genewiz Company). Sequencing result was aligned with phoA gene sequence at Geneious software. (Figure D1) Although sequence identity is 81%, the proceeding experiments was performed with this plasmid since the first 1000 bp matches 100%. The reduction in identity was due to the loss of effective reading after 1000 bp during sequencing.

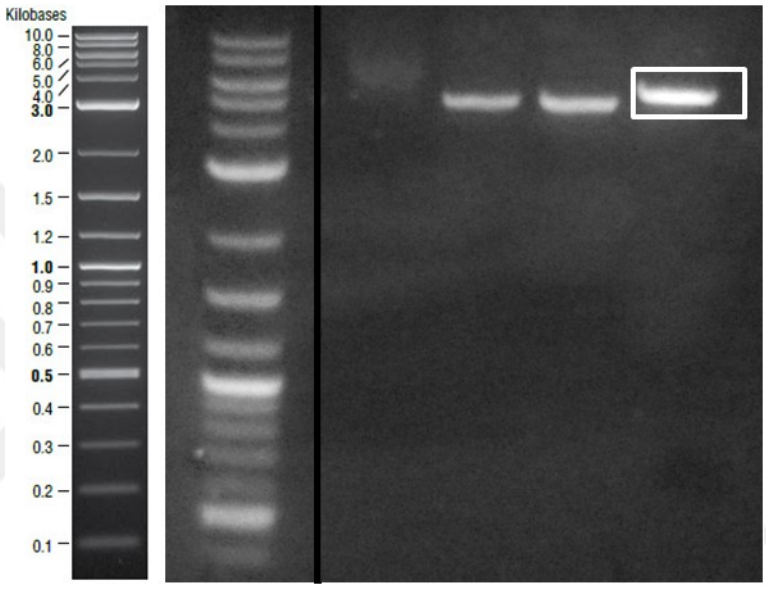

Figure 10. Agarose gel electrophoresis image of pEt22b-ALP plasmid verification by restriction enzyme digestion. Uncut plasmid was used as digestion control (Lane 2). 3 colonies was selected to verify insertion of ALP into pEt22b by HindIII digestion (Lanes 3-5). Last plasmid in image has a higher band (6500 bp vs. 5000 bp), which verifies insertion. The ladder was 2-log DNA ladder (NEB) in Lane 1.

For restriction enzyme digestion of pGEX-6P1-OCN, EcoRI-HF and BamHI enzymes were used to cut candidate pGEX-6P1-OCN constructs. 300-400 bp expected band was observed for the last candidate. (Figure 11) This plasmid was sent to sequencing (Genewiz Company). Sequencing results was aligned with OCN

gene sequence at Geneious software (Figure D2) OCN gene fragment sequence aligns with the sequencing results completely.

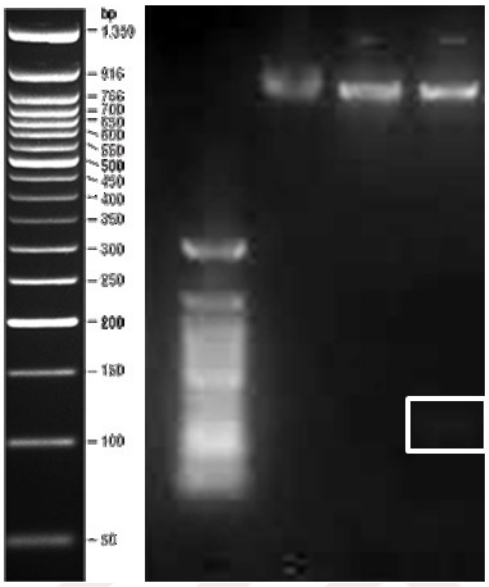

Figure 11. Agarose gel electrophoresis image of pGEX-6P1-OCN plasmid verification by restriction enzyme digestion. Uncut plasmid was used as digestion control (Lane 2). 2 colonies was selected to verify insertion of OCN into pGEX-6P1 by BamHI and EcoRI digestion (Lanes 3-4). Last plasmid in image has a band (300-400 bp), which verifies insertion. The ladder was 2-log DNA ladder (NEB) in Lane 1.

For restriction enzyme digestion of pEt22b-OPN, EcoRI-HF and BamHI enzymes were used to cut candidate pEt22b-OPN constructs. 900 bp expected band was observed for one of the candidate. (Figure 12) This plasmid was sent to sequencing (Genewiz Company). Sequencing results was aligned with OPN gene sequence at Geneious software. (Figure D3) OPN gene fragment sequence aligns with the sequencing results completely.

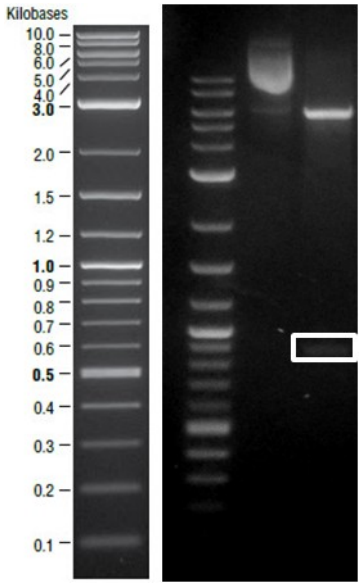

Figure 12. Agarose gel electrophoresis image of pEt22b-OPN plasmid verification by restriction enzyme digestion. Uncut plasmid was used as digestion control (Lane 2). One of the colonies was selected to verify insertion of OPN into pEt22b by NotI and XhoI digestion (Lane 3). Last plasmid in image has a band (900 bp), which verifies insertion. The ladder was 2-log DNA ladder (NEB) in Lane 1.

3.3.1.3 Overexpression of native and recombinant proteins in E. coli

The expression of ALP was induced by IPTG in BL21 strain, and ALP was extracted by standard lysis protocol to obtain both cytoplasmic and periplasmic fractions. Prior to purification, the overexpression of ALP was detected in cloned bacteria after a 4-h induction with 1 mM IPTG by pNPP phosphatase assay. The bacteria containing no plasmid was used as negative control. (Figure 13)

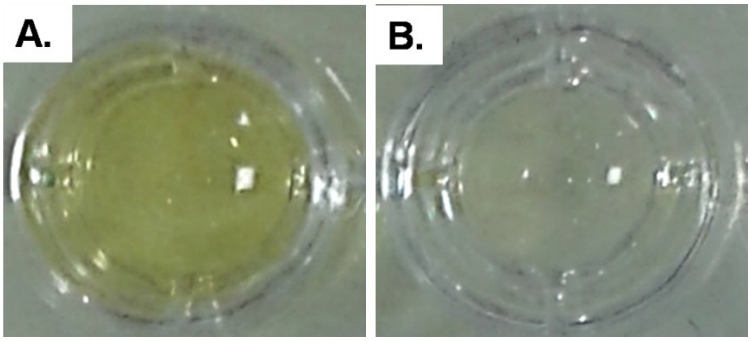

Figure 13. Phosphatase assay detects overexpression of ALP in transformed cells.

Overexpression of ALP in periplasmic extract of pET22b-ALP bacteria (A) compared to that of control bacteria (B) after 4 hour IPTG (1 mM) induction at 200 RPM, 37 ºC.

The expression of OCN and OPN was induced by IPTG in BL21 strain, and proteins were extracted by standard lysis protocol (Figure 16,18)

3.3.1.4 Purification of recombinant proteins by affinity chromatography and verification by Western Blotting

ALP was purified by Immobilized metal affinity chromatography (IMAC). Two fragments that have approximately 50 kDa molecular weights were detected both in SDS-PAGE followed by Coomassie blue staining and in Western blotting using antibodies against polyhistidine tag. (Figure 14, 15) The smaller fragment might correspond to the periplasmic space-localized ALP, and the larger one could correspond to the cytoplasmic fraction since 22 amino acid long pelB signal fragment is cleaved after localization. (Singh, Sharma et al. 2013)

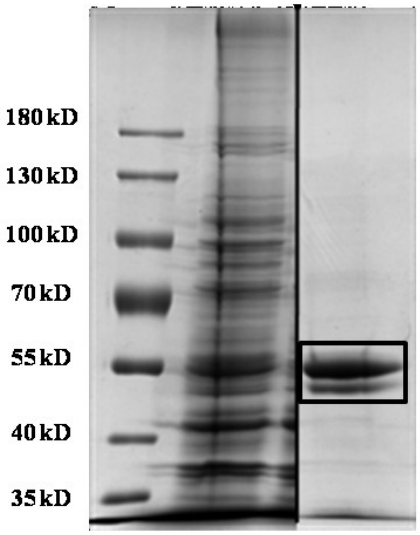

Figure 14. Purification of ALP by IMAC detected by SDS-PAGE analysis. Lane 1 Page Ruler (NEB) ladder, Lane 2 cell lysate, Lane 3 purified ALP. Purification was done by either Cobalt resin or Ni-NTA resin.

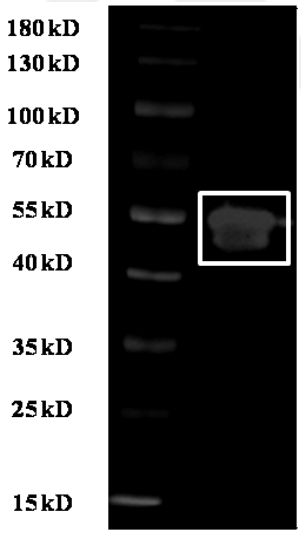

Figure 15. Purification of ALP by IMAC detected by Western blot analysis. Lane 1 Page Ruler (NEB) ladder, Lane 2 purified ALP. Detection was done by anti-his-tag primary antibody, HRP-conjugated secondary antibody and ECL substrate.

For purification of GST-OCN fusion protein, immobilized metal affinity chromatography (IMAC) method was used (Figure 16) Then, the GST-OCN fusion

protein was cleaved with TEV protease, and GST was removed with the GST binding resin. (Figure 16) The purification was detected by SDS-PAGE and Western blot analysis. (Figure 16, 17)

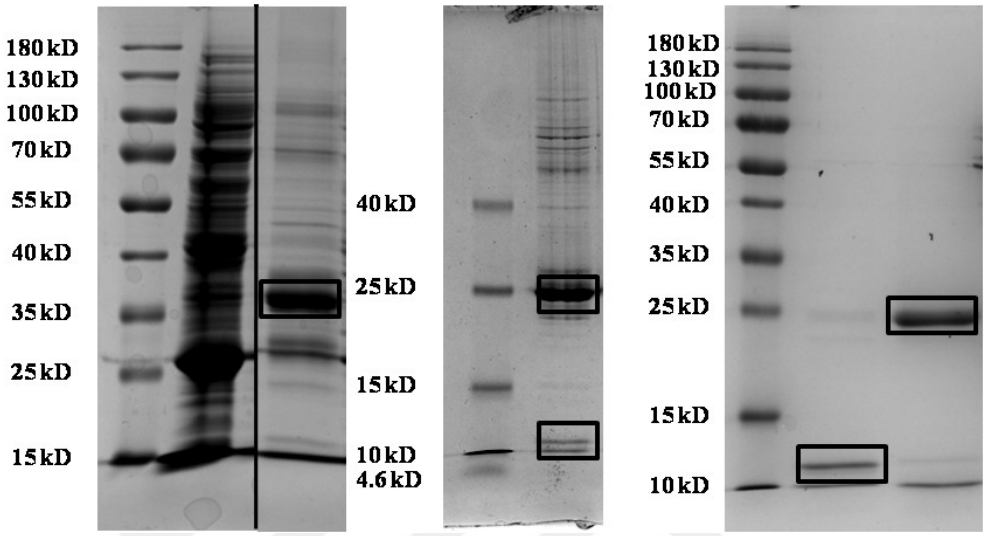

Figure 16. Purification of OCN detected by SDS-PAGE. Image 1: Lane 1 Page Ruler (NEB) ladder, Lane 2 cell lysate, Lane 3 purified GST-OCN (36 kD). Purification was done by either Cobalt resin or Ni-NTA resin. **Image 2:** Lane 1 Spectra Low Range (NEB) ladder, Lane 2 GST (26 kD) and OCN (10 kD) were cut by TEV protease. **Image 3:** Lane 1 Page Ruler (NEB) ladder, Lane 2 OCN (10 kD), Lane 3 GST (26 kD). Purification was done by GST bind resin.

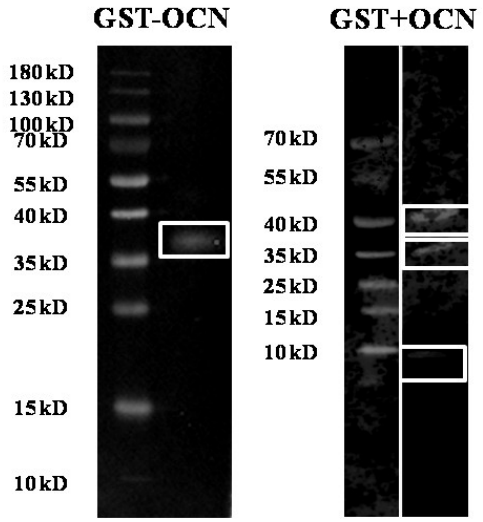

Figure 17. Purification of OCN by IMAC detected by Western blot analysis. Image 1: Lane 1 Page Ruler (NEB) ladder, Lane 2 purified GST-OCN (36 kD). **Image 2:** Lane 1 Spectra Low Range (NEB) ladder, Lane 2 GST-OCN (36 kD), GST (26 kD) and OCN (10 kD). GST-OCN were cut by TEV protease. Detection was done by anti-his-tag primary antibody, HRP-conjugated secondary antibody and ECL substrate.

OPN was expressed in the *E. coli* BL21 (DE3) strain using IPTG induction. Following IMAC purification, a clear band around 50 kDa was observed after SDS-PAGE Coomassie blue staining and Western blot analysis using antibodies against 6X-His tag. (Figure 18, 19) Because OPN is a negatively charged protein, it was observed at a higher molecular weight than expected (~33 kDa). Detection of OPN as an approximately 50 kDa fragment is consistent with the literature. (Denhardt and Guo 1993)

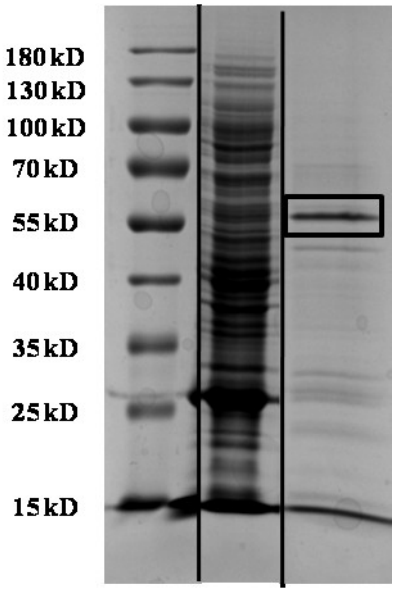

Figure 18. Purification of OPN by IMAC detected by SDS-PAGE analysis. Lane 1 Page Ruler (NEB) ladder, Lane 2 cell lysate, Lane 3 purified OPN. Purification was done by either Cobalt resin or Ni-NTA resin.

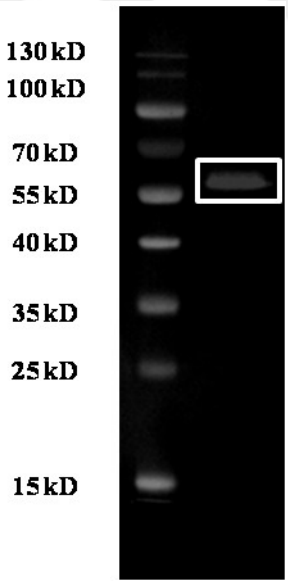

Figure 19. Purification of OPN by IMAC detected by Western blot analysis. Lane 1 Page Ruler (NEB) ladder, Lane 2 purified OPN. Detection was done by anti-his-tag primary antibody, HRP-conjugated secondary antibody and ECL substrate.

3.3.2 Effect of recombinant proteins on enzyme kinetics

The Michaelis-Menten kinetics relates reaction velocity of the enzyme to substrate concentration. In order to apply the Michaelis-Menten kinetics to a reaction, Substrate (S) should bind reversibly to the Enzyme (E), form an enzyme-substrate (ES) complex, and generate the free enzyme E and product P. V_{max} represents the maximum velocity achieved by the system, at maximum (saturating) substrate concentrations. K_M (the Michaelis constant) is the substrate concentration at which the reaction velocity is 50% of the V_{max}. (Johnson and Goody 2011)

In this study, the effect of OCN and OPN proteins on the enzyme activity of ALP was studied by commonly used phosphatase assay. In this assay ALP converts organic phosphate (pNPP) into inorganic phosphate (pNP), which results a yellow color. The intensity of this color correlates with the enzymatic activity and is detected by absorbance measurement at 405 nm in spectrophotometer. I performed Michaelis-Menten kinetic analysis in the presence of OCN and OPN to understand if these proteins affect ALP activity or not. According to the results of kinetic analysis, v_{max} did not altered, but k_m increased when OCN and OPN was added to the reaction. (Figure 20) Since v_{max} did not change, I concluded that ALP enzymatic activity was not affected by the presence of OCN and OPN. ALP still conserves its secondary structure and exerts its activity on phosphate conversion. The increase in k_m indicates that OCN and OPN bind to organic phosphate and reduce the chance of ALP to interact with this molecule. In other words, a higher concentration of substrate was required to reach the enzyme to half-maximum velocity.

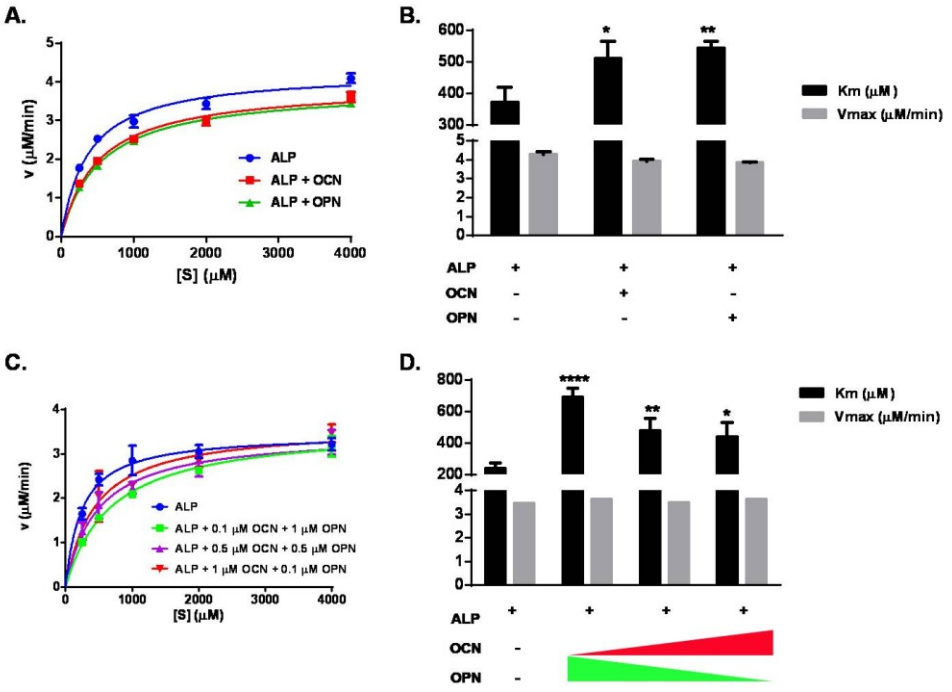

Figure 20. Michaelis-Menten kinetic analysis of ALP activity in the presence of OCN and OPN. A. ALP activity in the presence of OCN or OPN. B. V_{max} and K_m of ALP in the presence of OCN or OPN. K_m (µM), the reaction rate constant, increased in the presence of OCN and OPN. C. ALP activity in the presence of varying concentrations of OCN and OPN. D. v_{max} and k_m of ALP in the presence of OCN and OPN. K_m, the reaction rate constant, increased in the presence of varying concentrations of OCN and OPN. V_{max} (µM pNP/min) is constant for all cases. Experiment was performed in triplicate. Nonlinear regression curve fitting was performed to fit experimental data on Michaelis-Menten curve (A-C). TWO-WAY ANOVA was performed to compare each group with ALP only group (B-D). V_{max} was not statistically significant while k_m significantly increased for all groups.

In the presence of 1 U ALP and 0.5 µM OCN or OPN, k_m increased 1.4- and 1.5-fold, respectively. (Figure 20) The data suggest that OCN and OPN bind to organophosphate, decreasing its probability of interaction with ALP. Moreover, OPN was more effective in competitive inhibition of ALP than OCN. In the presence of 1

U ALP and varying concentrations of OCN and OPN, the same effect can be observed. (Figure 20) In the presence of 1 µM OCN and 0.1 µM OPN, k_m increased 1.8-fold. When the OCN concentration was decreased to 0.5 µM and the OPN concentration was increased to 0.5 µM, k_m increased 2-fold. When the OCN concentration was further decreased to 0.1 µM and the OPN concentration was increased to 1 µM, k_m increased more dramatically (2.9-fold) supporting the idea of OPN being more effective in the competitive binding to organophosphate.

In summary, v_{max} was not altered, suggesting that ALP conformation and the binding of organophosphate to the active site of ALP were not affected by the presence of OCN and OPN.

3.3.3 Secondary structure analysis

CD measures the emission of UV light from the proteins and each structural element (α helix, β-sheet, turns, random coils) in a protein gives a characteristic excitation in spectrum. Therefore, secondary structure of proteins can be determined by CD easily. (Micsonai, Wien et al. 2015)

In order to observe the structural elements in OCN and OPN, I performed CD analysis. In addition, I added calcium, organic and inorganic phosphate on each protein in order to analyze the structural changes of the proteins upon interaction with these molecules. (Figure 21) The analysis was done at 37 ºC and pH 7.4 to understand the structural characteristics in physiological conditions. In order to analyze the spectrum, Bestsel online tool was used and percentage of each structural element was calculated (Table G1, Figure G1). (Micsonai, Wien et al. 2015)

α-helices, anti parallel β-sheets and turns was observed in OCN secondary structure. OCN-calcium interaction increased the degree of compact structures. The percentage of helices and anti parallel β-sheets was increased while the percentage of turns was decreased. (Figure 21, Table G1, Figure G1) The increase in compact structures could be explained by the interaction of OCN and calcium. Hauschka *et al.* have shown that helix content of native chicken osteocalcin was increased 30% and the helix content of decarboxylated chicken osteocalcin was increased 8%. (Hauschka and Carr 1982) The increase of helix content in our recombinant osteocalcin was 3.4%. This could be due to the lack of carboxylation. Although the effect of Ca^{2+} and other cations on the secondary structure of OCN was extensively studied (Wians, Krech et al. 1983; Dowd, Rosen et al. 2001), there is no information in the literature if OCN interacts with organic and inorganic phosphate and if the secondary structure of OCN is affected or not upon these interactions. In this study, the interactions of OCN with organic and inorganic phosphates were also studied. While the interaction of OCN with organic phosphate resulted in no change in the protein structure, the interaction of OCN with inorganic phosphate disrupted secondary structure. (Figure 21, Table G1, Figure G1) According to enzyme kinetics and CD spectroscopy results, OCN-organic phosphate interaction occurred without any conformational change. (Figure 20) On the other hand, OCN-inorganic phosphate interaction altered the secondary structure of the protein, the helices were largely disrupted and more anti-parallel β-sheets were formed. (Figure 21, Table G1, Figure G1)

OPN formed α-helices, anti parallel β-sheets and turns in addition to random coils. Upon addition of Ca^{2+}, secondary structure of OPN was largely conserved. (Figure 21, Table G1, Figure G1) The conservation of secondary structure implies that the interaction of Ca^{2+} and OPN is not via compact domains but via flexible unstructured

domains, which are mainly D-rich HAP binding domain and ASARM peptide (Kazanecki, Uzwiak et al. 2007; Hunter, O'Young et al. 2010) Upon addition of β-GP, the secondary structure of the protein was slightly changed, but the anti-parallel β-sheet structures were still conserved. (Figure 21, Table G1, Figure G1) Because the interaction of OPN with β-GP was resulted in protection of the secondary structure, OPN interacts with β-GP without any conformational change, or no interaction occurs. Similar to OCN, OPN interacted with organic phosphate. These observations were supported by kinetic experiments. (Figure 20) Upon addition of $HPO4^{2-}$, the α-helical and parallel β-sheet contents of the protein increased while anti-parallel β-sheet content decreased. (Figure 21, Table G1, Figure G1) These changes may be due to an interaction that stabilizes the protein.

Gorski *et al.* has previously studied secondary structure of rat OPN in the presence and absence of Ca^{2+}. They have found that low concentrations of OPN showed random coil conformation, while high concentrations of OPN had helices, β-sheets and turns (29,24,17%, respectively). (Gorski, Kremer et al. 1995) Other studies have shown that OPN was largely unstructured. Phosphorylation of serines in bone and milk OPN could be responsible for the increase in flexibility on the secondary structure. (Gericke, Qin et al. 2005; Kazanecki, Uzwiak et al. 2007) For instance, phosphorylation of serine at LKFRISHEL sequence disrupt β-sheet structure. (Kazanecki, Uzwiak et al. 2007) Absence of phosphorylation may be the reason why some compact structures were observed in our system.

Kazanecki *et al.* was predicted 2 β-sheet regions in the secondary structure of OPN: SVVYGLR and LKFRISHEL. (Kazanecki, Uzwiak et al. 2007) Positively charged residues in these regions (K, R, H) may contribute to increase in β-sheet content

upon addition of $HPO4^{2-}$. Positively charged residues are probably neutralized in the presence of $HPO4^{2-}$, makes these regions more compact and stabilize β-sheets.

Both OCN and OPN bind to β-GP without any significant conformational change, as the proteins affected ALP enzymatic activity through competitive binding. (Figure 20) The helical structures in OCN was disrupted upon $HPO4^{2-}$ binding; this may explain why OCN was less effective in increasing the reaction rate constant of ALP phosphatase activity compared to OPN. The formation of inorganic phosphate ions during phosphatase assay led to reduced binding of OCN to organic phosphate (Figure 20) due to the disruption in the secondary structure of OCN.

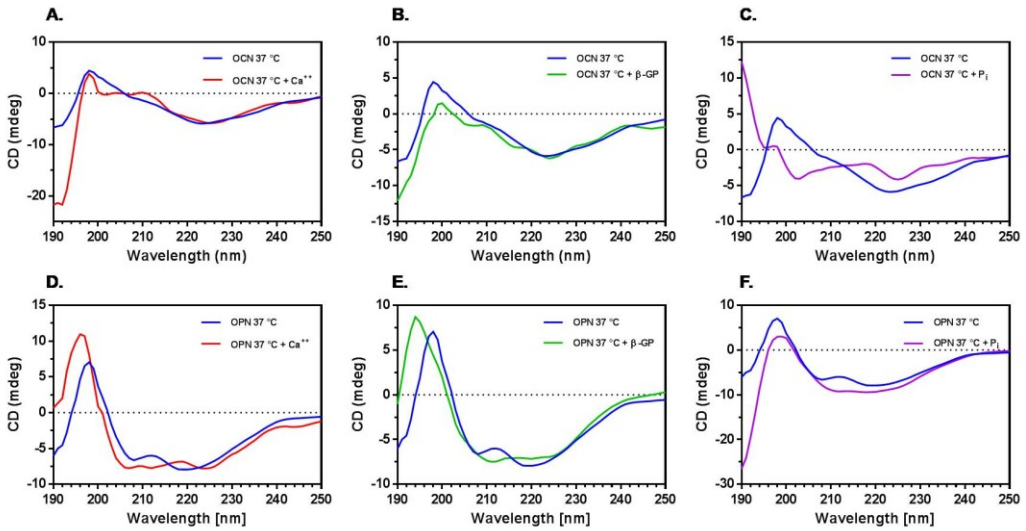

Figure 21. CD spectrum measurement for secondary structure analysis of OCN and OPN in the presence of biomineralization molecules. A.OCN helical and anti parallel structures was increased following the addition of Ca^{2+}. **B-C.** α-helical structure of OCN is disrupted in the presence of inorganic phosphate, not organic phosphate. **D.** Secondary structure of OPN following the addition of Ca^{2+} is largely conserved. **E-F.** OPN becomes more compact in the presence of inorganic phosphate, not the organic phosphate.

3.3.4 Effect of recombinant proteins on ALP-mediated *in vitro* biomineralization

The effect of OCN and OPN on the formation of CaP crystals *in vitro* was characterized by spectrophotometer measurement, electron microscopy imaging, EDS and XPS analysis. BB was prepared to provide calcium and phosphate source for crystal formation. ALP unit enzyme concentration was determined to be 5 U after several tests in order to find the concentration range that was high enough to see initial mineral formation within 1 h and low enough to differentiate the mineral formation rates of different groups. (data not shown) 820 nm light scattering in the first 1 h for each reaction was recorded to monitor crystal formation since it is known that CaP crystals scatter light at 820 nm. (Gungormus, Fong et al. 2008) The initialization of crystal formation was recorded, the differences between groups were differentiated, and $k_{observable}$ values were calculated from the slope of the linear regions of the scattering measurement curve in order to analyze the changes of initial mineral formation rate among groups.

3.3.4.1 Effect of OCN on ALP activity

3.3.4.1.1 Spectrophotometric measurements

First, the effect of OCN on the initial mineral formation rate was recorded. Surprisingly, the addition of ALP before or after the BB affected the results. When ALP was added before the BB, no difference was observed between the reaction

rates of ALP and the different concentrations of OCN. (Figure 22, 26) However, when ALP was added after the BB, the reaction rate was significantly reduced upon increasing concentrations of OCN. (Figure 23, 26) The biomineralization reaction starts when the two essential components are combined; ALP and the BB. ALP converts β-GP to P_i, and these inorganic phosphates interact with the Ca^{2+} ions in the solution to form initial CaP crystals. (Siller Alejandro and Whyte Michael 2017) First, amorphous CaP aggregates are formed till CaP particles reach a critical size for nucleation. Once a critical size is reached, CaP particles start to grow up and amorphous CaP aggregates are converted to more crystalline compounds. (Birkedal 2017) When the BB was added before ALP and OCN, OCN has time to interact with Ca^{2+} ions in the solution. The interaction of OCN with Ca^{2+} ions increased α-helices and anti-parallel β-sheets. (Figure 21, Table G1, Figure G1) Binding of OCN to Ca^{2+} not only decreased the number of free Ca^{2+} ions, but it also delayed formation of critical size nuclei and reduced the reaction rate. (Figure 23, 26)When the BB was added after ALP, P_i ions started to form before the interaction of OCN with the Ca^{2+} ions because the P_i ions disrupted the helical structure of OCN. (Figure 21), the affinity of OCN to Ca^{2+} ions was lowered. Consequently, OCN cannot delay critical size nuclei formation, and the crystal formation reaction hastens. (Figure 22, 26)

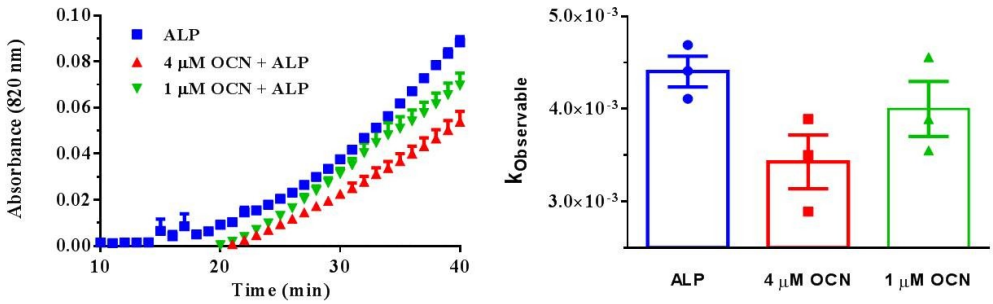

Figure 22. *In vitro* biomineralization in the presence of ALP and OCN-P_i. A. Initial mineral formation was detected by spectrophotometer when OCN and ALP were added into the reaction before BB (Ca^{2+} and β-GP). Initial mineral formation rate was calculated based on first 30 minutes of mineral formation. The legends in the first graphic are also valid for the columns in $k_{observable}$ graphic. Statistical analysis was performed in Graphpad Prism software by One-Way ANOVA. BB: 24 mM $CaCl_2$, 14.4 mM β-GP, 25 mM Tris-HCl (pH=7.4) ALP (5 U), 1 mM $MgCl_2$ used for each reaction. All samples are in 25 mM Tris-HCl, pH=7.4.

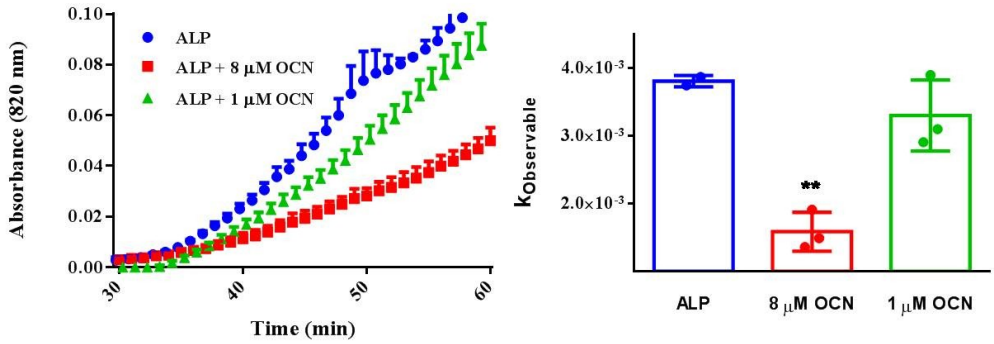

Figure 23 *In vitro* biomineralization in the presence of ALP and OCN-Ca^{2+}. A. Initial mineral formation was detected by spectrophotometer when OCN and BB Ca2+ and β-GP) were added into the reaction before ALP. Initial mineral formation rate was calculated based on first 30 minutes of mineral formation. The legends in the first graphic are also valid for the columns in $k_{observable}$ graphic. Statistical analysis was performed in Graphpad Prism software by One-Way ANOVA. BB: 24 mM $CaCl_2$, 14.4 mM β-GP, 25 mM Tris-HCl (pH=7.4) ALP (5 U), 1 mM $MgCl_2$ used for each reaction. All samples are in 25 mM Tris-HCl, pH=7.4.

3.3.4.1.2 Electron microscopy imaging

SEM imaging was performed to observe the effect of OCN on mineral shape. After 24 h of incubation at 37 ºC, the crystal size decreased and the crystals became more uniform compared to ALP only. (Figure 24, 26) The decrease in crystal size was quantified by ImageJ software by measuring the crystal area of 20 (ALP) and 18 (ALP and OCN) crystals. The average crystal size decreased from 2.17 μm^2 to 0.44 μm^2 and the standard error of the mean (SEM) was decreased from 0.44 to 0.02 upon OCN addition to the reaction indicating OCN not only caused a decrease in crystal size, but also narrowed down the size distribution of crystals. (Figure 24, 26)

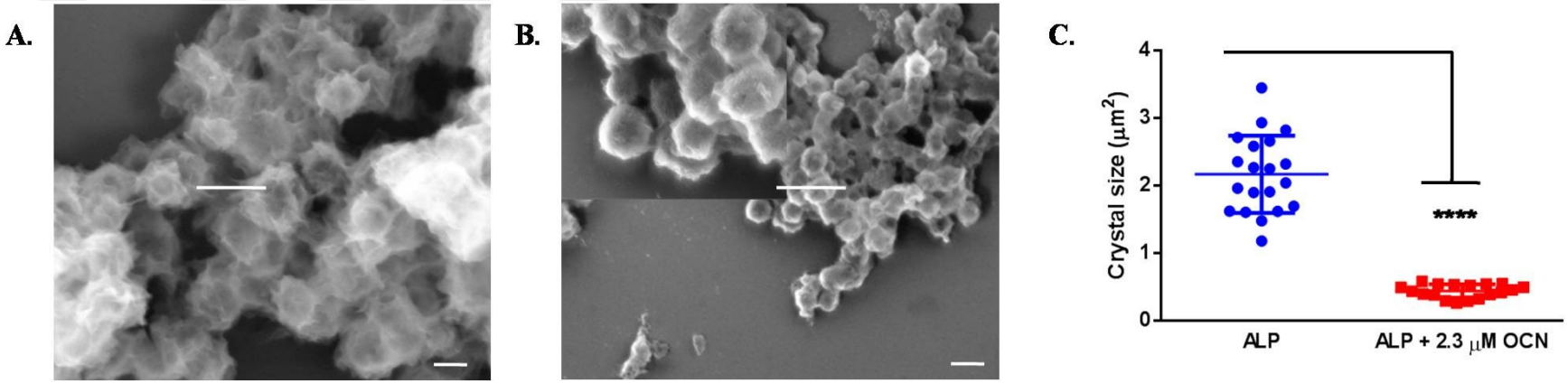

Figure 24. Electron microscopy imaging of *in vitro* biomineralization in the presence of ALP and OCN. A. SEM imaging of mineral formation in the presence of ALP after 24 h of incubation at 37 ˚C. B. SEM imaging of mineral formation in the presence of ALP and OCN after 24 h of incubation at 37 ˚C. A-B. Scale bars represent 1 μm. C. Crystal size is measured by the ImageJ program measure tool from SEM images from N=20 ± SEM and N=18 ± SEM crystals. Unpaired t-test was performed to analyze statistical significance. BB: 24 mM $CaCl_2$, 14.4 mM β-GP, 25 mM Tris-HCl (pH=7.4) ALP (5 U), 1 mM $MgCl_2$ used for each reaction. All samples are in 25 mM Tris-HCl, pH=7.4.

3.3.4.1.3 Elemental Analysis

In order to analyze crystallinity of the minerals, the surface Ca:P ratio was calculated based on the XPS measurements. XPS is based on scanning the micro focused x-ray beam across the sample surface. Exciting a sample surface with mono-energetic Al kα x-rays causes photoelectrons to be emitted from the sample surface. The energy of the emitted photoelectrons is measured and from the binding energy and intensity of a photoelectron peak, the elemental identity, chemical state, and quantity of a detected element can be determined.

Higher Ca:P ratio is an indicator of higher degree of crystallinity in CaP crystals. (Birkedal 2017) Although we expected an increase in the Ca:P ratio of the minerals because the minerals are more ordered, there is no statistically significant increase in the Ca:P ratio. (Figure 25, 26) This may be due to the measurement method. XPS only detects surface atoms. The surface minerals may be newly formed less crystalline forms, and the inner layers could still be more crystalline. (Wang and Nancollas 2008) Therefore, EDS analysis was performed to analyze crystallinity of the minerals. (Figure 25, 26) However, the difference cannot be observed. The inner layers are not more crystalline than the surface. So, it was depicted that OCN does affect crystal size, but not crystallinity during mineral formation. The decrease in crystal size could be due to inhibition of crystal growth at mineral surfaces.

It should also be noted that the composition of mineralization reaction is constant in our system. So, while the crystallization proceeds, the OH^- ions are incorporated into crystals leaving H^+ ions in solution, which makes the environment more acidic by the time compared to the initial phase (pH 7.4). (Isbell, Du et al. 1993) H^+ ions bind to negatively charged residues on OCN and OCN becomes more compact due to

neutralization of the charges. (Hunter 2013) When OCN becomes more compact, α-helical content is promoted, although to a lesser extent compared to Ca^{2+} binding. (Hunter 2013) The interaction of OCN and H^+ ions could help the inhibition of crystal growth by making OCN more helical and more prone to binding crystal lattices by releasing H^+ ions. (Hunter 2013)

Furthermore, positively charged arginine residues in OCN might be involved in interaction with HAP crystals since they can bind to phosphate ions in crystal structure. (Hauschka and Carr 1982)

Although some studies suggest that inhibition of crystal growth in the presence of OCN diminished upon decarboxylation (Romberg, Werness et al. 1986), others support the idea that decarboxylation is reduced the effect of OCN to inhibit crystal growth. (Hauschka and Carr 1982) Our results consistent with the latter that crystal growth inhibition is possible with uncarboxylated recombinant OCN. The controversial results may be explained by the differences in experimental setups, and measurement methods, most of the studies measure crystal growth but not crystallinity of the final minerals.

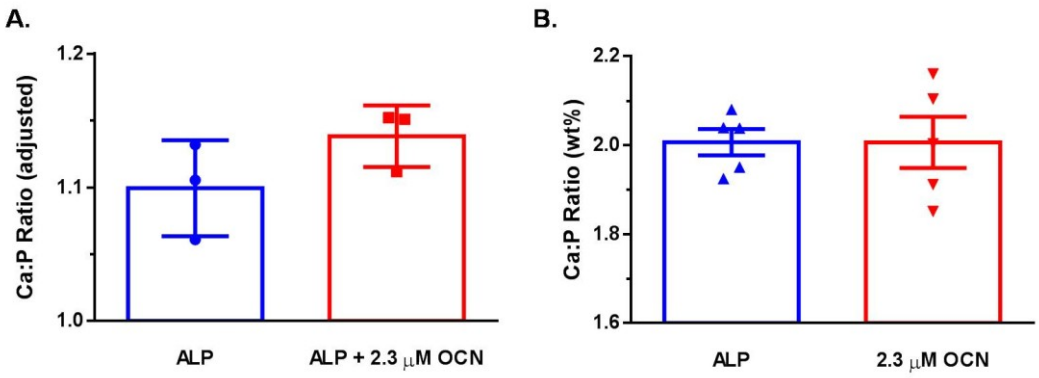

Figure 25. Ca:P ratio of the minerals formed in the presence of ALP and OCN after 24 h of incubation at 37 ˚C detected by XPS and EDS, respectively. 3 points with 400 µm spot size were selected for XPS scanning. Unpaired t-test was performed to analyze statistical significance. 5-6 points were selected EDS analysis. One-Way ANOVA was performed to analyze statistical significance.

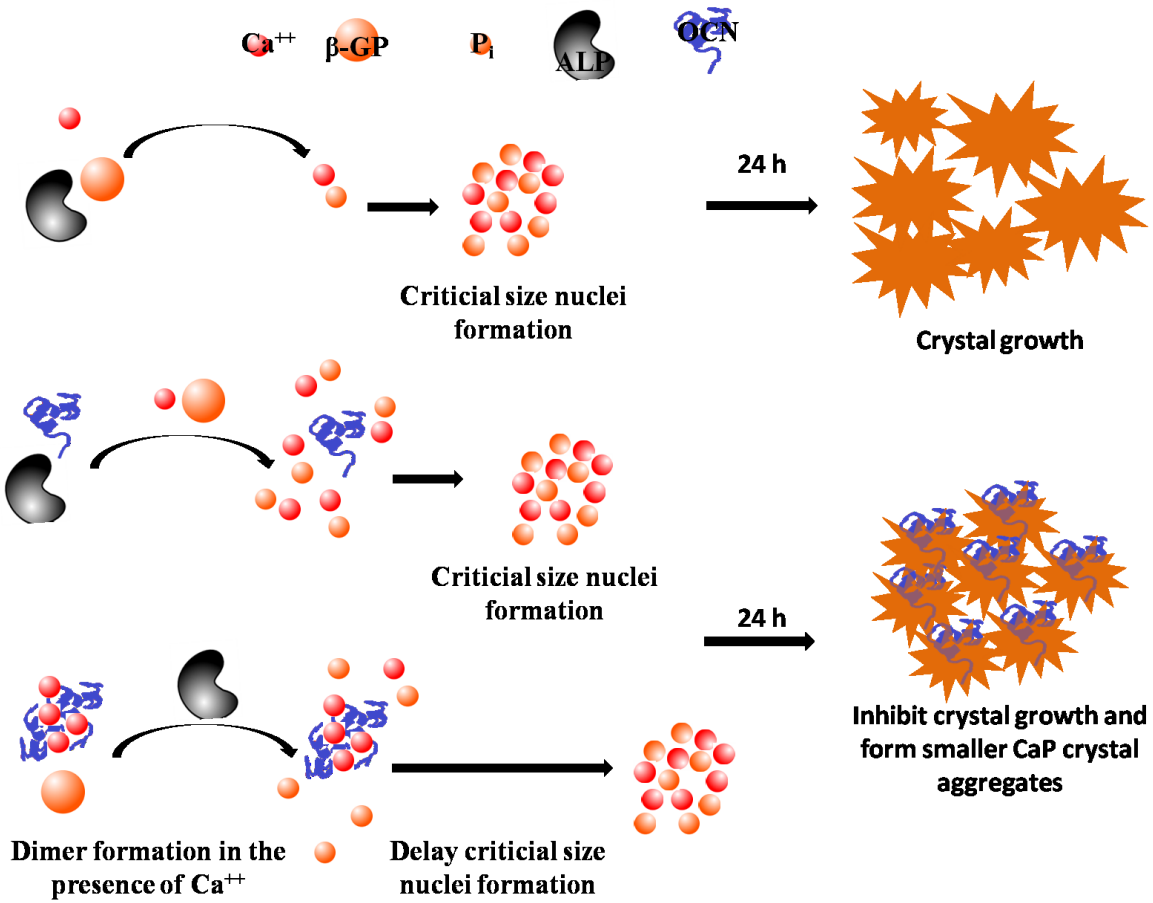

Figure 26. Schematic representation of the reaction with ALP in the absence of OCN, and ALP was added into reaction before or after BB (Ca^{2+} and β-GP).

3.3.4.2 Effect of OPN on ALP activity

3.3.4.2.1 Spectrophotometric measurements

Then, the effect of OPN on the initial mineral formation rate was analyzed. The addition of ALP before or after the BB affected the results, as with OCN, but in a different manner. When BB added lastly to the reaction mixture, the reaction started earlier and occurred faster in the presence of OPN compared to ALP only condition. (Figure 27, 28) One possible explanation is OPN can interacts to both Ca^{2+} and P_i ions, but it has a higher affinity to P_i ions. Because P_i helps to conserve the compact structures of OPN (Figure 21), OPN sequesters more P_i ions, and this hastens the reaction. On the other hand, when ALP is added lastly to the reaction mixture, OPN first interacts with Ca^{2+} ions, not the P_i ions. This interaction prevents OPN to be more compact when P_i is formed after addition of ALP. (Figure 21) Upon the addition of ALP, P_i formation starts, but P_i can no longer interacts with OPN or affinity of OPN to P_i was lowered. (Figure 27) Ergo, the reaction started later compared to the former case. (Figure 28) Subsequently, the reaction rate was calculated from the slope of the reaction curve (first 30 minutes of linear region of scattering plot). Although the mineral formation started earlier when OPN and ALP was added into the reaction before BB, there was no difference between the reaction rates of the groups. (Figure 27, 28)

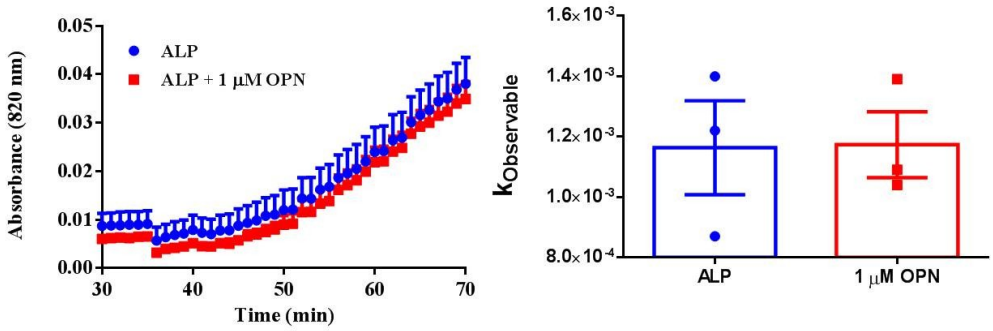

Figure 27. ***In vitro*** **biomineralization in the presence of ALP and OPN-Ca^{2+}.** Initial mineral formation was detected by spectrophotometer when BB and OPN added into the reaction before ALP. Initial mineral formation rate was calculated based on first 30 min of mineral formation. (Error bars represents N=3 ± SEM.) The legends in spectrophotometry measurement graphic are also valid for the columns in $k_{observable}$ graphics. Statistical analysis was performed in Graphpad Prism software by One-Way ANOVA. BB: 24 mM $CaCl_2$, 14.4 mM β-GP, 25 mM Tris-HCl (pH=7.4) ALP (5 U), 1 mM $MgCl_2$ used for each reaction. All samples are in 25 mM Tris-HCl, pH=7.4.

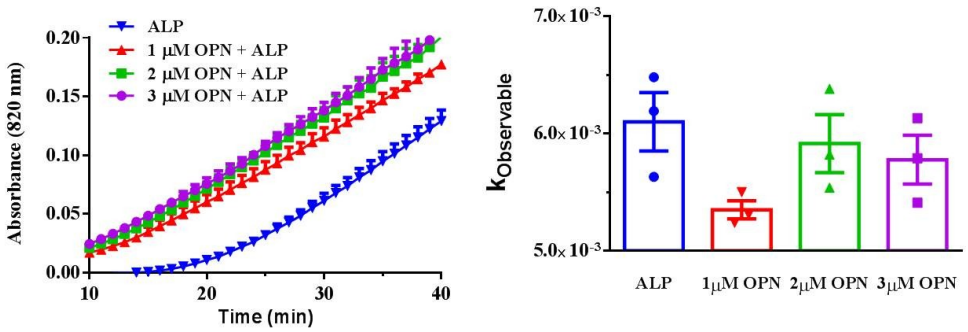

Figure 28. In vitro biomineralization in the presence of ALP and OPN-P_i. Initial mineral formation detected by spectrophotometer when ALP and OPN added into the reaction before BB. Initial mineral formation rate was calculated based on first 30 min of mineral formation. (Error bars represents N=3 ± SEM.) The legends in spectrophotometry measurement graphic are also valid for the columns in $k_{observable}$ graphics. Statistical analysis was performed in Graphpad Prism software by One-Way ANOVA. BB: 24 mM $CaCl_2$, 14.4 mM β-GP, 25 mM Tris-HCl (pH=7.4) ALP (5 U), 1 mM $MgCl_2$ used for each reaction. All samples are in 25 mM Tris-HCl, pH=7.4.

3.3.4.2.2 Electron microscopy imaging

After 24 h of incubation at 37 ºC, SEM imaging was performed, and there was no observable difference between ALP only and ALP and OPN containing groups in terms of crystal size and shape. (Figure 29) The crystal size was quantified by ImageJ software by measuring the crystal area of 14 (ALP) and 21 (ALP and OPN) crystals. The average crystal size was 3.8 μm^2 and 3.4 μm^2 and the SEM was 0.52 μm^2 and 0.31 μm^2, respectively. Unpaired t-test analysis revealed no significant difference. Early and late phases of crystal formation was illustrated in Figure 31.

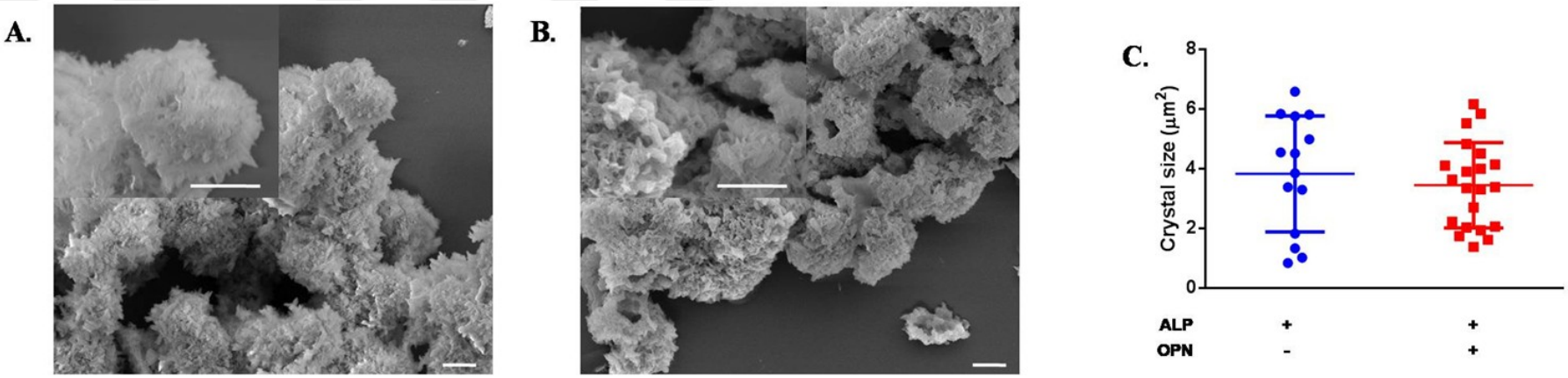

Figure 29. A.SEM imaging of mineral formation in the presence of ALP after 24 h of incubation at 37 ˚C. B. SEM imaging of mineral formation in the presence of ALP and 3 µM OPN after 24 h of incubation at 37 ˚C. A-B. Scalebars represent 1µm. C. Crystal size is measured by the ImageJ program measure tool from SEM images from N=14 ± SEM and N=21 ± SEM crystals. Unpaired t-test was performed to analyze statistical significance.

3.3.4.2.3 Elemental Analysis

Then, the surface Ca:P ratio was calculated based on the XPS measurements. The Ca:P ratio decreased when the OPN concentration increased to 3 µM. (Figure 30, one-way ANOVA) This may be explained by the faster formation of CaP crystals, which results in less crystallinity at the surface or at all. In order to understand whether the change is at the surface or not, Ca:P ratio was also investigated by EDS analysis and the results were similar to XPS. (Figure 34) Ca:P ratio was reduced in the presence of OPN, same as the XPS analysis.

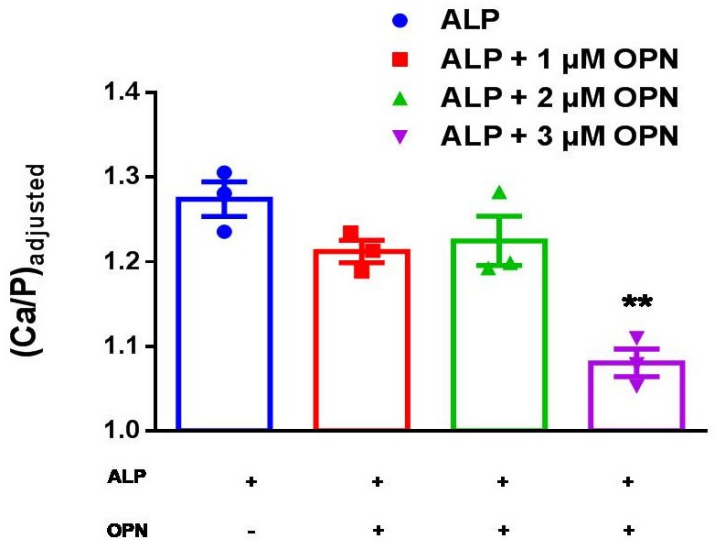

Figure 30. Surface Ca:P ratio of the minerals formed in the presence of ALP and OPN after 24 h of incubation at 37 ˚C detected by XPS. 3 points with 400 µm spot size are selected for scanning. ONE-WAY ANOVA was performed to analyze statistical significance of each sample compared to ALP.

Our results consistent with the literature that unphosphorylated OPN does not inhibit mineralization reaction. (Gericke, Qin et al. 2005) Yet, it hastened mineralization in

the presence of inorganic phosphate in our study. This could be due to the nucleator property of OPN, which was observed when OPN cross linked to gap regions of Collagen fibers via TG activity in bone tissue (Kaartinen, Pirhonen et al. 1999). Upon crosslinking, OPN forms aggregates which can induce mineralization event. (Kazanecki, Uzwiak et al. 2007) Promotion of nucleation was achieved in another study by using high concentrations of nonphosphorylated OPN peptide (NPP). (Wang, Guan et al. 2008) This peptide is highly negatively charged containing 7 aspartic acid and 1 glutamic acid residue. Only high concentrations of this peptide promoted the nucleation event since it was prone to aggregation easily. This aggregation could be mimicking cross linked aggregation of OPN. (Wang, Guan et al. 2008) In our study, we observed nucleation of CaP crystals in the presence of OPN, which can be also mimicking the aggregation of OPN which was shown in previous research. (Kaartinen, Pirhonen et al. 1999; Wang and Nancollas 2008) Contrary to OCN, OPN has no effect on crystal size, suggesting it does not alter crystal growth. (Figure 29) The results are consistent with literature, where nonphosphorylated OPN has no effect on crystal growth inhibition. (Ohri, Tung et al. 2005; Kazanecki, Uzwiak et al. 2007; Wang, Guan et al. 2008; Hunter, O'Young et al. 2010; Hunter 2013)

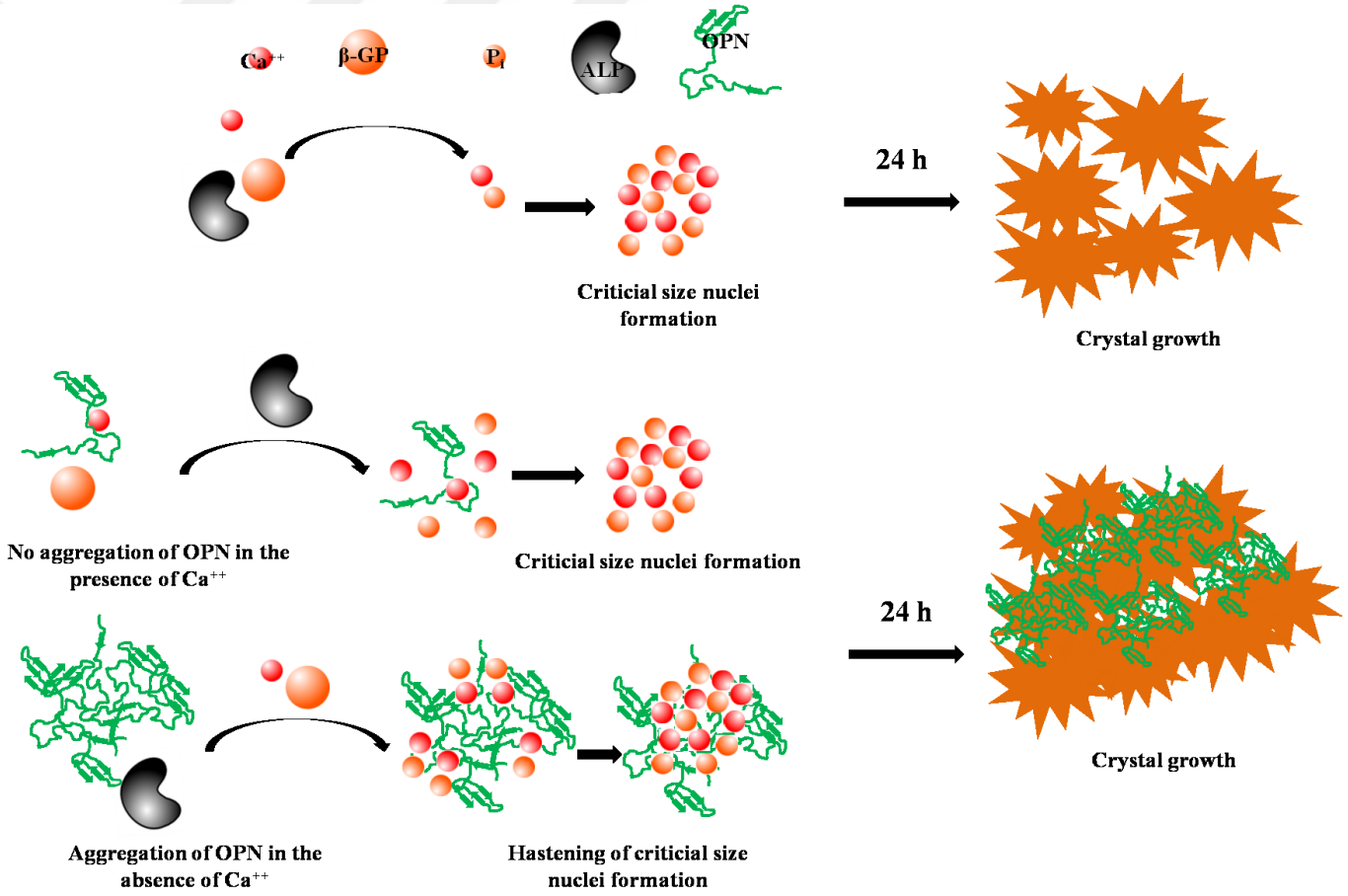

Figure 31. Illustration of initial and late phases of CaP crystal formation in the presence of ALP only, and both ALP and OPN.

3.3.4.3 Effect of combination of OCN and OPN on ALP activity

3.3.4.3.1 Spectrophotometric measurements

To observe the combined effects of OCN and OPN on biomineralization, a protein titration experiment was performed. The OPN concentration was increased when the OCN concentration was constant to see if the behavior of each protein changes in the presence of the other protein. Based on previous experiments, we hypothesized that the binding of calcium to OCN should decrease the crystal formation rate, yet the addition of P_i-bound OPN should increase the reaction rate. In the reaction set-up, the BB contains both Ca^{2+} and ß-GP, and after being added to the buffer, proteins immediately interact with the ions. In the presence of OCN, reaction rate was decreased compared to ALP only. (Figure 32) In the presence of OPN, reaction rate did not change but reaction started earlier. (Figure 33) When OCN and OPN was used together, reaction started earlier compared to ALP only condition but later compared to OPN. (Figure 32, 33) In addition, reaction rate decreased compared to ALP only condition. It means OCN still delays crystal formation and OPN still hastens reaction. (Figure 32, 33) The effects of two proteins can be used in single reaction. Early and late phases of crystal formation was illustrated in Figure 35.

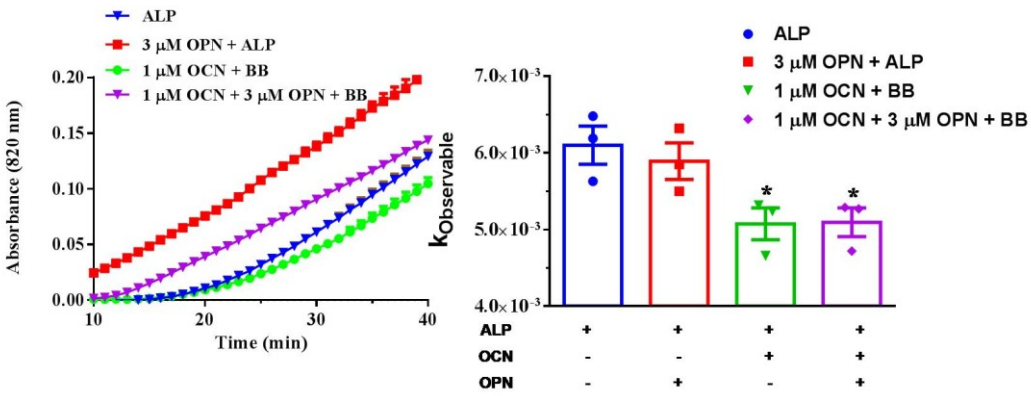

Figure 32. ***In vitro*** **biomineralization in the presence of ALP and varying concentrations of OCN and OPN.** Initial mineral formation detected by spectrophotometer. Initial mineral formation rate calculated based on first 40 min of mineral formation (ONE-WAY ANOVA). BB: 24 mM $CaCl_2$, 14.4 mM β-GP, 25 mM Tris-HCl (pH=7.4) ALP (5 U), 1 mM $MgCl_2$ used for each reaction. All samples are in 25 mM Tris-HCl, pH=7.4.

3.3.4.3.2 Electron microscopy imaging

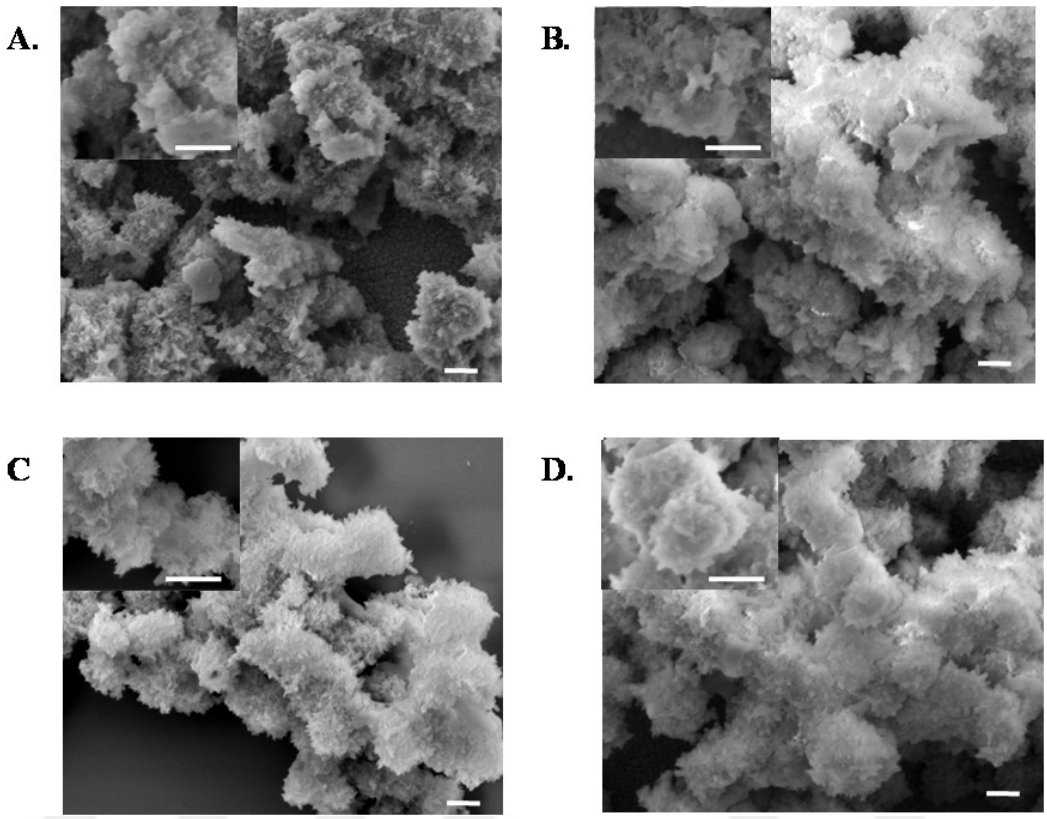

Figure 33. SEM imaging of mineral formation after 24 h of incubation at 37 ˚C in the presence of ALP only, ALP and 3 µM OPN, ALP and 1 µM OCN, and ALP, combination of, 3 µM OPN and 1µM OPN, respectively. Scalebars represents 1 µm.

3.3.4.3.3 Elemental Analysis

After 24 hours, SEM imaging and EDS analysis performed to observe the effect of proteins on late phases of mineral formation. Ca/P ratio decreased in the presence of OPN, but the addition of OCN reversed the decrease in Ca/P ratio. (Figure 34) Moreover, the surface CaP ratio of commercial HAP (Sigma) was calculated as a positive control. The crystallinity of biominerals formed in our *in vitro* system was higher than that of commercial HAP (Figure H1), and biominerals synthesized in this system can be a promising alternative for osteoblast differentiation and tissue regeneration. (Figure 1)

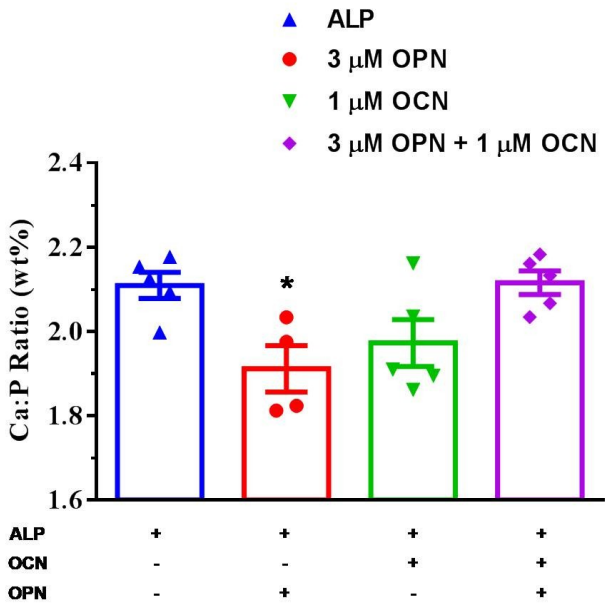

Figure 34. Ca:P ratio of the minerals formed in the presence of ALP and OCN after 24 h of incubation at 37 ˚C detected by EDS. 5-6 points were selected EDS analysis. One-Way ANOVA was performed to analyze statistical significance.

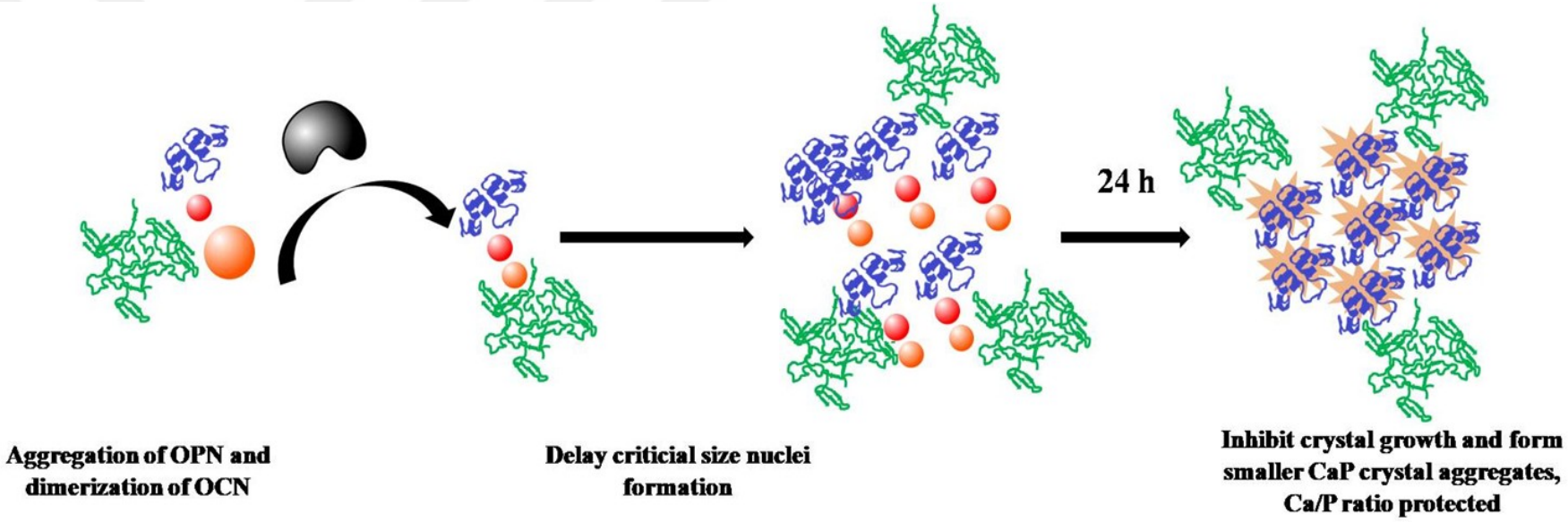

Figure 35. Illustration of initial and late phases of CaP crystal formation in the presence of ALP only, and ALP, OCN and OPN.

4 CHAPTER III: ENGINEERING CELLS FOR BIOMINERALIZATION

4.1 Objective

Synthetic biology enabled cloning of genes from one cell to another, even one organism to another. By this way, reprogramming cells to behave in a different manner became possible. The very popular and exciting example of this is the IPSCs (Induced Pluripotent Stem Cells), in which fibroblasts cells reprogrammed to stem cell state by defined stem cell factors, namely Yamanaka factors. In this study, pluripotent stem cells directly generated from fibroblast cultures by the introducing four factors, Oct3/4, Sox2, c-Myc, and Klf4. (Takahashi and Yamanaka 2006) Similarly, differentiation of embryonic mesenchymal cells to odontoblast-like cells achieved by overexpression of DMP1 (dentin matrix protein 1), an extracellular matrix protein plays important role in biomineralization of bone and dentin. (Narayanan, Srinivas et al. 2001) These examples show that reprogramming a cell to behave like another cell is possible. Another example from literature that support this phenomena is the comparison of the calcifying vascular smooth muscle cells (C-VSMCs) and osteoblasts. Trans-differentiation of VSMCs into C-VSMCs is a pathological condition associated with cardiovascular disease and mortality. The researchers found that VSMC keeps their own identity during ectopic calcification while using mechanisms that osteoblasts use to mineralize. (Alves, Eijken et al. 2014) Based on the information provided from these researches, it is possible to

achieve biomineralization without changing the properties of the host cell by inducing expression of biomineralization-related proteins.

In this part of my thesis project, I am working on programming non-biomineral formation cells for biomineral formation. I have chosen Human Embryonic Kidney Cell Line (HEK293), since they are very easy to grow and transfect very readily, and I have chosen OCN and OPN proteins since they are most abundant noncollagenous proteins in ECM of bone tissue. Transfection of mouse derived OCN and OPN genes was done to achieve differentiation-free bone mineral formation in HEK293 cells. I achieved expression of OCN and OPN proteins in HEK293 cells. Expression of these proteins can lead to formation of mineralized ECM in appropriate conditions. Combination of OCN/OPN expression cell line with an inorganic scaffold or with osteogenic medium (OM) is a promising route for the generation of a cell based bone-like scaffold.

4.2 Materials and Methods

4.2.1 Cell Lines

Human embryonic kidney cells (HEK 293, ATCC) were cultivated in DMEM (Lonza) containing 2 mM L-glutamine, 4.5 g/L glucose, 10% FBS (Gibco, South America origin), penicillin (5000 U/mL) and streptomycin (100 mg/mL) (Gibco) in 5% CO_2 humidified incubator at 37ºC (Binder).

Mouse pre-osteoblast cells (MC3T3, ATCC) were cultivated in α-MEM (Lonza) containing 2 mM L-glutamine, 10% FBS, penicillin (5000 U/mL) and streptomycin (100 mg/mL) in 5% CO2 humidified incubator at 37ºC (Binder).

4.2.2 Differentiation of Pre-Osteoblast Cells

Osteogenic Medium (OM) (50 µg ascorbic acid, 10 mM β-GP in α-MEM Growth Medium) was prepared freshly. MC3T3 pre-osteoblast cells were cultured for 14 days in OM. OM was renewed for every 2-3 days. After 14 days, the cells were resuspended in Trizol and RNA isolation was performed.

4.2.3 Plasmid construction

Mouse osteoblast cDNA Library was synthesized by iScript cDNA Synthesis Kit (Biorad) Mouse osteocalcin (mOCN) and mouse osteopontin (mOPNa) cDNAs were amplified by the primers listed in Table B1 from total RNA of differentiated MC3T3 cells. 6X-Histidine tags were added to the C-terminals by the reverse primers. 22 bp overhangs added both N- and C-terminals complementary to the vector. pCDNA3 GFP LIC cloning vector (6D) was a gift from Scott Gradia (Addgene plasmid # 30127). GFP was removed from the vector with restriction enzymes HindIII (NEB) and XbaI (NEB). PCR amplified mOCN (477 bp) and mOPNa (948 bp) cDNAs were cloned into linearized pCDNA3 vector by Gibson Assembly (NEB Gibson assembly kit) The assembly product was transformed into DH5α chemically competent cells according to the protocol described 3.2.1, and incubated at 37 ºC for 16 hours.

Positive colonies was selected and digested with HindIII and XbaI. Positive clones was verified by sequencing. pCDNA3-GFP, pCDNA3-mOCN and pCDNA3-mOPNa plasmids were isolated by midi-prep plasmid isolation kit (Qiagen).

4.2.4 Transfection

HEK293 cells were seeded in 24 well plate at a concentration of 10^5 cells/well 24 hours prior to transfection. The cells were incubated in 5% CO_2 incubator at 37 ºC in growth medium. After the cells reach 60-70% confluency, they were transfected with addition of Polyetylenimine (PEI) (Polyscience 23966-1) and one of the plasmids; pCDNA3-GFP, pCDNA3-mOCN and pCDNA3-mOPNa. Briefly, 500 µg DNA was mixed with 50 µl serum-free DMEM, 1500 µg PEI was mixed with 50 µl serum-free DMEM. DNA containing medium was added on PEI containing medium and they were mixed by gentle pipetting. The mix was incubated at room temperature for 20 min before adding on cells. After transfection, the cells were transferred into 5% CO_2 incubator and allowed to express proteins for 24-72 hours.

4.2.5 mRNA and protein isolation

500 µl Trizol was added on each well of 24 well plate. The cells were stored at -80ºC until isolation. Before isolation, samples were thawed and 100 µl chloroform was added on cells. Chloroform added samples were mixed and the samples incubated at room temperature for 2-3 min. Then, the samples were centrifuged at 15000 RPM for 15 min at 4 ºC.

For RNA extraction, aqueous phase was carefully removed and 500 µl isopropanol was added to precipitate RNA. The samples were incubated at RT for 10 min and were centrifuged at 15000 RPM for 10 minutes at 4 ºC. The supernatant was carefully discarded. The pellet was washed with 750 µl 75% EtOH and was centrifuged at 8000 RPM for 8 min. The supernatant was carefully discarded. The pellet was washed with 750 µl 99% EtOH and was centrifuged at 8000 RPM for 8 min. The supernatant was carefully discarded and the samples were allowed to dry at room temperature for 5-10 min. RNA pellet was dissolved in 30 µl ddH_2O and concentration was measured by Nanodrop spectrophotometer.

For protein extraction, 150 µl 99% EtOH was added on Trizol containing fraction to precipitate DNA. The samples were mixed and incubated at room temperature for 2-3 min. Then, the samples were centrifuged at 4600 RPM for 5 min at 4 ºC. Aqueous phase was taken and proteins were precipitated with 750 µl isopropanol. The samples were incubated at room temperature for 10 min and were centrifuged at 15000 RPM for 10 min at 4 ºC. The supernatant was carefully discarded. The protein pellet was washed 3 times in 1 ml 0.3 M Guanidine Hydrochloride in 95% ethanol for 10 min incubation at room temperature for each. The protein pellet was washed in 1 ml 99% EtOH and was incubated at room temperature for 10 min. The supernatant was carefully discarded and the pellet was allowed to dry at room temperature for 5-10 min. The precipitated proteins were stored at -80 ºC and were dissolved in 100 µl 8M Urea, 1% TritonX-100 prior to loading SDS gel.

4.2.6 Quantitative Real Time PCR (qRT-PCR)

cDNA synthesis was performed with 1000 ng mRNA by using iScript cDNA Synthesis Kit (Biorad). Thermocycling conditions were as followed: 25º C 5 min, 46º C 20 min, 95º C 1 min, 4º C Hold. cDNA samples were diluted in 1:10 ratio with ddH_2O prior to qRT-PCR. 200 nM Forward and Reverse Primers were used for each reaction. Primer sequences, amplicon lengths and annealing temperatures were listed in Table B2. iQ Supermix (Biorad) was used to amplify DNA by using the following thermocycling conditions: 95º C 3', (95º C 10", 63 º C (GAPDH) / 57 ºC (OCN) / 60 ºC (OPN) 10-45", 72º C 30", Plate Read, *39X), 95º C 10", (Melt Curve: 65-95º C Increment: 0.5º C), Plate Read 5". Amplicon size 70-150 bp: annealing/extension time: 10". Amplicon size >250 bp: annealing/extension time 45".

4.2.7 Immunocytochemistry (ICC)

HEK 293 cells were transfected with mOCN or mOPNa plasmids with PEI at 80-90% confluency. After 24 hours, the cells were detached and diluted in 1:10 ratio. Diluted cells were seeded on microscope glass coverslips (autoclaved) and incubated for 48 hrs at 37 ºC CO_2 incubator. Medium was aspirated and cells were washed with 1X PBS, fixed with -20 ºC fresh cold EtOH, washed 3*3 min with 1X PBS, permeabilized with 0.2% TritonX 100 in 1X PBS, and washed 3*3 min with 1X PBS. Blocking was done for 1 hr at room temperature with FBS (Fetal Bovine Serum), primary antibody incubation was done for 1 hr at room temperature in moist environment with sealing, wash was done 3*3 min with 1X PBS, secondary antibody incubation was done overnight at +4 ºC in moist environment with sealing, wash

was done 3*3 min with 1X PBS. Images were taken in 1X PBS with an upright fluorescent microscope.

4.3 RESULTS AND DISCUSSION

4.3.1 Cloning, expression and purification

4.3.1.1 Generation of osteoblast cDNA library

Mouse pre-osteoblast cell line MC3T3 was used to express OCN and OPN proteins. MC3T3 cells were thawed from DMSO stock and passaged prior to differentiation. They were differentiated for 14 days in OM. Verification of differentiation was done by Alizarin Red Staining since it binds to Ca^{2+} ions deposited on ECM. (Gregory, Grady Gunn et al. 2004) Alizarin Red staining performed after incubation in osteogenic medium for 14 days. (Figure 37) After verification, the cells were resuspended in Trizol for RNA isolation.

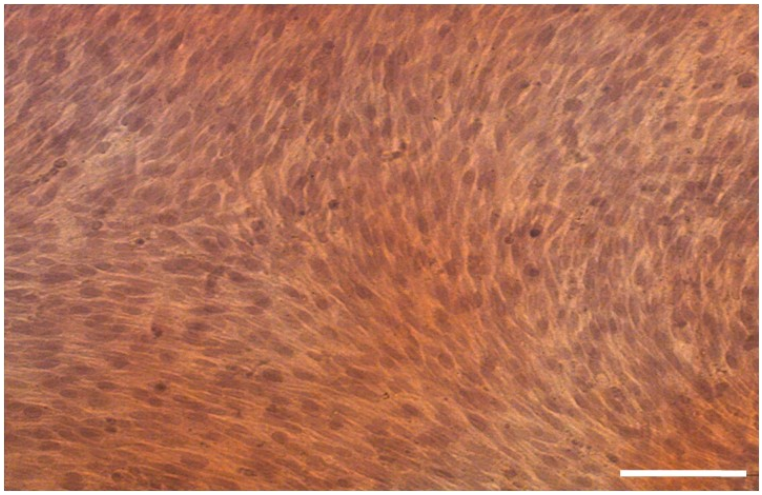

Figure 36. Differentiation of MC3T3 cells for osteoblastic gene expression. Alizarin Red Staining indicates CaP crystal formation of MC3T3 cells differentiated in osteogenic medium for 14 days. Scalebar represents 100 µm.

Total RNA was subjected to cDNA synthesis and a cDNA library was created. mOCN and mOPNa cDNA was amplified by primers listed in Table B1.

4.3.1.2 Cloning mOCN cDNA into mammalian expression plasmid

For cloning mOCN and mOPNa genes into pCDNA3 plasmid, design was done in Benchling platform. (https://benchling.com/editor) Kozak sequence was added to the 5' of the gene fragment after HindIII cut site and KpnI cut site was inserted between Kozak sequence and mOCN gene fragment. EcoRI cut site, GS linker and 4X-his tag was added to the 3' of the mOCN cDNA. HindIII and XbaI cut sites in MCS were chosen for backbone linearization. (Figure 38, 42)

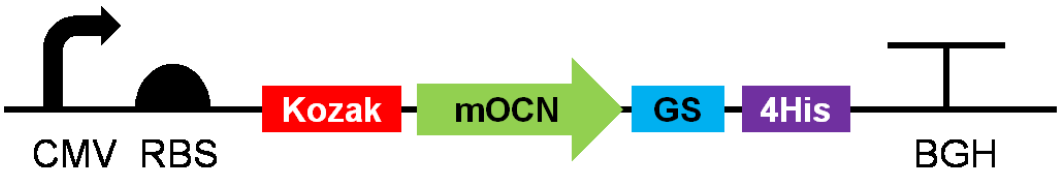

Figure 37. Schematic diagram of mOCN expression cassette. Kozak translation initiation sequence was added for enhanced expression. His-tag was added after a GS linker to the C-terminal of the protein for detection of expression. GS linker provides flexibility to His-tag. CMV promoter and BGH terminator were used for constitutive mammalian gene expression.

First, mOCN was amplified by PCR from cDNA library and the reaction was run by agarose gel electrophoresis. (Figure 39) Expected bands were extracted from agarose gel by gel extraction method (MN) and mOCN PCR amplicon was used for cloning into linearized pCDNA3 plasmid (HindIII-XbaI). (Figure 40)

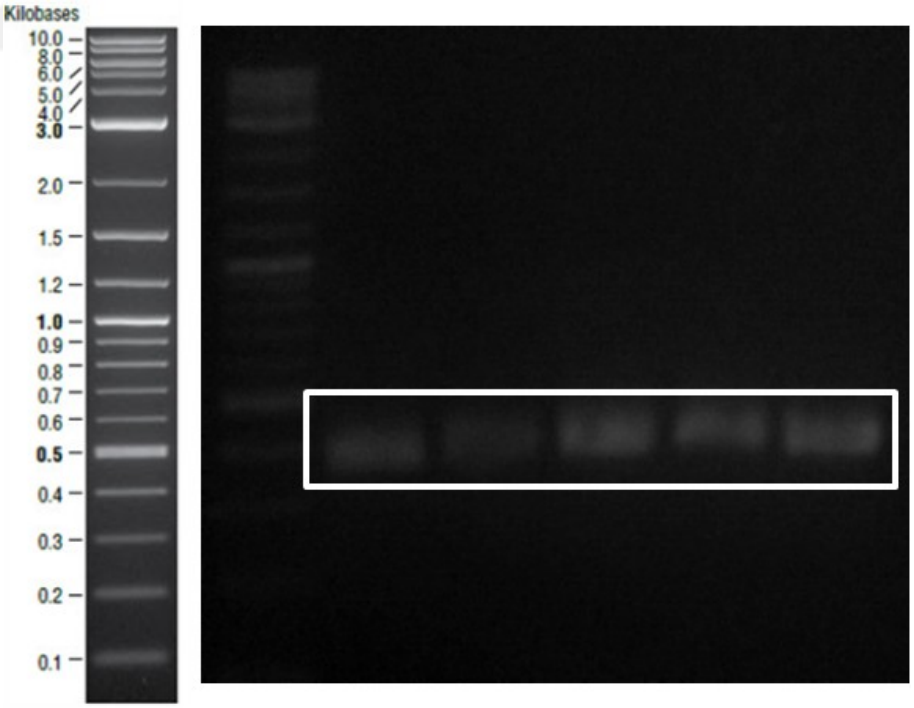

Figure 38. mOCN gene was amplified by PCR. mOCN cDNA was used as template in 2-step PCR. PCR reaction was performed according to the protocol of Q5 Polymerase (NEB). 2-log DNA ladder

(NEB) was used for detection. Tm1= 53-62 ºC (55 ºC best), Tm2= 82 ºC. All temperatures worked. Lane 1: 2 log DNA Ladder (NEB) Lane 2-6: Gradient PCR reactions.

For insertion of mOCN and mOPNa cDNAs, eGFP (800 bp) was removed from the plasmid. The plasmid was digested with XbaI for 2 h and with HindIII for 1.5 h. 2000 ng plasmid was used in 100 µl reaction. Efficiently cut 800 bp insert visible. Linearized pCDNA3 cut fragment was extracted from agarose gel for cloning.

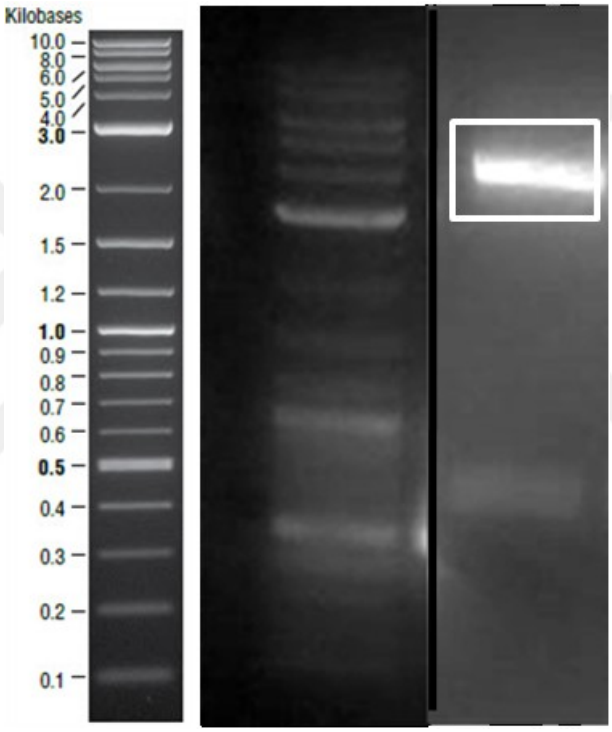

Figure 39. Linearization of plasmid vector pCDNA3-eGFP with HindIII and XbaI digestion. Lane 1 2-log DNA Ladder (NEB), Lane 2-3 double digested plasmid, Lane 4 uncut plasmid control.

For cloning mOCN cDNA, Gibson assembly method was used. 1:1 vector: insert ratio was not successful. (Data not shown) 1:5 vector: insert ratio was used for cloning since mOCN is a small fragment (~300 bp). Reaction performed at 50 ºC for 1 h and directly transformed to DH5α competent cells. Selected colonies were inoculated in LB medium for 16 h and subjected to plasmid isolation. Restriction

enzyme digestion was performed with EcoRI and KpnI enzymes and 300 bp mOCN fragment was observed. 5 colonies were selected for verification of cloning. 4 cuts were successful, 300 bp insert is visible for each. (Figure 41) Purified plasmids were sent to sequencing and one of the clones were selected for further use. Sequencing results were shown in Figure D4.

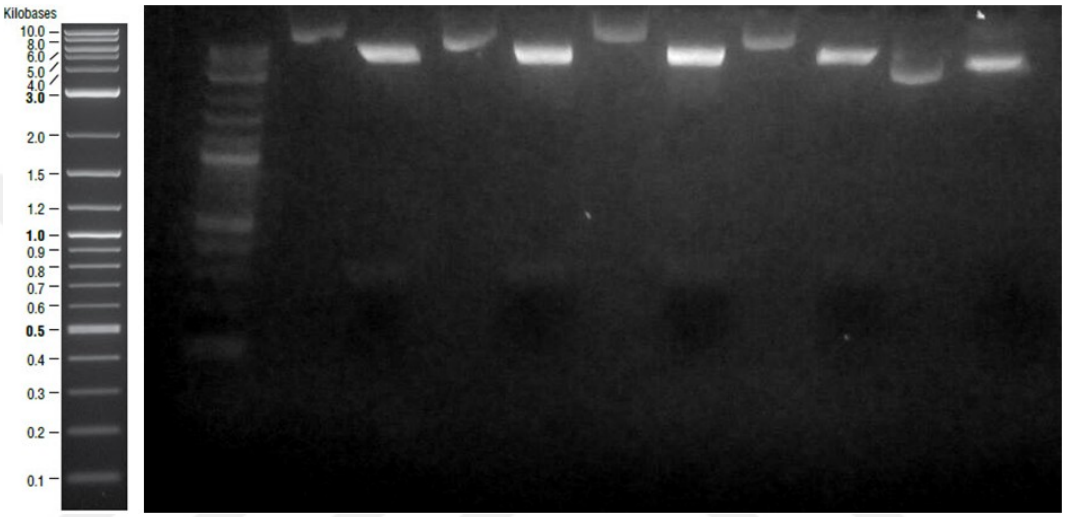

Figure 40. Verification of mOCN-pCDNA3 Gibson Assembly. Restriction enzyme digestion was performed with EcoRI and KpnI. Lane 1: Ladder, Lane 2: uncut plasmid for 1st colony, Lane 3: Double digested plasmid. Lane 4: uncut plasmid for 2nd colony, Lane 5: Double digested plasmid. Lane 6: uncut plasmid for 3rd colony, Lane 7: Double digested plasmid. Lane 8: uncut plasmid for 4th colony, Lane 9: Double digested plasmid. Lane 10: uncut plasmid for 5th colony, Lane 11: Double digested plasmid.

4.3.1.3 Cloning mOPNa cDNA into mammalian expression plasmid

Then, mOPNa was amplified by PCR from cDNA library and the reaction was run by agarose gel electrophoresis. (Figure 43) Expected bands were extracted from

agarose gel by gel extraction kit (MN) and mOPNa PCR amplicon was used for cloning into linearized pCDNA3 plasmid.

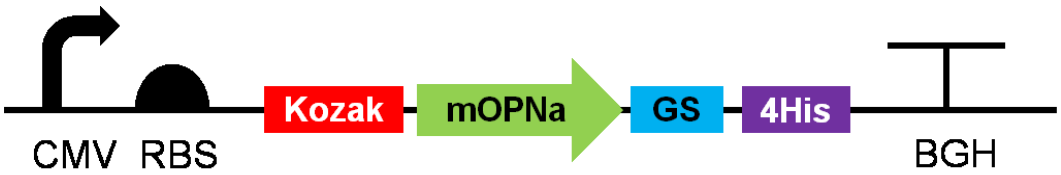

Figure 41. Schematic diagram of mOPNa expression cassette. Kozak translation initiation sequence was added for enhanced expression. His-tag was added after a GS linker to the C-terminal of the protein for detection of expression. GS linker provides flexibility to His-tag. CMV promoter and BGH terminator were used for constitutive mammalian gene expression.

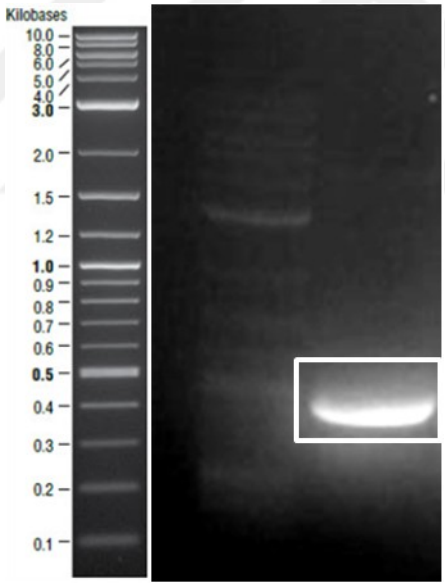

Figure 42. mOPNa gene was amplified by PCR. mOPNa cDNA was used as template in 2-step PCR. PCR reaction was performed according to the protocol of Q5 Polymerase (NEB). 2-log DNA ladder (NEB) was used for detection. Lane 1: 2-log DNA Ladder (NEB), Lane 2-6: mOPNa. cDNA library template was amplified at 62-72 ˚C interval. 900 bp expected band was visible on gel.

For cloning mOPNa cDNA, Gibson assembly method was used. mOCN-pCDNA3 plasmid was double digested with KpnI and EcoRI enzymes in order to obtain

modified linearized plasmid (Kozak sequence, GS linker, 4X his-tag). 1:1 vector: insert ratio was used. Reaction performed at 50 ºC for 1 h and directly transformed to DH5α competent cells. Selected colonies were subjected to colony PCR with the primers used in amplification of mOPNa. 900 bp mOPNa fragment was visible in agarose gel electrophoresis. (Figure 44)

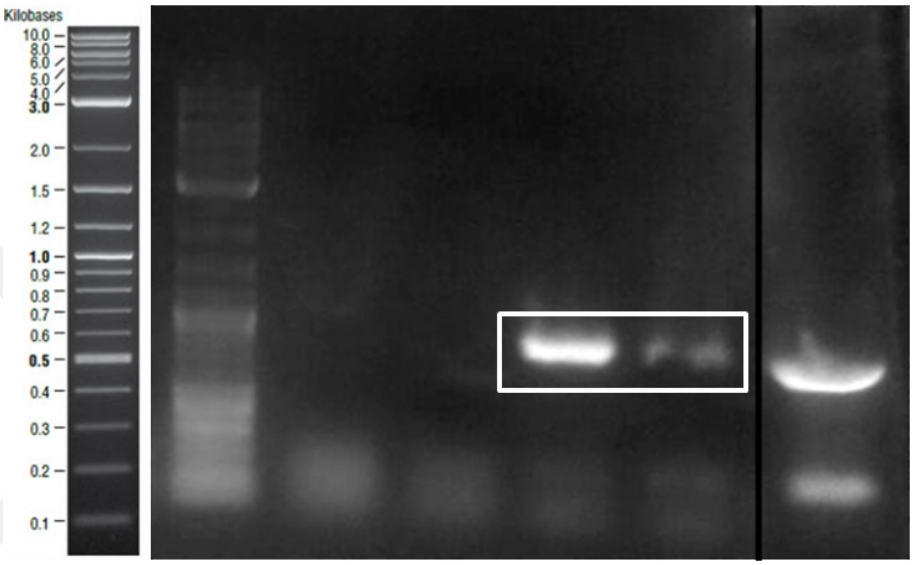

Figure 43. Colony PCR of mOPNa-pCDNA3 plasmid construct with PFU Polymerase. Lane 1: Ladder, Lane 2-5: mOPNa colonies 1-4 amplified at 67 ˚C, Lane 6: mOPNa plasmid (positive control).

Selected colonies (Figure 44, Lane 4-5) were inoculated in LB medium for 16 h and subjected to plasmid isolation. Purified plasmids were sent to sequencing and one of the clones were selected for further use. Sequencing results were shown in Figure D5. There was a missense mutation in D-rich sequence, which is a functional site for mineralization. The mutation was occurred around 50% of the plasmids. Therefore, Transformation of the plasmid was repeated into chemically competent cells and 5 colonies were sent to sequencing. One of the colonies was selected without mutation

and one of the colonies was selected with mutation. (Figure D6) In addition, there was a nonsense mutation at K30. Since it was not in functional site, and it was not be able to eliminated after repeating PCR reaction (Data not shown), the clone was used as it is. The reason could be the presence of mutation in either cDNA library or in mRNA itself.

4.3.2 Transient transfection of mammalian cells for OCN and OPN expression

mOCN-pCDNA3, mOPNa-pCDNA3 and pCDNA3-eGFP plasmids were prepared by midi-prep kit (MN) to remove endotoxins and to obtain high amount of plasmid. 400-2000 ng/µl plasmid were obtained from 150 ml LB culture of bacteria.

HEK293 cell line was thawed and passaged at least once prior to transfection. 10^5 cells were seeded each well in 24 well plate and they allowed to grow for 24 hours.

First, pCDNA-GFP plasmid DNA was used for each group. DNA (500 ng) and PEI (1500 ng) were premixed in serum-free DMEM 20 min before transfection. After adding DNA-PEI solution on cells, the cells were incubated at 37ºC for 24 h and GFP expression was detected. (Figure 45)

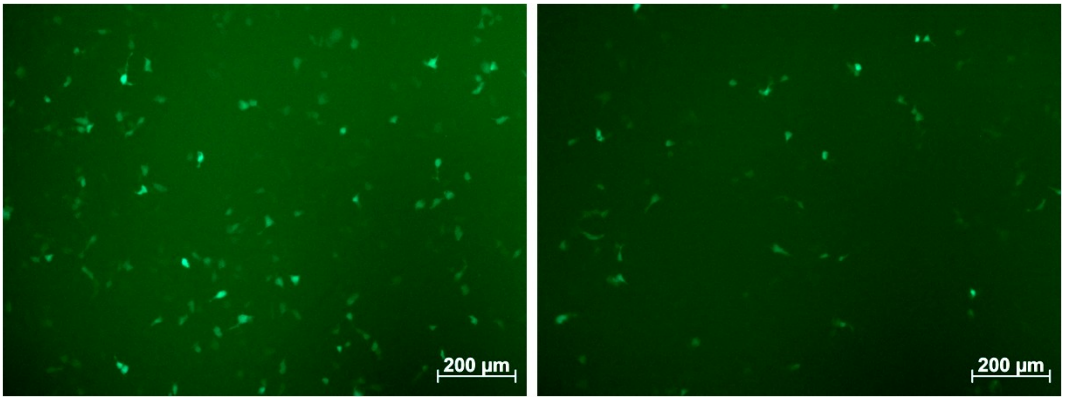

Figure 44. Transfection of HEK293 cells with pCDNA-eGFP and PEI. 1:3 DNA:PEI ratio was used. PEI was prepared in 0.1 N HCl and in 100% EtOH, respectively. 10^5 cells were seeded each well in 24 well plate and they were allowed to grow for 24 h. 500 ng DNA was used for each group. DNA and PEI were premixed in serum-free DMEM 20 min before transfection. Images were taken 24 hours after transfection by an inverted fluorescent microscope.

4.3.2.1 Detection of OCN and OPN expression by qRT-PCR

Then, mOCN and mOPNa plasmids were transfected into HEK293 cells. After 24, 48 and 72 h, the cells were collected for RNA isolation. A simultaneous GFP plasmid transfection was performed to verify successful transfection. A cDNA library was prepared by cDNA synthesis kit after RNA isolation. cDNA library was used as template for qRT-PCR. mOCN and mOPNa forward and reverse primers listed in Table B2 was used to detect exogenous OCN and OPN expression. Primers against human GAPDH was used for analyzing relative mRNA amount. (Figure 46) While OPN mRNA was expressed in high amount for 3 days (10^5 fold incerase), OCN mRNA was less stable and was expressed in lesser amount (10^3 fold incerase). OCN expression reduced by the time probably due to low mRNA length and stability.

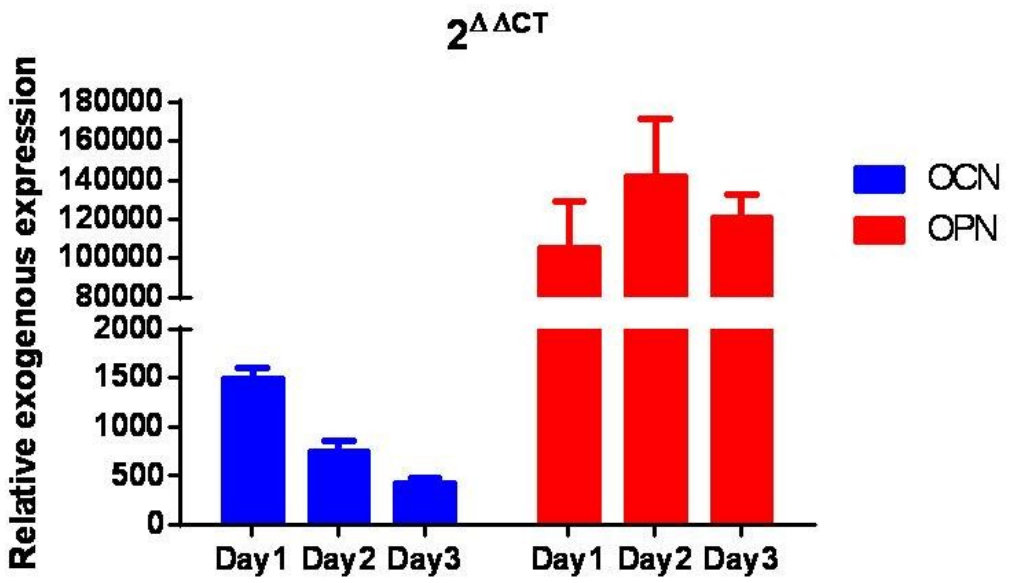

Figure 45. Detection of mOCN and mOPNa mRNA levels in HEK293 cells by qRT-PCR. cDNA library was created from equal amount of mRNA from each biological triplicate before qRT-PCR. Equal amount of cDNA was used in technical triplicate. hGAPDH gene was used to normalize gene expression levels. Untransfected HEK293 cells were used as negative control to calculate relative expression levels.

4.3.2.2 Detection of OCN and OPN expression by SDS-PAGE

OCN and OPN expression could not be detected by SDS-PAGE even after 48 and 72 h of incubation with plasmids. Since OCN and OPN proteins are ECM proteins, they could be secreted outside to cells. SDS-PAGE analysis was not informative to analyze protein expression. Both cell culture supernatant and cell lysate were analyzed for expression; however, no overexpression was observed. (Figure 47, 48)

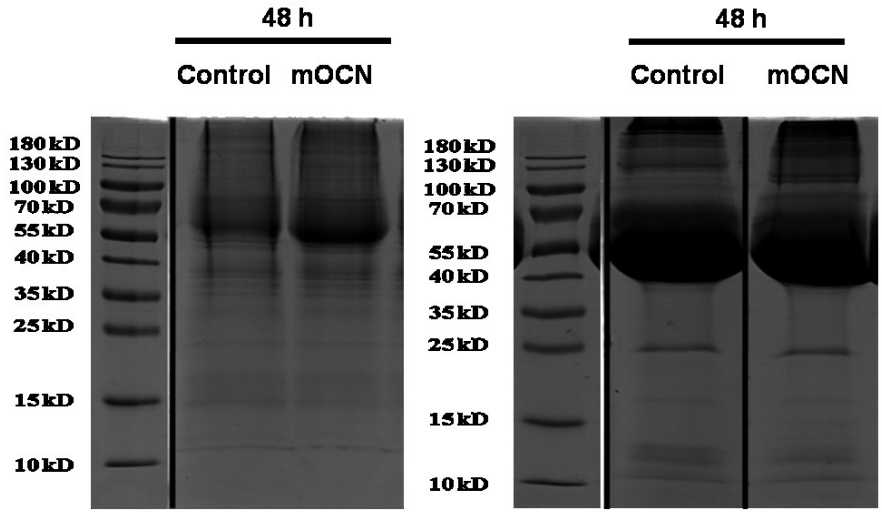

Figure 46. Protein expression analysis of mOCN in HEK293 cells by SDS-PAGE. Image 1. Cell lysate. Lane 1: Page Ruler Ladder (NEB), Lane 2: Untransfected cells. Lane 3: mOCN transfected cells after 48 h culture with plasmid. **Image 2.** Cell culture supernatant. Lane 1: Page Ruler Ladder (NEB), Lane 2: Control cells without transfection cultured in the presence of osteogenic medium for 48 h, Lane 3: mOCN transfected cells after 48 h culture with plasmid.

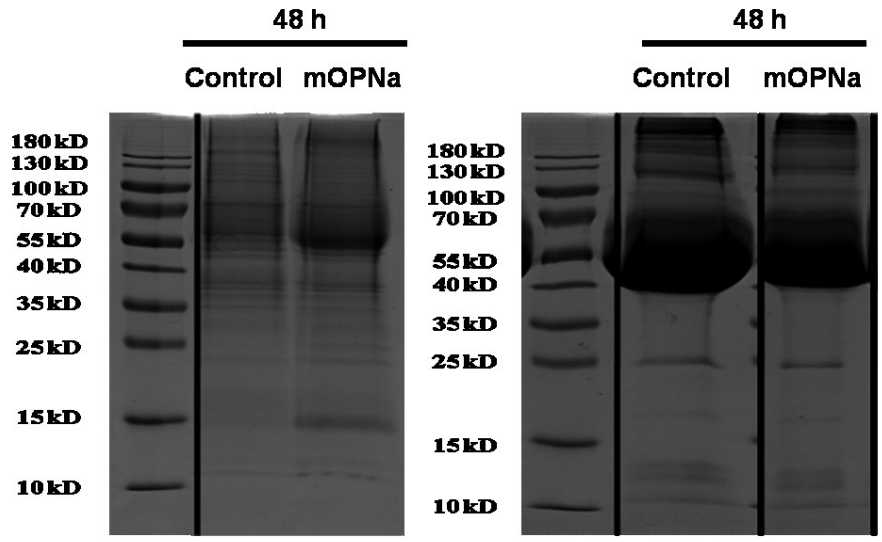

Figure 47. Protein expression analysis of mOPNa in HEK293 cells by SDS-PAGE. Image 1. Cell lysate. Lane 1: Page Ruler Ladder (NEB), Lane 2: Untransfected cells. Lane 3: mOPNa transfected cells after 48 h culture with plasmid. **Image 2.** Cell culture supernatant. Lane 1: Page Ruler Ladder (NEB), Lane 2: Control cells without transfection cultured in the presence of osteogenic medium for 48 h, Lane 3: mOPNa transfected cells after 48 h culture with plasmid.

4.3.2.3 Detection of OCN and OPN expression by Western Blotting

In order to understand if the proteins are expressed or not, Western blot analysis was also performed. But, no expression detected. It was not expected, since qRT-PCR results showed that the mRNAs were expressed. However, proteins cannot be detected by both SDS-PAGE and Western blot analysis. (Figure 47-49)

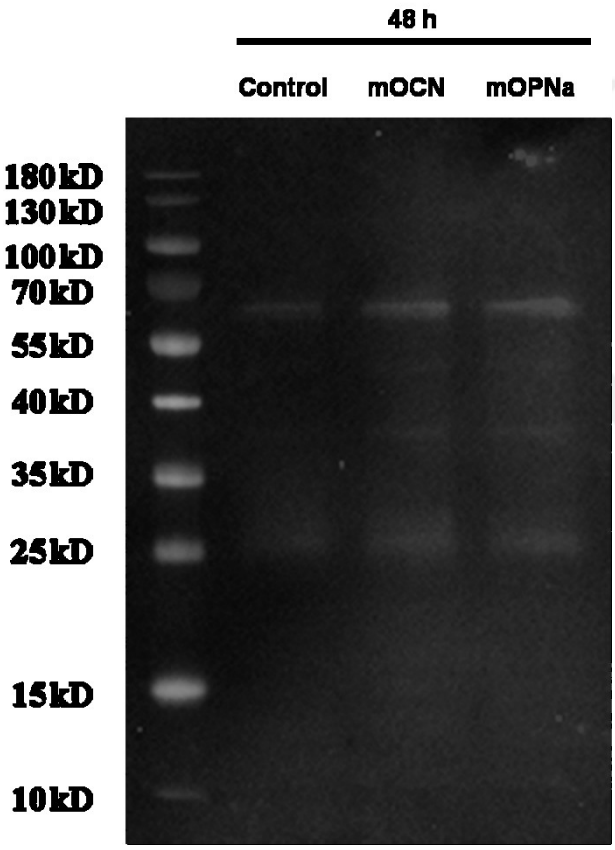

Figure 48. Protein expression analysis of mOPNa in HEK293 cells by Western Blotting. Cell lysate. Lane 1: Page Ruler Ladder (NEB), . Lane 2: Control cells without transfection cultured in the presence of osteogenic medium. Lane 3: mOCN transfected cells, Lane 3: mOPNa transfected cells. Western Blot analysis was performed 48 h after transfection.

4.3.2.4 Detection of OCN and OPN expression by immunostaining

Since gene expression analysis by Western Blot was not successful, immunostaining was performed to detect gene expression after transfection. Expression of mOCN and mOPNa genes was detected by ICC by using antibody against His-tag sequence. (Figure 50)

I have tried to differentiate HEK293 cells into mineral forming cell type. I transformed mOCN and mOPNa plasmids into HEK293 cells, after 48 hours, I added osteogenic differentiation medium on transfected cells. Osteogenic medium changed every 3-4 days for 21 days. However, I could not see mineral deposition. I concluded that presence of single osteogenic gene expression is not enough for mineral formation. Presence of a hydroxyapatite scaffold, and/or overexpression of ALP gene could be necessary for mineral deposition. Another strategy could be the addition of chemicals to increase epigenetic plasticity into the experimental setup such as 5-aza cytidine, which inhibits DNA methylation and change epigenetic characteristics of cells. (Harland, Day et al. 2014)

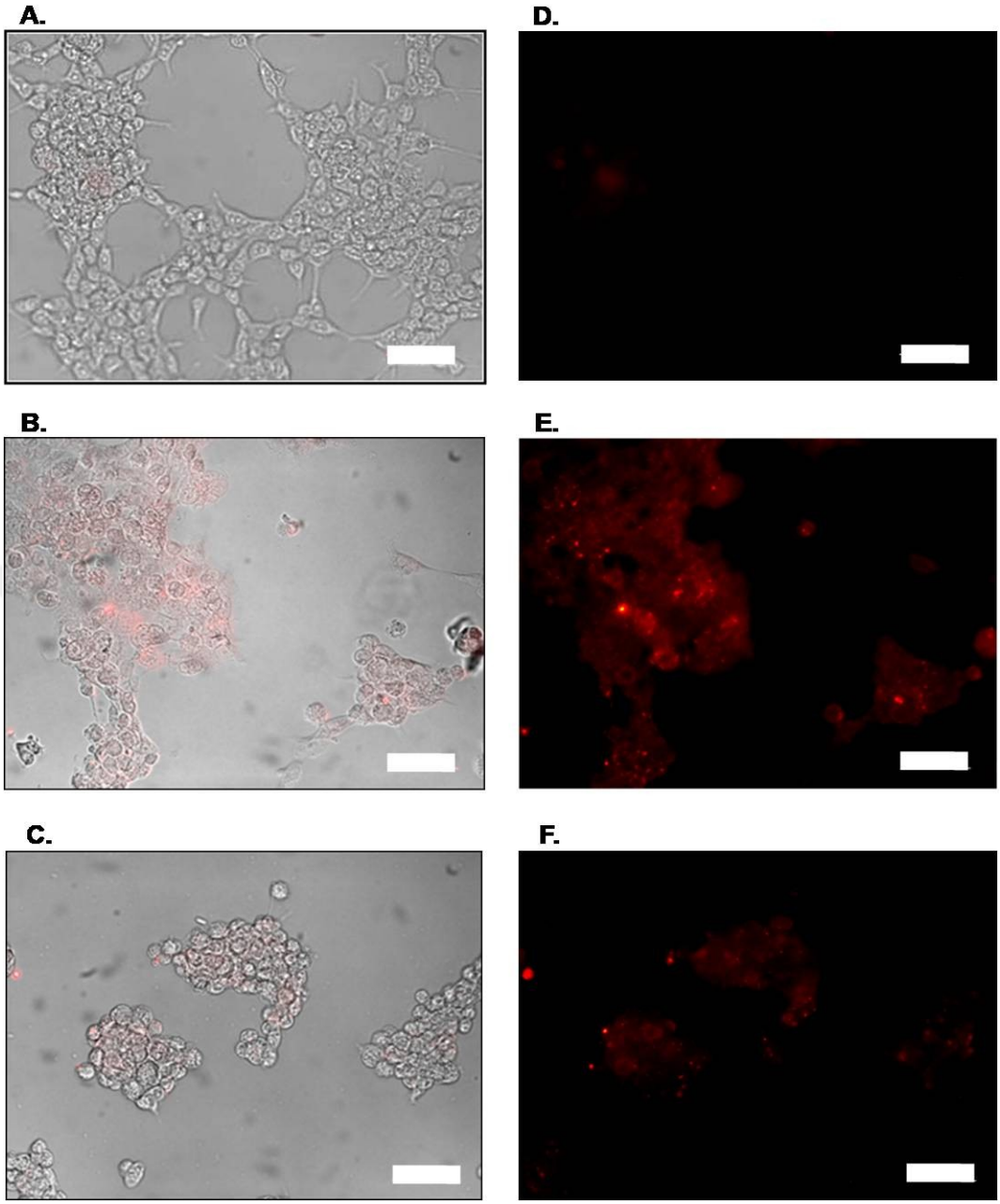

Figure 49. Protein expression analysis of mOCN and mOPNa in HEK293 cells by ICC. A,D. Untransfected HEK293 cells. B,E. mOCN transfected HEK 293 cells. C,F. mOPNa transfected HEK 293 cells. His Tag Monoclonal Antibody (HIS.H8) was used in 1:300 dilution in 5% milk powder in 1X PBS as primary antibody. Pierce Goat anti-Mouse IgG (H+L) Cross Adsorbed Secondary Antibody, DyLight 550 was used in 1:600 dilution in 5% milk powder in 1X PBS as secondary antibody. Images were taken fluorescent microscope. A-C. Overlay of brightfield and fluorescent images. D-F. Fluorescent staining images. Scalebars represents 50 µm.

5 CHAPTER IV

5.1 CONCLUSION

Biomimetic ECM scaffolds are the most promising candidates for bone tissue engineering applications. Synthetic bone scaffolds are generated by combination of inorganic matrix, bone ECM proteins or bone ECM protein-like peptides, and mesenchymal stem cells or pre-osteoblast cells. While generating these scaffolds, several routes can be used. The important parameters includes formation of an inorganic matrix with defined Ca/P ratio, size and shape, using accurate concentrations of proteins and peptides to control mineralization event, and existence of a cell type which can produce bone type minerals continuously or which can differentiate into mineral forming cells. The inorganic matrix should truly mimic bone tissue when it is produced *in vitro*. To do this, an environmentally friendly biomineralization system was constructed in ambient conditions in this study, which is composed of ALP, and recombinant bone ECM proteins, OCN and OPN. While ALP produces inorganic phosphate ions required for biomineralization, OCN and OPN controls size, shape and Ca/P ratio of the minerals, control crystal growth rate and inhibit excessive mineralization.

ALP from *E. coli* was produced in this system owing to the structural homology and functional overlap with human ALP. ALP was successfully lead CaP crystal formation in a reaction which is composed of organic phosphate and calcium at physiological pH and temperature. Recombinant OCN and OPN proteins were produced and purified in our system in order to understand effect of each bone ECM

proteins on CaP crystals formed in the presence of ALP. OCN was found to become more compact upon interaction with calcium, but its secondary structure was disrupted upon interaction with inorganic phosphate. The order of interaction of OCN with calcium or phosphate changed the behavior of OCN in terms of controlling biomineralization of CaP crystals. OCN-calcium interaction made the biomineralization event slower, reduced the reaction rate and reduced the crystal size. OCN-inorganic phosphate interaction hindered all the effects of OCN, due to the changes in the structure upon interaction. OPN was a largely disordered protein, but the compact structures occur because of the absence of phosphorylation in our system. The interaction of OPN with inorganic phosphate causes aggregation of OPN, and the aggregation makes CaP crystal formation faster. The interaction of OPN with calcium hindered the effect of OPN, reaction was not faster anymore. This was probably due to the disruption of OPN aggregates. OPN-calcium interaction had no effect on secondary structure, but this interaction could be preventing OPN-inorganic phosphate interaction. In addition, Ca/P ratio was reduced when OPN is present in biomineralization reaction. The effect of OPN on Ca/P ratio was compensated by the presence of OCN, when OCN and OPN was used in a singal reaction. Moreover, the presence of OCN and OPN proteins in reaction causes a decrease on ALP activity since they both can bind organic phosphate source and compete with ALP in binding. Further analysis is needed to understand the molecular mechanisms behind the interaction of bone ECM proteins with inorganic matrix and small ions. Differentiation of osteoblast precursors can be tuned by the crystal characteristics of the minerals which were formed in our system. Engineering mammalian or bacterial cells for production and secretion of OCN and OPN proteins

has great potential to control biomineralization events and produce bone-tissue mimetic scaffolds for biomedical applications.

Moreover, an engineered mammalian cell line was generated in this study in order to achieve differentiation free bone mineral formation in a somatic cell line. We observed that OCN and OPN are not enough to achieve this goal, expression of ALP, use of an inorganic matrix, and induction of epigenetic plasticity could also be necessary. Reprogramming of cells will provide the production of CaP crystals required for bone tissue repair to aid fracture healing. By means of engineered cells, bone marrow stromal cells can be replaced with somatic cells in cell-based scaffolds and aspiration of bone marrow can be eliminated, which is a painful procedure. The results of this study will lead to engineering effective cell-based scaffolds in bone tissue regeneration. The engineering approach can yield in engineering implantable designer cells with genetic cellular devices for biomineralization to be used in regenerative medicine applications.

5.2 BIBLIOGRAPHY

(2019/07/15/08:07:24). "Biochemical aspects of biomineralization | SpringerLink." from https://link.springer.com/chapter/10.1007/BFb0048192.

(2019/07/24/11:45:30). "Cytoplasmic inclusion bodies in Escherichia coli producing biosynthetic human insulin proteins | Science." from https://science.sciencemag.org/content/215/4533/687.

(2019/07/24/11:45:24). "Human insulin from recombinant DNA technology | Science." from https://science.sciencemag.org/content/219/4585/632.abstract.

Abbarin, N., S. San Miguel, et al. (2014). "The Enamel Protein Amelotin Is a Promoter of Hydroxyapatite Mineralization." Journal of Bone and Mineral Research **30**(5): 775-785.

Ai-Aql, Z. S., A. S. Alagl, et al. (2008). "Molecular Mechanisms Controlling Bone Formation during Fracture Healing and Distraction Osteogenesis." Journal of Dental Research **87**(2): 107-118.

Alves, R. D. A. M., M. Eijken, et al. (2014). "Calcifying vascular smooth muscle cells and osteoblasts: independent cell types exhibiting extracellular matrix and biomineralization-related mimicries." BMC Genomics **15**(1): 965.

Baneyx, F. (1999). "Recombinant protein expression in Escherichia coli." Current Opinion in Biotechnology **10**(5): 411-421.

Birkedal, H. (2017). Phase Transformations in Calcium Phosphate Crystallization. New Perspectives on Mineral Nucleation and Growth: From Solution Precursors to Solid Materials. A. E. S. Van Driessche, M. Kellermeier, L. G. Benning and D. Gebauer. Cham, Springer International Publishing**:** 199-210.

Borja, G. M., E. Meza Mora, et al. (2012). "Engineering Escherichia coli to increase plasmid DNA production in high cell-density cultivations in batch mode." Microbial Cell Factories **11**: 132.

Cai, Y., D. Mei, et al. (2010). "Synthesis of oriented hydroxyapatite crystals: Effect of reaction conditions in the presence or absence of silk sericin." Materials Letters **64**(24): 2676-2678.

Choi, J. H., K. C. Keum, et al. (2006). "Production of recombinant proteins by high cell density culture of Escherichia coli." Chemical Engineering Science **61**(3): 876-885.

Choi, J. H. and S. Y. Lee (2004). "Secretory and extracellular production of recombinant proteins using Escherichia coli." Applied Microbiology and Biotechnology **64**(5): 625-635.

Crichton, R. R. (2012). Chapter 19 - Biomineralisation. Biological Inorganic Chemistry (Second Edition). R. R. Crichton. Oxford, Elsevier**:** 359-378.

D'Souza, R. N., A. Cavender, et al. (1997). "Gene expression patterns of murine dentin matrix protein 1 (Dmp1) and dentin sialophosphoprotein (DSPP) suggest distinct developmental functions in vivo." Journal of Bone and Mineral Research **12**(12): 2040-2049.

Denhardt, D. T. and X. Guo (1993). "Osteopontin: a protein with diverse functions." The FASEB Journal **7**(15): 1475-1482.

Dowd, T. L., J. F. Rosen, et al. (2001). "The effect of Pb2+ on the structure and hydroxyapatite binding properties of osteocalcin." Biochimica et Biophysica Acta (BBA) - Molecular Basis of Disease **1535**(2): 153-163.

Ducy, P., C. Desbois, et al. (1996). "Increased bone formation in osteocalcin-deficient mice." Nature **382**: 448.

Edwards, C. C., S. C. Simmons, et al. (1988). "Severe open tibial fractures. Results treating 202 injuries with external fixation." Clinical Orthopaedics and Related Research(230): 98-115.

Gajjeraman, S., K. Narayanan, et al. (2007). "Matrix macromolecules in hard tissues control the nucleation and hierarchical assembly of hydroxyapatite." Journal of Biological Chemistry **282**(2): 1193-1204.

Galperin, M. Y. and M. J. Jedrzejas (2001). "Conserved core structure and active site residues in alkaline phosphatase superfamily enzymes." Proteins: Structure, Function, and Bioinformatics **45**(4): 318-324.

Gehron Robey, P. (2008). Chapter 17 - Noncollagenous Bone Matrix Proteins. Principles of Bone Biology (Third Edition). J. P. Bilezikian, L. G. Raisz and T. J. Martin. San Diego, Academic Press**:** 335-349.

Gericke, A., C. Qin, et al. (2005). "Importance of Phosphorylation for Osteopontin Regulation of Biomineralization." Calcified Tissue International **77**(1): 45-54.

Gibson, D. G., L. Young, et al. (2009). "Enzymatic assembly of DNA molecules up to several hundred kilobases." Nature Methods **6**: 343.

Golub, E. E. (2009). "Role of matrix vesicles in biomineralization." Biochimica et biophysica acta **1790**(12): 1592-1598.

Gorski, J. P., E. Kremer, et al. (1995). "Conformational Analyses on Soluble and Surface Bound Osteopontin." Annals of the New York Academy of Sciences **760**(1): 12-23.

Greenwald, A. S., S. D. Boden, et al. (2001). "Bone-graft substitutes: facts, fictions, and applications." J Bone Joint Surg Am **83-A Suppl 2 Pt 2**: 98-103.

Gregory, C. A., W. Grady Gunn, et al. (2004). "An Alizarin red-based assay of mineralization by adherent cells in culture: comparison with cetylpyridinium chloride extraction." Analytical Biochemistry **329**(1): 77-84.

Guan, K. and J. E. Dixon (1991). "Eukaryotic proteins expressed in Escherichia coli: An improved thrombin cleavage and purification procedure of fusion proteins with glutathione S-transferase." Analytical Biochemistry **192**(2): 262-267.

Gungormus, M., H. Fong, et al. (2008). "Regulation of in vitro Calcium Phosphate Mineralization by Combinatorially Selected Hydroxyapatite-Binding Peptides." Biomacromolecules **9**(3): 966-973.

Halford, S. E., M. J. Schlesinger, et al. (1972). "Escherichia coli alkaline phosphatase. Kinetic studies with the tetrameric enzyme." Biochemical Journal **126**(5): 1081-1090.

Harland, K. L., E. B. Day, et al. (2014). "Epigenetic plasticity of Cd8a locus during CD8⁺ T-cell development and effector differentiation and reprogramming." Nature Communications **5**: 3547.

Hauschka, P. V. and S. A. Carr (1982). "Calcium-dependent .alpha.-helical structure in osteocalcin." Biochemistry **21**(10): 2538-2547.

Hauschka, P. V. and F. H. Wians Jr (1989). "Osteocalcin-hydroxyapatite interaction in the extracellular organic matrix of bone." The Anatomical Record **224**(2): 180-188.

He, G., T. Dahl, et al. (2003). "Nucleation of apatite crystals in vitro by self-assembled dentin matrix protein 1." Nat Mater **2**(8): 552-558.
Heise, U., J. F. Osborn, et al. (1990). "Hydroxyapatite ceramic as a bone substitute." International Orthopaedics **14**(3): 329-338.
Herries, D. G. (1981). "Alkaline phosphatase: by R B McComb, G N Bowers, Jr and S Posen. pp 986. Plenum Press, New York and London. 1979. $75 ISBN 0-306-40214-9." Biochemical Education **9**(2): 76.
https://benchling.com/editor. (2019/07/24/13:15:50). "Editor · Benchling." from https://benchling.com/editor.
Hunter, G. K. (2013). "Role of Osteopontin in Modulation of Hydroxyapatite Formation." Calcified Tissue International **93**(4): 348-354.
Hunter, G. K., J. O'Young, et al. (2010). "The Flexible Polyelectrolyte Hypothesis of Protein−Biomineral Interaction." Langmuir **26**(24): 18639-18646.
Ibsen, C. J. S., D. Gebauer, et al. (2016). "Osteopontin Stabilizes Metastable States Prior to Nucleation during Apatite Formation." Chemistry of Materials **28**(23): 8550-8555.
Isbell, D. T., S. Du, et al. (1993). "Metal ion binding to dog osteocalcin studied by 1H NMR spectroscopy." Biochemistry **32**(42): 11352-11362.
Jemal, A., R. Siegel, et al. (2008). "Cancer statistics, 2008." CA Cancer J Clin **58**(2): 71-96.
Jeong, H., V. Barbe, et al. (2009). "Genome Sequences of Escherichia coli B strains REL606 and BL21(DE3)." Journal of Molecular Biology **394**(4): 644-652.
Johnson, K. A. and R. S. Goody (2011). "The Original Michaelis Constant: Translation of the 1913 Michaelis–Menten Paper." Biochemistry **50**(39): 8264-8269.
Kaartinen, M. T., A. Pirhonen, et al. (1999). "Cross-linking of Osteopontin by Tissue Transglutaminase Increases Its Collagen Binding Properties." Journal of Biological Chemistry **274**(3): 1729-1735.
Käkönen, S.-M., J. Hellman, et al. (1996). "Purification and Characterization of Recombinant Osteocalcin Fusion Protein Expressed inEscherichia coli." Protein Expression and Purification **8**(2): 137-144.
Kazanecki, C. C., D. J. Uzwiak, et al. (2007). "Control of osteopontin signaling and function by post-translational phosphorylation and protein folding." Journal of Cellular Biochemistry **102**(4): 912-924.
Keen, H., J. C. Pickup, et al. (1980). "HUMAN INSULIN PRODUCED BY RECOMBINANT DNA TECHNOLOGY: SAFETY AND HYPOGLYCÆMIC POTENCY IN HEALTHY MEN." The Lancet **316**(8191): 398-401.
Kikuchi, M., T. Ikoma, et al. (2004). "Biomimetic synthesis of bone-like nanocomposites using the self-organization mechanism of hydroxyapatite and collagen." Composites Science and Technology **64**(6): 819-825.
Kirkham, J., S. J. Brookes, et al. (2002). "Physico-chemical properties of crystal surfaces in matrix–mineral interactions during mammalian biomineralisation." Current Opinion in Colloid & Interface Science **7**(1): 124-132.
Landi, E., G. Celotti, et al. (2003). "Carbonated hydroxyapatite as bone substitute." Journal of the European Ceramic Society **23**(15): 2931-2937.
Lee-Huang, S. (1984). "Cloning and expression of human erythropoietin cDNA in Escherichia coli." Proceedings of the National Academy of Sciences **81**(9): 2708-2712.

Lee, S. Y., S. Y. Kim, et al. (2012). "Effects of recombinant dentin sialoprotein in dental pulp cells." J Dent Res **91**(4): 407-412.
Li, Z., L. Yubao, et al. (2005). "Preparation and in vitro investigation of chitosan/nano-hydroxyapatite composite used as bone substitute materials." Journal of Materials Science: Materials in Medicine **16**(3): 213-219.
Liu, Y., D. Luo, et al. (2016). "Hierarchical Structures of Bone and Bioinspired Bone Tissue Engineering." Small **12**(34): 4611-4632.
Lu, H. B., C. T. Campbell, et al. (2000). "Surface characterization of hydroxyapatite and related calcium phosphates by XPS and TOF-SIMS." Anal Chem **72**(13): 2886-2894.
Micsonai, A., F. Wien, et al. (2015). "Accurate secondary structure prediction and fold recognition for circular dichroism spectroscopy." Proceedings of the National Academy of Sciences **112**(24): E3095-E3103.
Narayanan, K., R. Srinivas, et al. (2001). "Differentiation of embryonic mesenchymal cells to odontoblast-like cells by overexpression of dentin matrix protein 1." Proceedings of the National Academy of Sciences **98**(8): 4516-4521.
O'Neill, E., G. Awale, et al. (2018). "The roles of ions on bone regeneration." Drug Discovery Today **23**(4): 879-890.
Ohri, R., E. Tung, et al. (2005). "Mitigation of Ectopic Calcification in Osteopontin-Deficient Mice by Exogenous Osteopontin." Calcified Tissue International **76**(4): 307-315.
Plotkin, J. B. and G. Kudla (2010). "Synonymous but not the same: the causes and consequences of codon bias." Nature Reviews Genetics **12**: 32.
Prince, C. W., T. Oosawa, et al. (1987). "Isolation, characterization, and biosynthesis of a phosphorylated glycoprotein from rat bone." Journal of Biological Chemistry **262**(6): 2900-2907.
Puzas, J. E., M. D. Miller, et al. (1989). "Pathologic bone formation." Clinical Orthopaedics and Related Research(245): 269-281.
Riggs, B. L. and L. J. Melton (1986). "Involutional Osteoporosis." New England Journal of Medicine **314**(26): 1676-1686.
Romberg, R. W., P. G. Werness, et al. (1986). "Inhibition of hydroxyapatite-crystal growth by bone-specific and other calcium-binding proteins." Biochemistry **25**(5): 1176-1180.
Sadat-Shojai, M., M. T. Khorasani, et al. (2013). "Synthesis methods for nanosized hydroxyapatite with diverse structures." Acta Biomater **9**(8): 7591-7621.
Sampath, T. K., J. C. Maliakal, et al. (1992). "Recombinant human osteogenic protein-1 (hOP-1) induces new bone formation in vivo with a specific activity comparable with natural bovine osteogenic protein and stimulates osteoblast proliferation and differentiation in vitro." Journal of Biological Chemistry **267**(28): 20352-20362.
Sanchez-Garcia, L., L. Martín, et al. (2016). "Recombinant pharmaceuticals from microbial cells: a 2015 update." Microbial Cell Factories **15**(1): 33.
Shin, N.-K., D.-Y. Kim, et al. (1998). "High-level production of human growth hormone in Escherichia coli by a simple recombinant process." Journal of Biotechnology **62**(2): 143-151.
Siller Alejandro, F. and P. Whyte Michael (2017). "Alkaline Phosphatase: Discovery and Naming of Our Favorite Enzyme." Journal of Bone and Mineral Research **33**(2): 362-364.

Singer, A., M. A. Eiteman, et al. (2009). "DNA plasmid production in different host strains of Escherichia coli." Journal of Industrial Microbiology & Biotechnology **36**(4): 521-530.
Singh, P., L. Sharma, et al. (2013). "Effect of signal peptide on stability and folding of Escherichia coli thioredoxin." PLoS One **8**(5): e63442-e63442.
Smith, L. L., H. K. Cheung, et al. (1996). "Osteopontin N-terminal domain contains a cryptic adhesive sequence recognized by alpha9beta1 integrin." Journal of Biological Chemistry **271**(45): 28485-28491.
Sørensen, H. P. and K. K. Mortensen (2005). "Advanced genetic strategies for recombinant protein expression in Escherichia coli." Journal of Biotechnology **115**(2): 113-128.
Structural Genomics, C., B. Architecture et Fonction des Macromolécules, et al. (2008). "Protein production and purification." Nature Methods **5**: 135.
Svensson Bonde, J. and L. Bulow (2012). "One-Step Purification of Recombinant Human Amelogenin and Use of Amelogenin as a Fusion Partner." PLoS One **7**(3): e33269.
Swartz, J. R. (2001). "Advances in Escherichia coli production of therapeutic proteins." Current Opinion in Biotechnology **12**(2): 195-201.
Takahashi, K. and S. Yamanaka (2006). "Induction of Pluripotent Stem Cells from Mouse Embryonic and Adult Fibroblast Cultures by Defined Factors." Cell **126**(4): 663-676.
Tan, S., W. Wu, et al. (2002). "Efficient expression and secretion of recombinant hirudin III in E. coli using the l-asparaginase II signal sequence." Protein Expression and Purification **25**(3): 430-436.
Tartaix, P. H., M. Doulaverakis, et al. (2004). "In Vitro Effects of Dentin Matrix Protein-1 on Hydroxyapatite Formation Provide Insights into in Vivo Functions." Journal of Biological Chemistry **279**(18): 18115-18120.
Teotia, A. K., D. B. Raina, et al. (2017). "Nano-Hydroxyapatite Bone Substitute Functionalized with Bone Active Molecules for Enhanced Cranial Bone Regeneration." ACS Applied Materials & Interfaces **9**(8): 6816-6828.
Trope, M. (2008). "Regenerative potential of dental pulp." J Endod **34**(7 Suppl): S13-17.
Tsao, Y.-T., Y.-J. Huang, et al. (2017). "Osteocalcin Mediates Biomineralization during Osteogenic Maturation in Human Mesenchymal Stromal Cells." International Journal of Molecular Sciences **18**(1).
Wang, L., X. Guan, et al. (2007). "Amelogenin Promotes the Formation of Elongated Apatite Microstructures in a Controlled Crystallization System." The Journal of Physical Chemistry C **111**(17): 6398-6404.
Wang, L., X. Guan, et al. (2008). "Phosphorylation of Osteopontin Is Required for Inhibition of Calcium Oxalate Crystallization." The Journal of Physical Chemistry B **112**(30): 9151-9157.
Wang, L. and G. H. Nancollas (2008). "Calcium Orthophosphates: Crystallization and Dissolution." Chemical Reviews **108**(11): 4628-4669.
Wians, F. H., K. E. Krech, et al. (1983). "Effects of magnesium and calcium on osteocalcin adsorption to hydroxyapatite." Magnesium **2**: 83-92.
Wittneben, J. G., D. Buser, et al. (2014). "Complication and failure rates with implant-supported fixed dental prostheses and single crowns: a 10-year retrospective study." Clin Implant Dent Relat Res **16**(3): 356-364.

Xiong, S. H., L. Yu, et al. (2002). "Expression and purification of recombinant bone morphogenetic protein-2 in E.coli." Di Yi Jun Yi Da Xue Xue Bao **22**(5): 413-416.

Yang, S., H. He, et al. (2011). "Oriented crystallization of hydroxyapatite by the biomimetic amelogenin nanospheres from self-assemblies of amphiphilic dendrons." Chemical Communications **47**(36): 10100-10102.

Yun, Y. R., H. W. Kim, et al. (2012). "Expression and purification recombinant human dentin sialoprotein in Escherichia coli and its effects on human dental pulp cells." Protein Expr Purif **83**(1): 47-51.

Zhang, H., L. Yang, et al. (2018). "The pH-dependent activation mechanism of Ser102 in Escherichia coli alkaline phosphatase: a theoretical study." JBIC Journal of Biological Inorganic Chemistry **23**(2): 277-284.

5.3 APPENDIX A

5.3.1 DNA sequences of genes and gene fragments

Table A1. Nucleotide sequences of phoA, GST-OCN, OCN and OPN genes.

E. coli phoA gene nucleotide sequence with pelB, 6X His-Tag and GS Linker	ATGAAATACCTGCTGCCGACCGCTGCTGCTG GTCTGCTGCTCCTCGCTGCCCAGCCGGCGAT GGCCATGGGCCACCACCACCACCACCACGGT GGCGGTGGATCCCGGACACCAGAAATGCCTG TTCTGGAAAACCGGGCTGCTCAGGGCGATAT TACTGCACCCGGCGGTGCTCGCCGTTTAACG GGTGATCAGACTGCCGCTCTGCGTGATTCTCT TAGCGATAAACCTGCAAAAAATATTATTTTG CTGATTGGCGATGGGATGGGGGACTCGGAAA TTACTGCCGCACGTAATTATGCCGAAGGTGC GGGCGGCTTTTTTAAAGGTATAGATGCCTTA CCGCTTACCGGGCAATACACTCACTATGCGC TGAATAAAAAAACCGGCAAACCGGACTACG TCACCGACTCGGCTGCATCAGCAACCGCCTG GTCAACCGGTGTCAAAACCTATAACGGCGCG CTGGGCGTCGATATTCACGAAAAAGATCACC CAACGATTCTGGAAATGGCAAAAGCCGCAG GTCTGGCGACCGGTAACGTTTCTACCGCAGA

Table A1. (cont'd)

	GTTGCAGGATGCCACGCCCGCTGCGCTGGTG
	GCACATGTGACCTCGCGCAAATGCTACGGTC
	CGAGCGCGACCAGTGAAAAATGTCCGGGTA
	ACGCTCTGGAAAAAGGCGGAAAAGGATCGA
	TTACCGAACAGCTGCTTAACGCTCGTGCCGA
	CGTTACGCTTGGCGGCGGCGCAAAAACCTTT
	GCTGAAACGGCAACCGCTGGTGAATGGCAG
	GGAAAAACGCTGCGTGAACAGGCACAGGCG
	CGTGGTTATCAGTTGGTGAGCGATGCTGCCT
	CACTGAATTCGGTGACGGAAGCGAATCAGCA
	AAAACCCCTGCTTGGCCTGTTTGCTGACGGC
	AATATGCCAGTGCGCTGGCTAGGACCGAAAG
	CAACGTACCATGGCAATATCGATAAGCCCGC
	AGTCACCTGTACGCCAAATCCGCAACGTAAT
	GACAGTGTACCAACCCTGGCGCAGATGACCG
	ACAAAGCCATTGAATTGTTGAGTAAAAATGA
	GAAAGGCTTTTTCCTGCAAGTTGAAGGTGCG
	TCAATCGATAAACAGGATCATGCTGCGAATC
	CTTGTGGGCAAATTGGCGAGACGGTCGATCT
	CGATGAAGCCGTACAACGGGCGCTGGAATTC
	GCTAAAAAGGAGGGTAACACGCTGGTCATA
	GTCACCGCTGATCACGCCCACGCCAGCCAGA
	TTGTTGCGCCGGATACCAAAGCTCCGGGCCT
	CACCCAGGCGCTAAATACCAAAGATGGCGCA

Table A1. (cont'd)

	GTGATGGTGATGAGTTACGGGAACTCCGAAG AGGATTCACAAGAACATACCGGCAGTCAGTT GCGTATTGCGGCGTATGGCCCGCATGCCGCC AATGTTGTTGGACTGACCGACCAGACCGATC TCTTCTACACCATGAAAGCCGCTCTGGGGCT GAAATGATGA
Synthetic GST-TEV-OCN-6X His-Tag nucleotide sequence (https://eu.idtdna.com/CodonOpt)	ATGTCCCCTATACTAGGTTATTGGAAAATTA AGGGCCTTGTGCAACCCACTCGACTTCTTTTG GAATATCTTGAAGAAAAATATGAAGAGCATT TGTATGAGCGCGATGAAGGTGATAAATGGCG AAACAAAAAGTTTGAATTGGGTTTGGAGTTT CCCAATCTTCCTTATTATATTGATGGTGATGT TAAATTAACACAGTCTATGGCCATCATACGT TATATAGCTGACAAGCACAACATGTTGGGTG GTTGTCCAAAAGAGCGTGCAGAGATTTCAAT GCTTGAAGGAGCGGTTTTGGATATTAGATAC GGTGTTTCGAGAATTGCATATAGTAAAGACT TTGAAACTCTCAAAGTTGATTTTCTTAGCAAG CTACCTGAAATGCTGAAAATGTTCGAAGATC GTTTATGTCATAAAACATATTTAAATGGTGA TCATGTAACCCATCCTGACTTCATGTTGTATG ACGCTCTTGATGTTGTTTTATACATGGACCCA ATGTGCCTGGATGCGTTCCCAAAATTAGTTT GTTTTAAAAAACGTATTGAAGCTATCCCACA

Table A1. (cont'd)

	AATTGATAAGTACTTGAAATCCAGCAAGTAT ATAGCATGGCCTTTGCAGGGCTGGCAAGCCA CGTTTGGTGGTGGCGACCATCCTCCAAAATC GGATCTGGAAGTTCTGTTCCAGGGGCCCCTG GGATCCGAAAACCTGTATTTTCAGGGCATGA AACCGTCTGGCGCAGAAAGCTCTAAGGGTGC GGCCTTCGTTTCAAAACAGGAAGGCTCGGAA GTGGTTAAACGTCCGCGTCGCTATCTGTACC AATGGCTGGGTGCCCCGGTTCCGTATCCGGA CCCGCTGGAACCGCGTCGCGAAGTCTGCGAA CTGAACCCGGATTGTGACGAACTGGCGGACC ATATTGGTTTTCAGGAAGCCTATCGTCGCTTC TACGGCCCGGTCCACCACCACCATCATCATG AATTCCCGGGTCGACTCGAGCGGCCGCATCG TGACTGA
Synthetic OCN nucleotide sequence without secretion signal sequence, with 6X His-Tag sequence and codon optimized to *E. coli* by online tool (https://eu.idtdna.com/CodonOpt)	ATGAAACCGTCTGGCGCAGAAAGCTCTAAGG GTGCGGCCTTCGTTTCAAAACAGGAAGGCTC GGAAGTGGTTAAACGTCCGCGTCGCTATCTG TACCAATGGCTGGGTGCCCCGGTTCCGTATC CGGACCCGCTGGAACCGCGTCGCGAAGTCTG CGAACTGAACCCGGATTGTGACGAACTGGCG GACCATATTGGTTTTCAGGAAGCCTATCGTC GCTTCTACGGCCCGGTCCACCACCACCATCA TCAT

Table A1. (cont'd)

Synthetic OPN nucleotide sequence without secretion signal sequence, with 6X His-Tag sequence and codon optimized to *E. coli* by online tool (https://eu.idtdna.com/CodonOpt)	ATGATTCCGGTTAAACAGGCAGATAGCGGCA GCTCTGAAGAAAAACAACTGTACAACAAATA CCCGGATGCAGTGGCTACCTGGCTGAACCCG GACCCGTCGCAGAAACAAAATCTGCTGGCTC CGCAGACCCTGCCGAGCAAATCTAACGAATC TCATGATCACATGGATGACATGGATGACGAA GATGACGATGACCATGTCGATTCACAGGACT CGATCGATAGCAATGACTCTGATGACGTTGA TGACACCGATGACAGTCACCAATCCGATGAA TCACATCACTCGGATGAAAGCGACGAACTGG TGACCGATTTTCCGACGGACCTGCCGGCCAC CGAAGTTTTCACGCCGGTGGTTCCGACCGTC GATACGTATGACGGCCGTGGTGATTCCGTCG TGTACGGTCTGCGCAGTAAATCCAAAAAATT TCGTCGCCCGGATATTCAGTATCCGGACGCG ACCGATGAAGACATCACGTCCCACATGGAAT CAGAAGAACTGAACGGCGCGTACAAAGCCA TTCCGGTTGCACAGGATCTGAATGCTCCGTC GGATTGGGACAGCCGTGGTAAAGATTCTTAT GAAACCAGTCAGCTGGATGACCAATCTGCGG AAACGCATTCCCACAAACAGTCACGTCTGTA CAAACGCAAAGCCAACGATGAATCGAATGA ACATAGCGATGTGATTGACAGTCAAGAACTG TCTAAAGTTAGTCGTGAATTTCATTCTCACGA

Table A1. (cont'd)

	ATTTCATAGTCACGAAGATATGCTGGTTGTC GACCCGAAAAGCAAAGAAGAAGATAAACAT CTGAAATTCCGCATCTCCCACGAACTGGATT CAGCGAGTTCCGAAGTGAATCTCGAGCACCA CCACCACCACCACTGAG

Table A2. Nucleotide sequences of cDNAs.

mOCN cDNA sequence with Kozak sequence, GS linker, 4x-His tag, stop codon	TACTTCCAATCCAATGCCACCGGTACC ATGAGGACCCTCTCTCTGCTCACTCTGCTGG CCCTGGCTGCGCTCTGTCTCTCTGACCTCACA GATGCCAAGCCCAGCGGCCCTGAGTCTGACA AAGCCTTCATGTCCAAGCAGGAGGGCAATA AGGTAGTGAACAGACTCCGGCGCTACCTTGG AGCCTCAGTCCCCAGCCCAGATCCCCTGGAG CCCACCCGGGAGCAGTGTGAGCTTAACCCTG CTTGTGACGAGCTATCAGACCAGTATGGCTT GAAGACCGCCTACAAACGCATCTACGGTATC ACTATTGAATTCCTTAAGGGCGGTAGCGGTC ACCATCACCATTAA

Table A2. (cont'd)

mOPNa cDNA sequence with Kozak sequence, GS linker, 4x-His tag, stop codon	TACTTCCAATCCAATGCCACCGGTACCATGA GATTGGCAGTGATTTGCTTTTGCCTGTTTGGC ATTGCCTCCTCCCTCCCGGTGAAAGTGACTG ATTCTGGCAGCTCAGAGGAGAAGAAGCTTTA CAGCCTGCACCCAGATCCTATAGCCACATGG CTGGTGCCTGACCCATCTCAGAAGCAGAATC TCCTTGCGCCACAGAATGCTGTGTCCTCTGA AGAAAAGGATGACTTTAAGCAAGAAACTCTT CCAAGCAATTCCAATGAAAGCCATGACCACA TGGACGACGATGATGACGATGATGATGACG ATGGAGACCATGCAGAGAGCGAGGATTCTG TGGACTCGGATGAATCTGACGAATCTCACCA TTCGGATGAGTCTGATGAGACCGTCACTGCT AGTACACAAGCAGACACTTTCACTCCAATCG TCCCTACAGTCGATGTCCCCAACGGCCGAGG TGATAGCTTGGCTTATGGACTGAGGTCAAAG TCTAGGAGTTTCCAGGTTTCTGATGAACAGT ATCCTGATGCCACAGATGAGGACCTCACCTC TCACATGAAGAGCGGTGAGTCTAAGGAGTCC CTCGATGTCATCCCTGTTGCCCAGCTTCTGAG CATGCCCTCTGATCAGGACAACAACGGAAA GGGCAGCCATGAGTCAAGTCAGCTGGATGA ACCAAGTCTGGAAACACACAGACTTGAGCAT TCCAAAGAGAGCCAGGAGAGTGCCGATCAG TCGGATGTGATCGATAGTCAAGCAAGTTCCA

Table A2. (cont'd)

	AAGCCAGCCTGGAACATCAGAGCCACAAGT TTCACAGCCACAAGGACAAGCTAGTCCTAGA CCCTAAGAGTAAGGAAGATGATAGGTATCTG AAATTCCGAATTTCTCATGAATTAGAGAGTT CATCTTCTGAGGTCAACGAATTCCTTAAGGG CGGTAGCGGTCACCATCACCATTAA

5.4 APPENDIX B

5.4.1 List of primers

Table B1. Nucleotide sequences of primers used in cloning ALP, OCN and OPN genes.

pEt22b-ALP (BamHI-HindIII)	**Forward Primer**	5' ATCTCAGTGGTGGTGGTGGTGGTGCTCGAGTCATCATTTCAGCCCCAGAGCGGC 3'
	Reverse Primer	5' ATAGGGGAATTGTGAGCGGATAACAATTCCCCTCTAGAAATAATTTTGTTTA 3'
pGEX-6P1-OCN (BamHI-EcoRI)	**Forward Primer**	5' AAGTTCTGTTCCAGGGGCCCCTGGGATCCGAAAACCTGTATTTTCAGGGCATGAAACCG TCTGGCGCAGA 3'
	Reverse Primer	5' GCTCGAGTCGACCCGGGAATTCATGATGATGGTGGTGGTGGACCGGGCCGTAGAAGCG AC 3'

Table B1. (cont'd)

pEt22b-OPN (NotI-XhoI)	**Forward Primer**	5' CGAATTCGAGCTCCGTCGACAAGCTTGCGGCCGCATGATTCCGGTTAAACAGGC 3'
	Reverse Primer	5' GCCGGATCTCAGTGGTGGTGGTGGTGGTGCTCGAGATTCACTTCGGAACTCGCTG 3'
pCDNA3-mOCN (HindIII-XbaI)	**Forward Primer**	5' CTATAGGGAGACCCAAGCTTTACTTCCAATCCAATGCCACCGGTACCATGAGGACCCTCTCTCTG 3'
	Reverse Primer	5' ATAGAATAGGGCCCTCTAGATTAATGGTGATGGTGACCGCTACCGCCCTTAAGGAATTCAATAGTGATACCGTAGATG 3'
pCDNA3-mOPNa (KpnI-EcoRI)	**Forward Primer**	5' AATCCAATGCCACCGGTACCATGAGATTGGCAGTGATTTG 3'
	Reverse Primer	5' CTACCGCCCTTAAGGAATTCGTTGACCTCAGAAGATGAAC 3'

Table B2. Nucleotide sequences of primers used in qRT-PCR reactions.

Primer Name	Primer Sequence	Amplicon length	T_m
hGAPDH Fwd	5' GCTCTCTGCTCCTCCTGTTC 3'	412	63
hGAPDH Rev	5' CAAATGAGCCCCAGCCTTCT 3'		
mOCN Fwd	5' CTATAGGGAGACCCAAGCTTATGAGGACCCTCTCTCT 3'	475	57
mOCN Rev	5' ATAGAATAGGGCCCTCTAGAATGGTGATGGTGATGGTGTCTGAA CTTTATTTTGGAGC 3'		
mOPNa Fwd	5' CGGTGAAAGTGACTGATTCTGGC 3'	114	60
mOPNa Rev	5' GCAAGGAGATTCTGCTTCTGAGATG 3'		

5.5 APPENDIX C

5.5.1 Plasmid maps

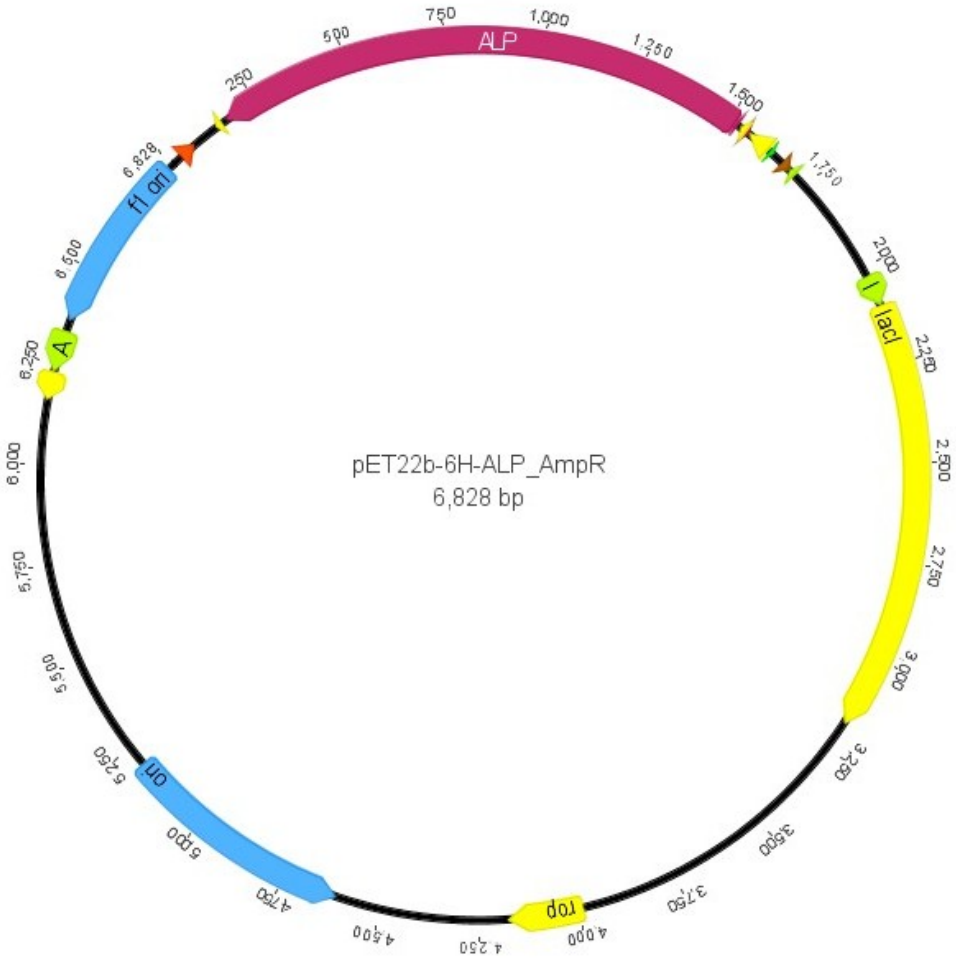

Figure C1. Schematic representation of pEt22b-pelB-6H-ALP plasmid.

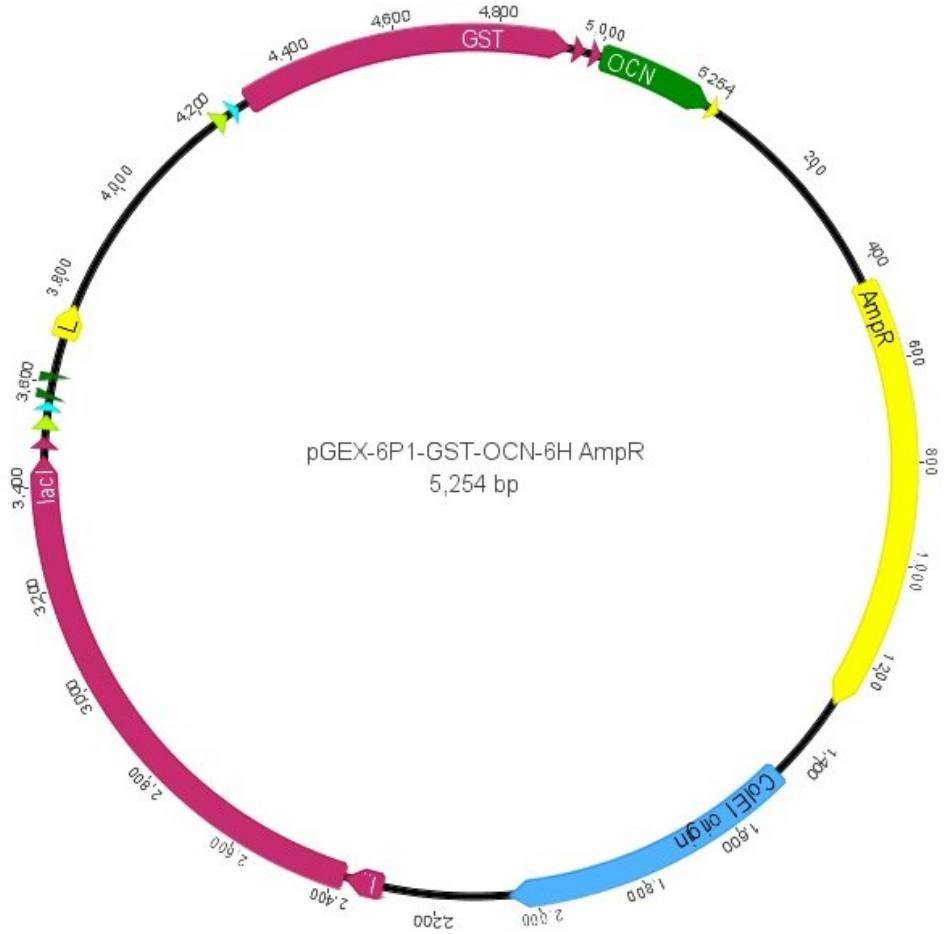

Figure C2. Schematic representation of pGEX-6P1-GST-OCN-6H plasmid.

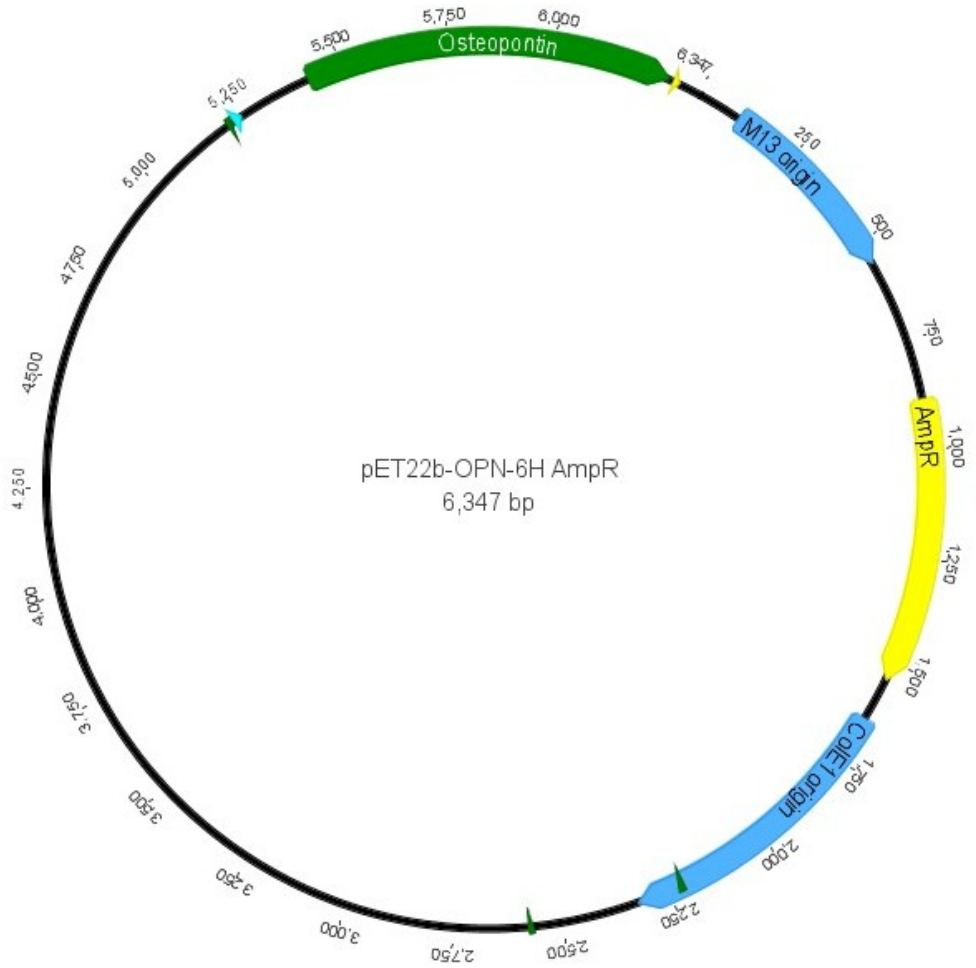

Figure C3. Schematic representation of pEt22b-OPN-6H plasmid.

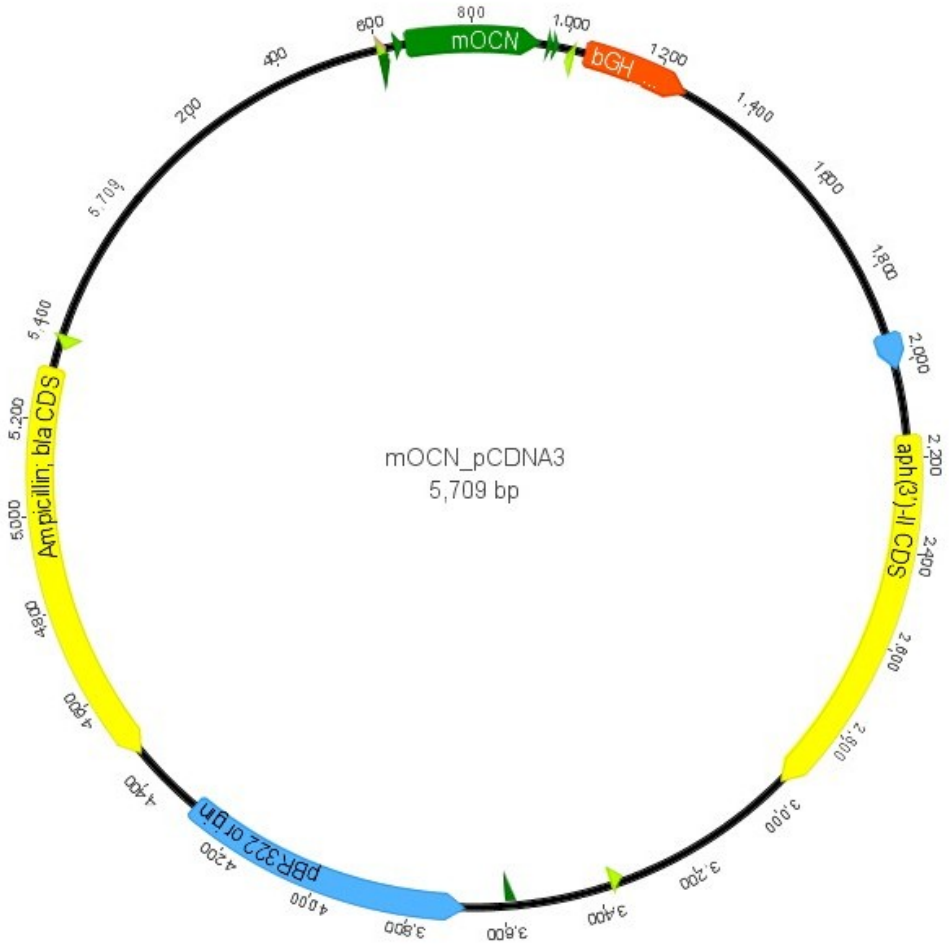

Figure C4. Schematic representation of pCDNA3-OCN-4H plasmid.

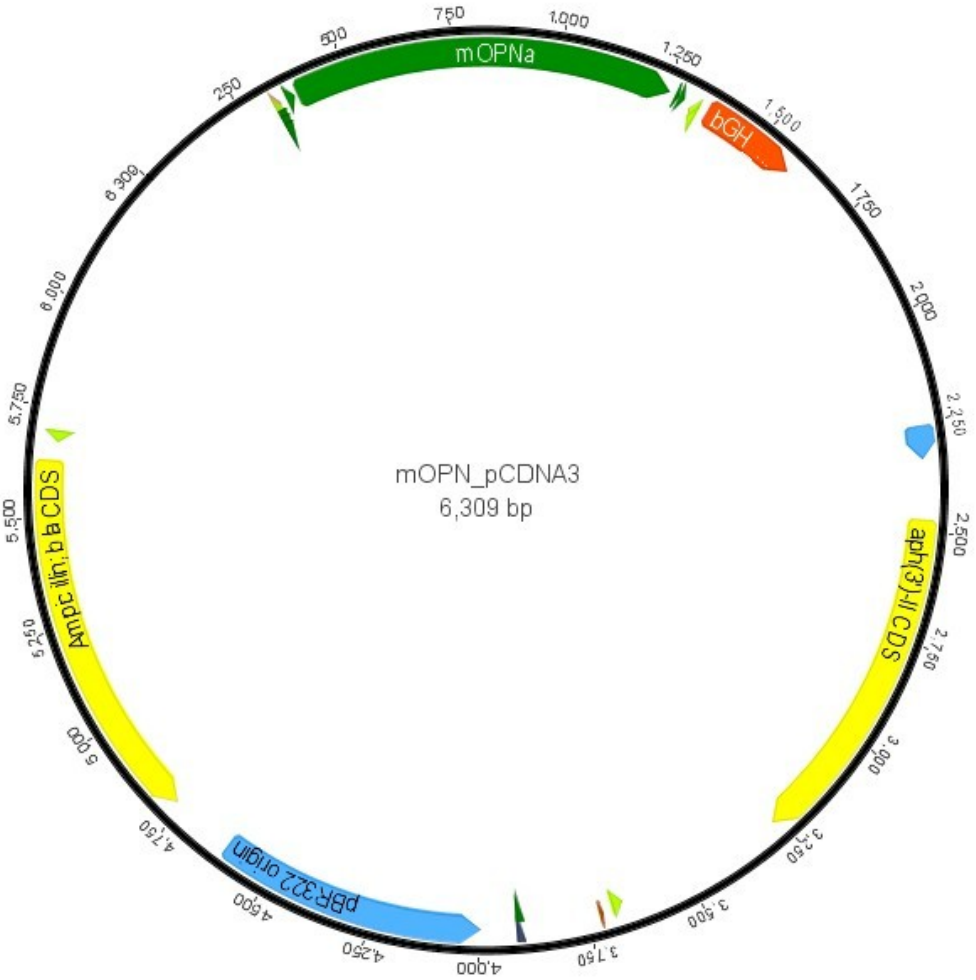

Figure C5. Schematic representation of pCDNA3-OPN-4H plasmid.

5.6 APPENDIX D

5.6.1 Sanger sequencing results

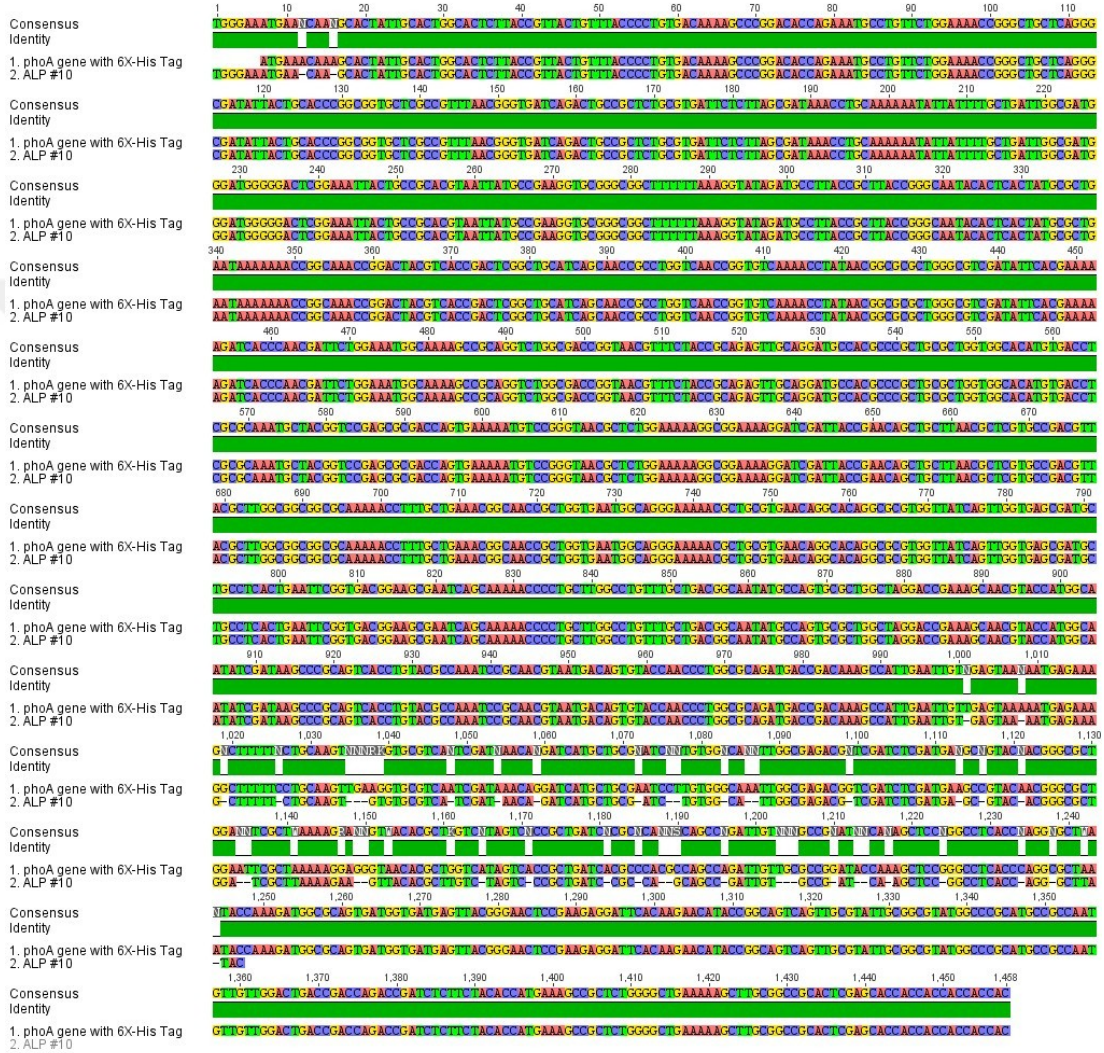

Figure D 1. Sequencing alignment of pEt22b-ALP construct with phoA gene sequence. Analysis performed in Geneious R9.0.5 Software. (Score = 5475.0, Identities = 1189/1458 (81%), Positives = 1189/1458 (81%), Gaps = 261/1458 (17%))

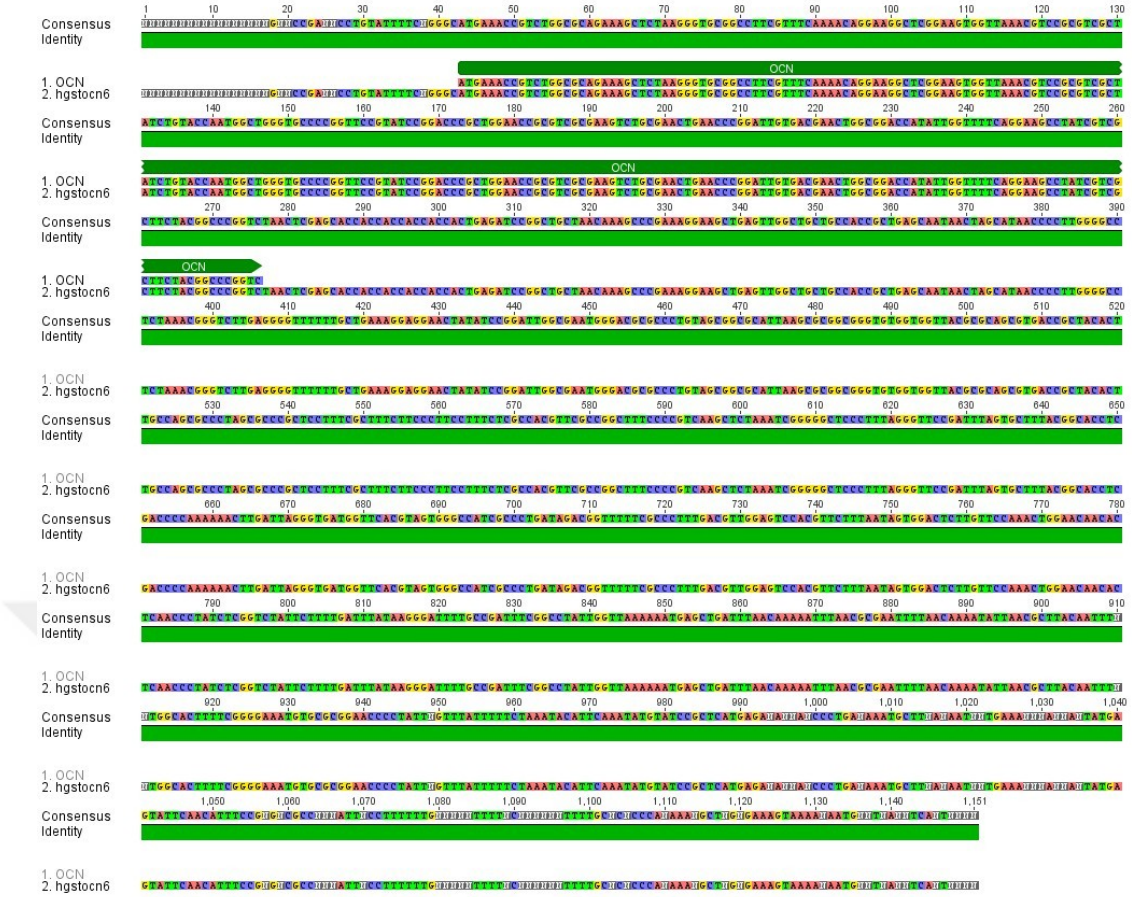

Figure D 2. Sequencing alignment of pGEX-6P1-GST-OCN-6H construct with synthetic OCN gene fragment sequence. Analysis performed in Geneious R9.0.5 Software.

Score = 1170.0, Identities = 234/1151 (20%), Positives = 234/1151 (20%), Gaps = 917/1151 (79%)

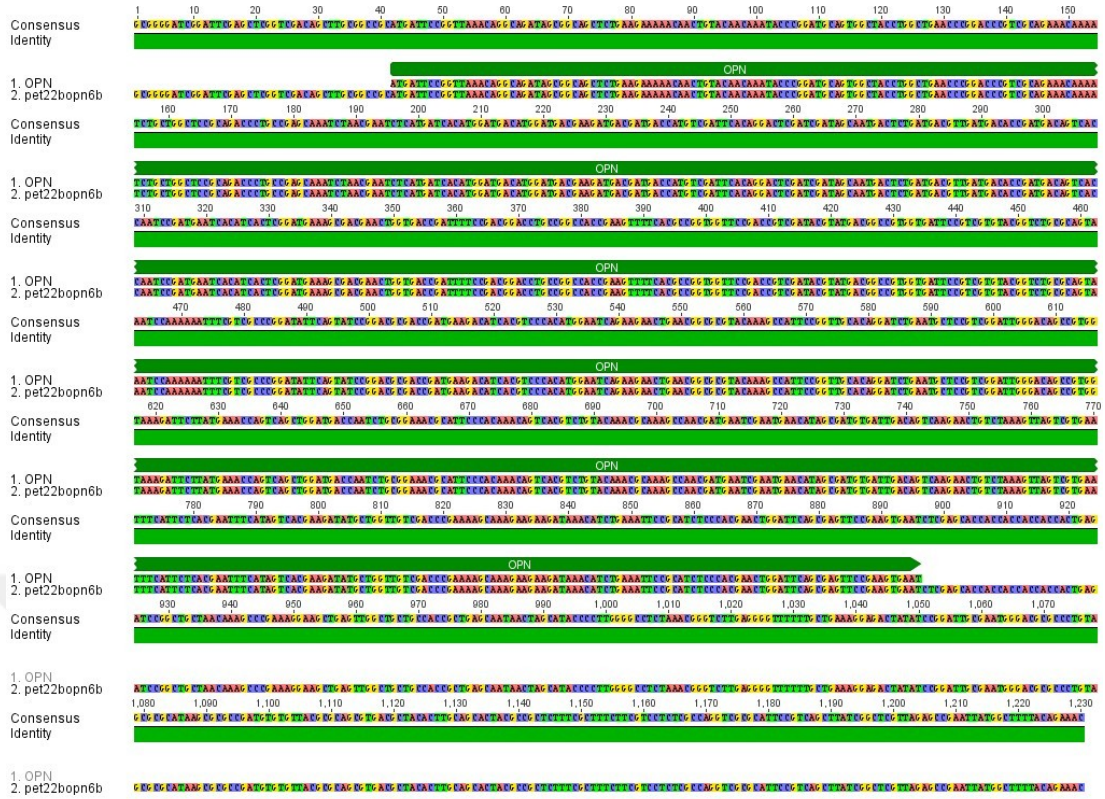

Figure D3. Sequencing alignment of pEt22b-OPN-6H construct with synthetic OPN gene fragment sequence. Analysis performed in Geneious R9.0.5 Software.

Score = 4275.0, Identities = 855/1230 (69%), Positives = 855/1230 (69%), Gaps = 375/1230 (30%)

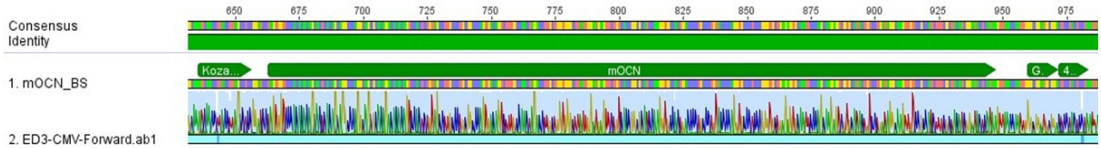

Figure D4. Sequencing alignment of pCDNA3-mOCN-4H construct with mOCN cDNA sequence. Score = 4835.75, Identities = 1013/5710 (17%),

Positives = 1076/5710 (18%), Gaps = 4632/5710 (81%)

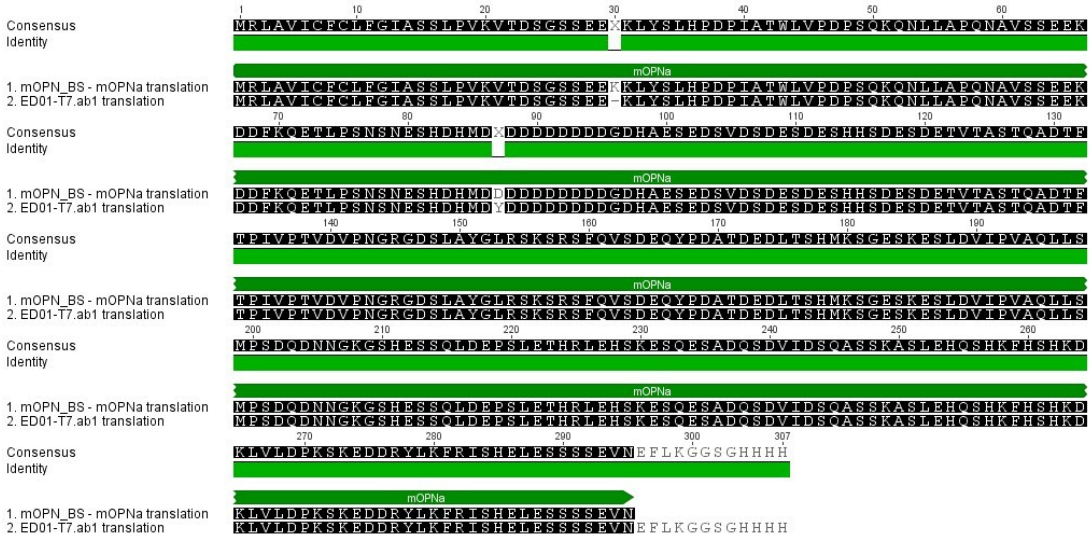

Figure D5. Sequencing alignment of pCDNA3-mOPNa-4H construct with mOPNa cDNA sequence. Score = 1500.0, Identities = 293/307 (95%),

Positives = 293/307 (95%), Gaps = 13/307 (4%)

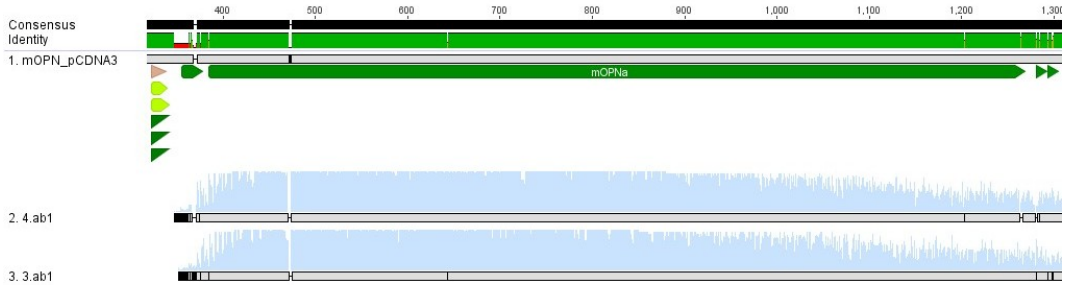

Figure D6. Sequencing alignment of pCDNA3-mOPNa-4H (K30) and pCDNA3-mOPNa-4H (K30, D87Y) constructs with mOPNa cDNA sequence. First colony does not contain missense mutation while second colony has missense mutation.

5.7 APPENDIX E

5.7.1 Amino acid sequences of proteins

Table E1. Amino acid sequences of ALP, GST-OCN, OCN and OPN proteins.

E. coli ALP amino acid sequence with pelB, 6X His-Tag and GS Linker	MKYLLPTAAAGLLLLAAQPAMAMGHHHHHHGGGGSRTPE MPVLENRAAQGDITAPGGARRLTGDQTAALRDSLSDKPAK NIILLIGDGMGDSEITAARNYAEGAGGFFKGIDALPLTGQYT HYALNKKTGKPDYVTDSAASATAWSTGVKTYNGALGVDIH EKDHPTILEMAKAAGLATGNVSTAELQDATPAALVAHVTS RKCYGPSATSEKCPGNALEKGGKGSITEQLLNARADVTLGG GAKTFAETATAGEWQGKTLREQAQARGYQLVSDAASLNSV TEANQQKPLLGLFADGNMPVRWLGPKATYHGNIDKPAVTC TPNPQRNDSVPTLAQMTDKAIELLSKNEKGFFLQVEGASIDK QDHAANPCGQIGETVDLDEAVQRALEFAKKEGNTLVIVTAD HAHASQIVAPDTKAPGLTQALNTKDGAVMVMSYGNSEEDS QEHTGSQLRIAAYGPHAANVVGLTDQTDLFYTMKAALGLK

Table E1. (cont'd)

GST-OCN recombinant fusion protein amino acid sequence with TEV protease recognition sequence	MSPILGYWKIKGLVQPTRLLLEYLEEKYEEHLYERDEG DKWRNKKFELGLEFPNLPYYIDGDVKLTQSMAIIRYIAD KHNMLGGCPKERAEISMLEGAVLDIRYGVSRIAYSKDF ETLKVDFLSKLPEMLKMFEDRLCHKTYLNGDHVTHPDF MLYDALDVVLYMDPMCLDAFPKLVCFKKRIEAIPQIDK YLKSSKYIAWPLQGWQATFGGGDHPPKSDLEVLFQGPL GSENLYFQGMKPSGAESSKGAAFVSKQEGSEVVKRPRR YLYQWLGAPVPYPDPLEPRREVCELNPDCDELADHIGF QEAYRRFYGPVHHHHHHEFPGRLERPHRD*
Recombinant OCN amino acid sequence without secretion signal sequence and with 6X-His Tag	MKPSGAESSKGAAFVSKQEGSEVVKRPRRYLYQWLGA PVPYPDPLEPRREVCELNPDCDELADHIGFQEAYRRFYG PVHHHHHHEFPGRLERPHRD*

Table E1. (cont'd)

Recombinant OPN amino acid sequence without secretion signal sequence and with 6X-His Tag	MIPVKQADSGSSEEKQLYNKYPDAVATWLNPDPSQKQ NLLAPQTLPSKSNESHDHMDDMDDEDDDDHVDSQDSI DSNDSDDVDDTDDSHQSDESHHSDESDELVTDFPTDLP ATEVFTPVVPTVDTYDGRGDSVVYGLRSKSKKFRRPDI QYPDATDEDITSHMESEELNGAYKAIPVAQDLNAPSDW DSRGKDSYETSQLDDQSAETHSHKQSRLYKRKANDESN EHSDVIDSQELSKVSREFHSHEFHSHEDMLVVDPKSKEE DKHLKFRISHELDSASSEVNLEHHHHHH*

Table E2. Amino acid sequences of mouse pre-osteoblast derived OCN and OPN proteins.

mOCN amino acid sequence with Kozak sequence, GS linker, 4x-His tag, stop codon	YFQSNATGTMRTLSLLTLLALAALCLSDLTDAKPSGPESDKAFMSKQEGNKVVNRLRRYLGASVPSPDPLEPTREQCELNPACDELSDQYGLKTAYKRIYGITIEFLKGGSGHHHH*
mOPNa amino acid sequence with Kozak sequence, GS linker, 4x-His tag, stop codon	YFQSNATGTMRLAVICFCLFGIASSLPVKVTDSGSSEEKKLYSLHPDPIATWLVPDPSQKQNLLAPQNAVSSEEKDDFKQETLPSNSNESHDHMDDDDDDDDDDGDHAESEDSVDSDESDESHHSDESDETVTASTQADTFTPIVPTVDVPNGRGDSLAYGLRSKSRSFQVSDEQYPDATDEDLTSHMKSGESKESLDVIPVAQLLSMPSDQDNNGKGSHESSQLDEPSLETHRLEHSKESQESADQSDVIDSQASSKASLEHQSHKFHSHKDKLVLDPKSKEDDRYLKFRISHELESSSSEVNEFLKGGSGHHHH*

5.8 APPENDIX F

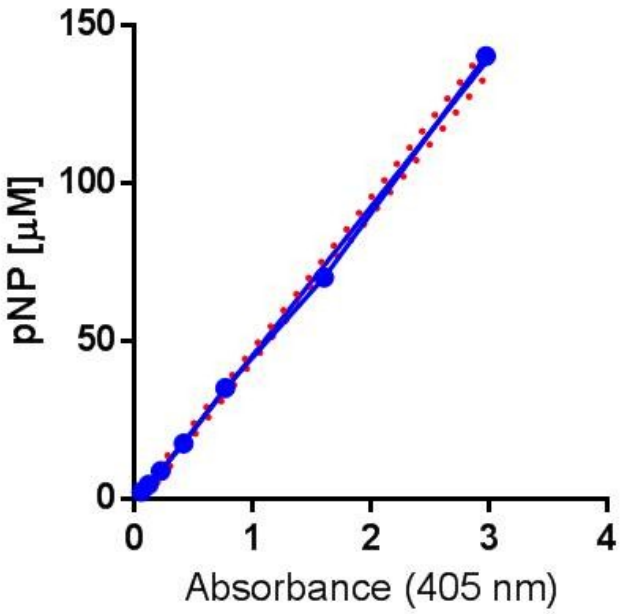

Figure F1. Standard curve for pNP concentration. ($y = 47.19x - 1.655$, $R^2 = 0.998$)

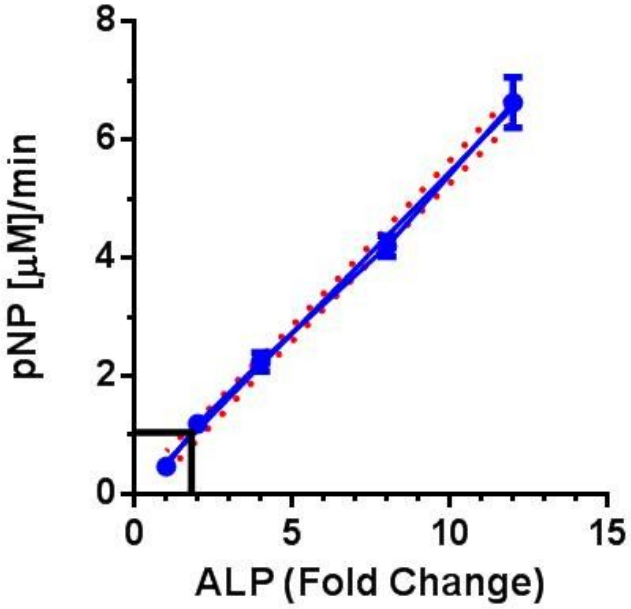

Figure F 2. Determination of ALP unit enzyme concentration. ($y = 0.546x - 0.008$, $R^2 = 0.997$) 1 U enzyme corresponds to the 1.98 fold ALP, which generates 1 µM pNP in 1 min.

5.9 APPENDIX G

5.9.1 Secondary structure analysis.

Table G1. Secondary structure prediction by Bestsel online tool. Secondary structure analysis of OCN and OPN proteins and their changes upon addition of $CaCl_2$ (Ca^{2+}), β-GP (organic phosphate, P) and Na_2HPO_4 (inorganic phosphate, P_i). The analysis was done based on the protocol described elsewhere. (Micsonai, Wien et al. 2015).

37 ºC	OCN	OCN + Ca^{2+}	OCN + P	OCN + P_i	OPN	OPN + Ca^{2+}	OPN + P	OPN + P_i
Helix1 (regular)	0	0	0	2.1	3.3	1.7	1.9	3.6
Helix2 (distorted)	13.7	17.1	11.7	0	7.8	10.1	5.6	16.2
Anti1 (left-twisted)	13.8	10.4	11	0	6.2	4.2	2	3.9
Anti2 (relaxed):	0	0	0	24.4	5.7	10	12.5	0
Anti3 (right-twisted):	4.7	14.3	8.5	27.9	13.9	10	13.1	6.2
Parallel:	0	0	0	0	0	0	0	5.3

Table G1. (cont'd)

Turn:	20.3	11.7	17.5	21.9	15	16.1	15.6	13.5
Others:	47.5	46.5	51.3	23.8	48.1	47.9	49.3	51.2
Helix:	13.7	17.1	11.7	2.1	11.1	11.8	7.5	19.8
Anti-parallel:	18.6	24.7	19.5	52.3	25.8	24.2	27.6	10.1
Parallel:	0	0	0	0	0	0	0	5.3
Turn:	20.3	11.7	17.5	21.9	15	16.1	15.6	13.5
Others:	47.5	46.5	51.3	23.8	48.1	47.9	49.3	51.2

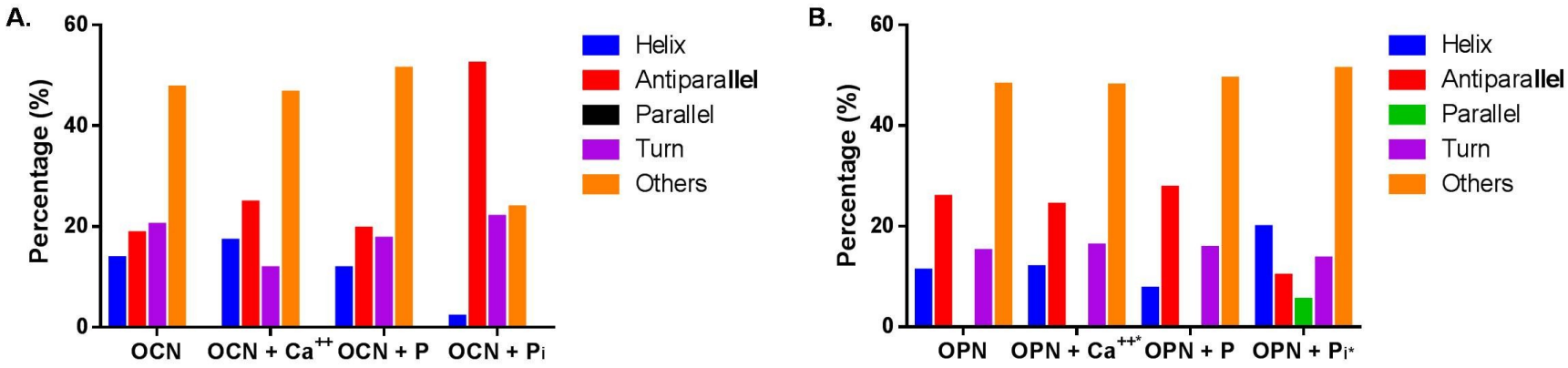

Figure G1. Secondary structure analysis of OCN and OPN proteins and their changes upon addition of $CaCl_2$ (Ca^{2+}), β-GP (organic phosphate, P) and Na_2HPO_4 (inorganic phosphate, P_i). The analysis was done based on the protocol described elsewhere with Bestsel online tool.(Micsonai, Wien et al. 2015)

5.10 APPENDIX H

5.10.1 Comparison of commercial HAP with CaP crystals in our system

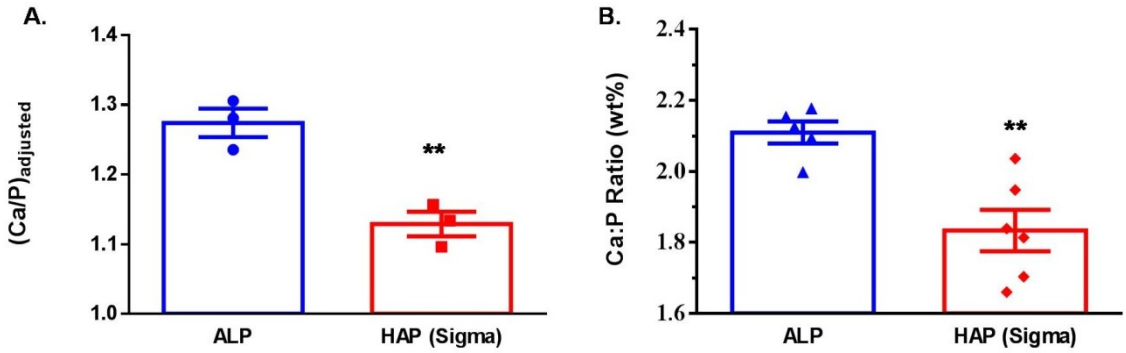

Figure H 1. Comparison of Ca:P ratio of the CaP crystals in our system with the commercial HAP. Ca:P ratio was calculated by XPS and EDS, respectively. Measurements were done after 24 h of incubation at 37 ˚C. **A.** 3 points with 400 µm spot size were selected for XPS scanning. **B.** 5-6 points were selected EDS analysis. Unpaired t-test was performed to analyze statistical significance.